Journal Pre-proof

A regularized variational mechanics theory for modeling the evolution of brittle crack networks in composite materials with sharp interfaces

Kaushik Vijaykumar, Benjamin E. Grossman-Ponemon, Yang Wan, Pooya Yousefi, Christopher J. Larsen, Haneesh Kesari

PII: S0022-5096(24)00238-2
DOI: https://doi.org/10.1016/j.jmps.2024.105772
Reference: MPS 105772

To appear in: *Journal of the Mechanics and Physics of Solids*

Received date : 16 November 2023
Revised date : 30 May 2024
Accepted date : 4 July 2024

Please cite this article as: K. Vijaykumar, B.E. Grossman-Ponemon, Y. Wan et al., A regularized variational mechanics theory for modeling the evolution of brittle crack networks in composite materials with sharp interfaces. *Journal of the Mechanics and Physics of Solids* (2024), doi: https://doi.org/10.1016/j.jmps.2024.105772.

A regularized variational mechanics theory for modeling the evolution of brittle crack networks in composite materials with sharp interfaces

Kaushik Vijaykumar[a], Benjamin E. Grossman-Ponemon[a,c], Yang Wan[a], Pooya Yousefi[b,d], Christopher J. Larsen[b], Haneesh Kesari[a,*]

[a]*Division of Solid Mechanics, School of Engineering, Brown University, Providence, RI 02912, United States*
[b]*Department of Mathematical Sciences, Worcester Polytechnic Institute, Worcester, MA 01609, United States*
[c]*New address: Department of Physics and Engineering, John Carroll University, University Heights, OH 44118, United States*
[d]*New address: Department of Mathematics & Statistics, McMaster University, Hamilton, Ontario, L8S 4K1, Canada*

Abstract

In the design of structural materials, there is traditionally a tradeoff between achieving high strength and achieving high toughness. Nature offers creative solutions to this problem in the form of structural biomaterials (SBs), intelligent arrangements of mineral and organic phases which possess greater strength and toughness than the constituents. The micro-architecture of SBs like nacre and sea sponge spicules are characterized by weak organic interfaces between brittle mineral phases. To better understand the toughening mechanisms in SBs requires simulation techniques which can resolve arbitrary interface and bulk fracture patterns.

In this work, we present a modified regularization of Variational Fracture Theory (VFT) that allows for simulation of fracture in materials and structures with weak interfaces. The core of our approach is widen the weak interfaces on a length scale proportional to that of the diffuse damage field, and assign a reduced fracture toughness therein. We show that in 2D the modified regularized functionals Γ-converge to that for sharp cracks. The resulting thin weak interfaces have fracture toughness which depends on the bulk material fracture toughness, the widened interface fracture toughness, and the widened interface length scale. We next apply our modified regularization within a computer implementation of regularized VFT, which we term RVFTI. We assess the performance of RVFTI in 2D by reproducing the effective interface fracture toughness predicted by the Γ-convergence theory and simulating crack trapping at a bi-material interface. We then use RVFTI to study toughening in SB-inspired microarchitectures, namely layered materials and materials with wavy interfaces.

Keywords: regularized variational fracture theory, weak interface, interfacial fracture

This research paper is dedicated to Professor Allan Bower on the occassion of his retirement. We celebrate him for his exceptional and deep scholarship in the field of Solid Mechanics, and for inspiring and supporting several young scientists through his mentorship and teaching.

*Corresponding author
Email address: haneesh_kesari@brown.edu (Haneesh Kesari)

1. Introduction

In structural engineering, it is important for materials to possess both high strength and high toughness. However, in conventional structural materials such as steels and aluminum alloys, strength and toughness are in competition, as the mechanisms that enhance one can inhibit the other [1]. Recent studies indicate that structural biomaterials (SBs) show both high strength and toughness [1, 2, 3, 4, 5, 6]. Most such SBs are heterogeneous in nature and consist of a mineral (stiff) phase and an organic (compliant) phase. Nacre is one such SB where the mineral phase occupies $> 95\%$ of the volume fraction of the material [3]. Due to the presence of high volume fraction of the mineral phase, Aragonite ($CaCO_3$), the bulk properties of nacre such as Young's modulus and Poisson's ratio are almost identical to Aragonite. Hence, it is meaningful to compare the mechanical behavior of nacre to Aragonite. Nacre obtains its high strength properties from Aragonite, and has a tensile strength of ≈ 170 MPa which is almost identical to that of Aragonite [7]. However, the work of fracture in nacre can be as large as 1500 J/m^2, while that in Aragonite is about 10 J/m^2 [2]. Hence, SBs are ideal prototypical materials for understanding mechanisms which enable high strength and toughness.

The micro-architectural arrangement of phases varies in different SBs, although the organic phase is often located at interfaces in the mineral phase. Such an example is nacre, whose micro-architecture resembles a brick-and-mortar structure as seen in Fig. 1(a). Here, the bricks consist of the mineral phase while the mortar is organic. However, in other SBs such as spicules in sea sponges, some of the organic phase is also mixed with the mineral phase [8, 9, 10]. The micro-architecture of spicules resembles that of a lamellar structure, as seen in Fig. 1(b), where the mineral phase is arranged concentrically and is separated by a nanometer-thin layer (approximately 35 nm [11]) of the organic phase.

Attempts to replicate these micro-architectural designs have been quite promising. As shown in Fig. 1(c), an alumina-based composite mimicking the micro-architecture of nacre achieved higher peak stress and exhibited greater area under the stress-strain curve, called the work of fracture [12], when subjected to notched three-point bending experiments [1]. The work of fracture is a useful measure of toughness in materials, as it quantifies the energy needed to be applied in order to break the structure. It can be clearly seen that the alumina-based composite has higher strength and toughness than nacre.

The superior toughness properties of SBs, such as bone and nacre, are plotted in Fig. 1(d). From the figure, we see that bone and nacre display higher toughness than either of their respective mineral and organic phases. Furthermore, the alumina-based composite has even higher toughness than the SBs. This suggests that a comprehensive understanding of the failure mechanisms in SBs can aid in designing materials with superior properties to those found in nature.

It has been postulated that higher toughness in SBs can be attributed to fracture mechanisms such as crack deflection and crack arrest, which are shown in Fig. 1(b) [6, 3]. However, insights into the underlying toughening mechanisms such as the interplay of fracture mechanisms at different length scales and the operating extrinsic toughening mechanisms (e.g., crack deflection and crack arrest) have not been studied adequately. Further, the effect of model parameters such as the thickness of the interface, the ratio of fracture toughness of the phases, and the arrangement of the phases on the toughness of the SBs is still unexplored. To address these gaps, we believe that computational models capable of modeling such complex architectural designs can be used to conduct virtual experiments which can aid in engineering synthetic materials with both high strength and toughness.

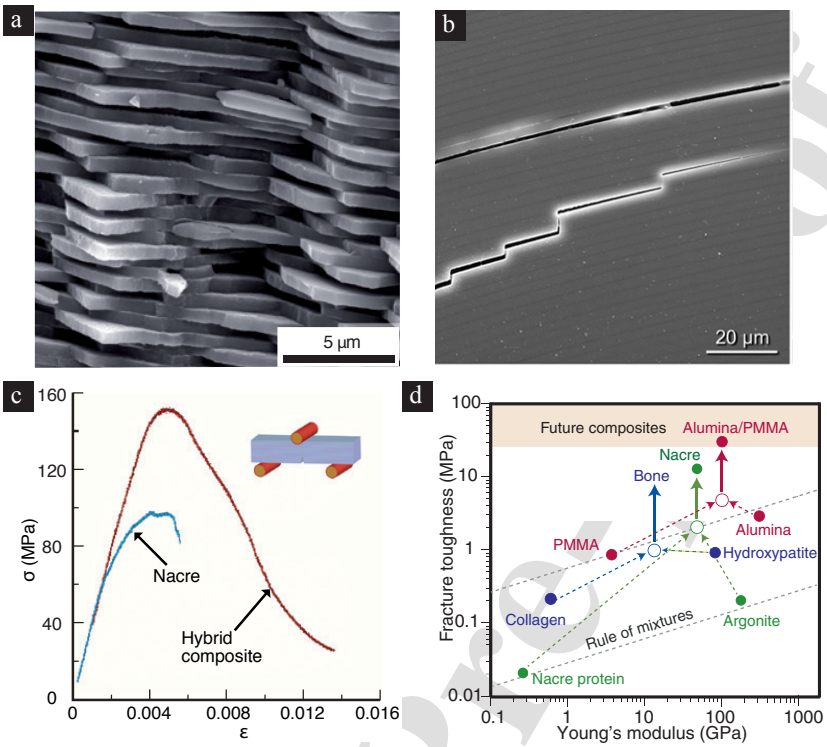

Figure 1: (a) SEM micrograph of nacre showing the brick-and-mortar micro-architecture. Figure reproduced from [1]. (b) SEM micrograph of *Monorhaphis chuni* (*M.chuni*) specimen subjected to a three point bend test. It is observed that the specimen before failure develops convoluted crack patterns due to crack deflection and arrest at the interfaces. Figure reproduced from [6]. (c) A comparison of the stress-strain response obtained by edge notched three point bend testing of nacre and a synthetic composite made of 75% alumina indicates that the composite has both higher strength and toughness as compared to nacre. Figure reproduced from [1]. (d) A summary of fracture toughness properties of structural biomaterials, hybrid composites in comparison to their respective constituents. Figure reproduced from [13].

In recent years, researchers have performed experimental and analytical studies to explore mechanisms to increase toughness in ceramic composites [14, 15, 16]. Phenomena such as crack trapping and crack bridging due elastic heterogeneities and their ability to enhance the toughness of materials have also been studied [17, 18, 19, 20]. A perturbation-based analysis was employed to shed light on the role of elastic moduli on fracture toughness [21]. Studies predominantly using semi-analytical methods have investigated the toughness of interfaces in the presence of elastic heterogeneities in semi-infinite geometries [22, 23, 24, 25, 26]. However, these studies fall short in providing a complete description of how toughness is enhanced in SBs for various reasons:

(1) The aforementioned numerical studies are limited to small extensions to the pre-defined crack in ceramic composites or SBs, and therefore the influence of crack tortuosity on toughness is unclear.

(2) Fracture mechanisms such as crack bridging, crack deflection, and crack arrest are not well understood.

(3) SBs such as bone have a hierarchical architecture, and there are different fracture mechanisms operating at different length scales. The aforementioned works do not study the contributions of different mechanisms to the bulk toughening.
(4) The influence of geometric features and micro-architecture on toughness is inadequately studied. Therefore, greater research is needed to understand these micro-architectures and how they might enhance both strength and toughness.

Numerical methods featuring cohesive zone models have been used to study how toughness can be enhanced in the presence of interfaces [27, 28]. These studies are limited by the fact that cracks could only grow along a set of pre-defined paths, and therefore instabilities such as crack jumps from the interface to the bulk could not be simulated. Meanwhile, Begley and co-workers [29, 30] simulated brick-and-mortar micro-architectures using rigid bricks and cohesive interfaces. The problem was solved using Monte Carlo methods by prescribing displacements to the bricks and iterating until a configuration with minimum energy is achieved.

Working in the broader realm of heterogenous materials, Bourdin and Battacharya and collaborators [31, 32, 33, 34, 35] have investigated through computations using regularized variational fracture theory (RVFT) (and in some cases with experiments) how the effective toughness of a specimen is affected by the presence of elastic heterogeneities and fracture toughness heterogeneities. In particular, the simulations were able to capture crack tortuosity which resulted from the geometry of the heterogeneities. These studies have generally focused on evaluating the effective fracture toughness in domains with periodic arrangements of stiff and compliant materials subjected to Mode-I loading. Further, the effective fracture toughness is defined using the J-integral, which is computed using the the outermost boundary of the domain as the contour of integration. Importantly, the length scales within the considered heterogeneous media were all comparable. In contrast, in SBs such as nacre, the compliant interfaces are orders of magnitude thinner than the stiff bricks.

The core challenge for any potential numerical method to simulate crack evolution in SBs is capturing the complex crack morphologies that have been demonstrated in experiments. Methods which represent the crack via sharp surfaces (or curves in 2D) face some difficulties with this task. Methods like the eXtended Finite Element Method (XFEM) [36, 37, 38] require an explicit representation of the crack geometry (such as a surface parameterization or a level set) to define enrichment functions. Crack growth is typically modeled via crack front (or crack tip in 2D) dynamics, for example with Griffith's criterion [39]; additional criteria or models are needed to incorporate crack branching and crack nucleation. Another class of sharp crack methods are based on cohesive zone models, such as [40, 41]. In these methods, cohesive zone separation laws are imposed on the faces (or edges in 2D) between neighboring finite elements. This provides a unified framework for crack growth, crack nucleation, and crack branching, because cracks may nucleate and grow between any elements. However, this method is limited as the crack patterns are heavily mesh-dependent.

A family of models which can simulate complex crack morphologies uses phase fields to model fracture. With origins in continuum damage theory [42], phase transformation theory [43], and variational fracture theory (VFT) [44, 45, 46], these models replace sharp cracks with a diffuse damage field, the evolution of which models crack growth. In the case of RVFT, the damage field (i.e. the cracks) evolves such that the total energy (elastic plus fracture) of the system is minimized. Furthermore, the notion of Γ-convergence [47] provides a rigorous mathematical connection between the phase-field approximations of RVFT [45] and the original sharp-crack theory [48]. Unlike sharp crack approaches, there are minimal prior restrictions on the distribution of damage in the problem domain, which means that a wide variety of crack morphologies may be simulated without mesh

dependence, including crack branching and crack jumps across heterogeneities [49, 50, 31]. While RVFT and phase field models present their own difficulties, for example requiring large amounts of mesh refinement to adequately resolve the damage field, their ability to produce realistic and complex crack morphologies is why we have chosen them as the basis of our approach for SBs.

Phase field models have been introduced to simulate fracture in the presence of weak interfaces. In [51, 52], the interface, which is nominally a surface of co-dimension 1 embedded within the bulk material, is replaced by a region with finite thickness. Within this region of finite thickness, the fracture toughness and/or elastic moduli are allowed to vary. In [51], the fracture toughness is assigned a constant value within the wide interface; in [52], the authors also explore smoother fracture toughness distributions and elastic moduli distributions. For the case of constant wide-interface fracture toughness, the authors derive relationships for the effective interface fracture toughness as a function of the bulk toughness, the assigned wide-interface fracture toughness, the wide-interface thickness, and the damage field length scale. These formulas are assessed numerically through examples.

Approaches taken after [51, 52] generally follow a similar approach. For example, in [53], the authors adopt the approach of a constant fracture toughness within the wide interface as in [51]. In [54], the authors also assign constant fracture toughness within the wide interface; however, they also explore the case where the bulk fracture toughness is different on either side of the interface. Meanwhile, in [55], a Gaussian kernel is used to create a smooth variation in the fracture toughness.

In this work, we modify the traditional regularization process for VFT (recapitulated in §3.1 and §3.2) to incorporate materials whose fracture toughness may differ along interfaces with zero thickness. Such cases are representative of atomically-thin bonding in adhesive contact, grain boundaries in polycrystalline materials, or interfaces whose thickness is much smaller than other relevant problem dimensions (e.g., the organic phase in SBs). In our regularization approach, the interfaces are assigned finite (small) width, inside which the material has fracture toughness g_i, while the surrounding material has fracture toughness g_b. The interface width is chosen to scale proportionally with the fracture regularization length ε, and is discussed further in §3.3. Under suitable assumptions, we prove the Γ-convergence result for arbitrary two-dimensional specimens in §4. A consequence of this result is that we quantify the effective interface fracture toughness g_{int} of the zero-thickness interface, which depends g_b, g_i, and the proportionality constant of the interface width to ε. Returning to the problem of crack evolution in SBs, we implement our modified regularization procedure within a phase-field model for irreversible, brittle fracture, see §5. In §6, we verify that the modified RVFT for interfaces (RVFTI) reproduces fracture toughness consistent with g_{int}, and we explore crack kinking at a bi-material interface. We then use RVFTI to study toughening mechanisms in SB-inspired configurations in §7. Lastly, we discuss the main results and conclude this work in §8.

We remark that our approach resembles the work of [51, 52] in that we replace an infinitesimally-thin interface by one with finite thickness and assign a constant fracture toughness g_i (that is different from g_{int}) within. However, our approach is motivated by Γ-convergence; that is, we introduce a regularization to the variational fracture problem in a material with weak interfaces and we prove under some mild assumptions that the regularization Γ-converges to the original problem.

While the results in this work are particularized to two dimensional problems, we believe that the theory also applies in 3D. Three dimensional RVFTI simulations have been performed, but we do not present these here.

2. Mathematical Preliminaries

2.1. Notation

We let unbolded symbols such as x and u denote scalars or scalar-valued fields, while we let bold symbols such as $\boldsymbol{x}$ and $\boldsymbol{u}$ denote vectors or vector-valued fields in $\mathbb{R}^n$. We denote sequences with parentheses: $(a_n)_n := (a_1, a_2, a_3, \ldots)$. Depending on context, $|\cdot|$ may indicate the absolute value of a scalar, the Euclidean norm of a vector, or the Frobenius norm of a tensor.

There are two important measures used in this manuscript. Further details on measure theory may be found in textbooks such as [56]. For any subset $A \subseteq \mathbb{R}^n$, we let $\mathcal{L}^n(A)$ denote the n-dimensional Lebesgue measure of A (which may be infinite). Integration with respect to this measure is written with the standard notation $\int \mathrm{d}\boldsymbol{x}$. Next, for $A \subseteq \mathbb{R}^n$, we let $\mathcal{H}^m(A)$ denote the m-dimensional Hausdorff measure of A (where m may differ from n), which is defined in two steps. First, for any $\delta > 0$,

$$\mathcal{H}^m_\delta(A) = \inf\left\{ \alpha_m \sum_{i=1}^{\infty} \operatorname{diam}(U_i)^m \ : \ A \subseteq \bigcup_{i=1}^{\infty} U_i,\ \operatorname{diam}(U_i) < \delta \right\}, \tag{1a}$$

where $\operatorname{diam}(U) = \sup_{\boldsymbol{x},\boldsymbol{y}\in U} |\boldsymbol{x} - \boldsymbol{y}|$ for any $U \subset \mathbb{R}^n$. Second, we take

$$\mathcal{H}^m(A) = \lim_{\delta \to 0} \mathcal{H}^m_\delta(A) = \sup_{\delta > 0} \mathcal{H}^m_\delta(A). \tag{1b}$$

As in [56, Definition 2.1], we define $\mathcal{H}^m$ with a scaling constant α_m so that $\mathcal{H}^1$ coincides with the usual definition of arc length ($\alpha_1 = 1$), $\mathcal{H}^2$ coincides with the usual definition of surface area, etc. Integration with respect to the Hausdorff measure is written with the notation $\int \mathrm{d}\mathcal{H}^m(\boldsymbol{x})$.

For any $A \subset \mathbb{R}^n$, we define $\operatorname{dist}(\cdot, A) : \mathbb{R}^n \to \mathbb{R}$ as the distance function to A. That is, for any $\boldsymbol{x} \in \mathbb{R}^n$,

$$\operatorname{dist}(\boldsymbol{x}, A) = \inf_{\boldsymbol{z}\in A} |\boldsymbol{x} - \boldsymbol{z}|.$$

We let $\mathcal{N}_\rho(A) \subset \mathbb{R}^n$ denote the ρ-neighborhood of A, or

$$\mathcal{N}_\rho(A) = \{\boldsymbol{x} \in \mathbb{R}^n \ : \ \operatorname{dist}(\boldsymbol{x}, A) < \rho\}.$$

Let $\mathcal{B}$ be an open subset of $\mathbb{R}^n$. For non-negative integer k, we let $C^k(\mathcal{B}; \mathbb{R}^m)$ denote the space of functions $\boldsymbol{f} : \mathcal{B} \to \mathbb{R}^m$ whose derivatives up to order k are continuous. The space $C^\infty(\mathcal{B}; \mathbb{R}^m)$ contains the functions with all derivatives continuous, while $C^\infty_c(\mathcal{B}; \mathbb{R}^m) \subset C^\infty(\mathcal{B}; \mathbb{R}^m)$ are those functions which are compactly supported in $\mathcal{B}$. We let $L^2(\mathcal{B}; \mathbb{R}^m)$ denote the space of functions for which $\int_\mathcal{B} |\boldsymbol{f}|^2 \,\mathrm{d}\boldsymbol{x} < \infty$ and $H^1(\mathcal{B}; \mathbb{R}^m) \subset L^2(\mathcal{B}; \mathbb{R}^m)$ be the space of functions for which $\int_\mathcal{B} |\nabla \boldsymbol{f}|^2 \,\mathrm{d}\boldsymbol{x} < \infty$, where the derivative is defined in the distributional sense. Finally, let $L^\infty(\mathcal{B}; \mathbb{R}^m)$ be the space of functions which have finite essential supremum (roughly, which are bounded), $\operatorname{ess\,sup}_{\boldsymbol{x}\in\mathcal{B}} |\boldsymbol{f}(\boldsymbol{x})| < \infty$. The usual norms on these spaces are denoted by $\|\cdot\|_{L^2(\mathcal{B};\mathbb{R}^m)}$, $\|\cdot\|_{H^1(\mathcal{B};\mathbb{R}^m)}$, and $\|\cdot\|_{L^\infty(\mathcal{B};\mathbb{R}^m)}$, respectively.

When referring to functions of time and space, e.g. $f(t, \boldsymbol{x})$, we will use the notation $f(t)$ in place of $f(t, \cdot)$ to refer to the function evaluated at time t.

3. Theory

3.1. Variational principle of fracture

The concept of fracture toughness in elastic, brittle materials stems from the seminal work of Griffith [39]. Griffith postulated that there was an energy cost to the creation of new crack surfaces, proportional to the new surface area, and that this cost must be paid by releasing stored elastic energy in the body. With respect to an infinitesimal extension of a crack, Griffith's criterion states that the stored energy release rate must be equal to a material constant. This notion implies a balance of energy during crack growth.

In Griffith's original work, the material constant is twice the surface free energy of the bulk material, as the insertion of a crack creates two free surfaces which are assumed to perfectly coincide in the undeformed configuration.[1] In this work, we will refer to Griffith's material constant as the "fracture toughness," accounting for the crack surface as a single surface instead of two identical crack faces.[2]

Francfort and Marigo [44] introduced variational fracture theory (VFT) as an extension of Griffith's theory. Rather than considering the energetics of a single crack tip, a key postulate of VFT is that the solid deforms and cracks to (globally) minimize the total free energy, which is comprised of two parts: *(i)* the energy corresponding to elastic deformation and the work of applied external forces; and *(ii)* the energy needed to produce the crack surfaces. Respectively, we call these the "elastic energy" and "surface energy." The relaxed conditions on the admissible cracks naturally allow for crack nucleation and the formation of other complex morphologies (such as crack branching, merging, etc.) to be captured.

Mathematically, the variational principle is stated as follows, see Fig. 2(a.i). We consider an elastic domain $\mathcal{B} \subset \mathbb{R}^{n3}$ which is subjected to applied displacements $\hat{\boldsymbol{u}}$ on a portion of the boundary $\partial\mathcal{B}_u \subseteq \partial\mathcal{B}$. Then, the crack set Γ and displacement field $\boldsymbol{u}$ minimize the energy

$$\Pi(\boldsymbol{u}, \Gamma) = \int_{\mathcal{B}\setminus\Gamma} W(\boldsymbol{x}, \boldsymbol{\epsilon}(\boldsymbol{u}))\, \mathrm{d}\boldsymbol{x} + g\mathcal{H}^{n-1}(\Gamma), \tag{2}$$

where $W(\boldsymbol{x}, \boldsymbol{\epsilon}) \geq 0$ is the strain energy density, $\boldsymbol{\epsilon}(\boldsymbol{u}) := (\nabla\boldsymbol{u} + \nabla\boldsymbol{u}^T)/2$ is the symmetrized displacement gradient (i.e., small-strain tensor), and $g > 0$ is the fracture toughness.

For simplicity, we assume an isotropic, linear elastic constitutive response

$$W(\boldsymbol{x}, \boldsymbol{\epsilon}) = \frac{1}{2}\lambda(\boldsymbol{x})\,\mathrm{tr}[\boldsymbol{\epsilon}]^2 + \mu(\boldsymbol{x})|\boldsymbol{\epsilon}|^2, \tag{3}$$

where $\mathrm{tr}[\cdot]$ is the trace of a tensor and $|\cdot|$ is the Frobenius norm of a tensor. The coefficients λ and μ are the Lamé parameters, but we may also discuss the elastic behavior in terms of Young's modulus E and Poisson's ratio ν. We allow these (strictly positive) coefficients to vary spatially to include situations like a crack along a bi-material interface, see §6.2.

[1] At smaller scales, this assumption may not be valid, as the surface roughness and fragmentation of material in between the crack faces can mean that the surface areas do not exactly coincide.

[2] Another common name for Griffith's material constant is the "critical energy release rate," while "fracture toughness" is also used for a critical value of the stress intensity factor around a crack tip. Since we do not refer to the critical stress intensity value in this work, we do not anticipate confusion in our terminology.

[3] We predominantly consider the $n = 2$ case but will also briefly explore the $n = 1$ case.

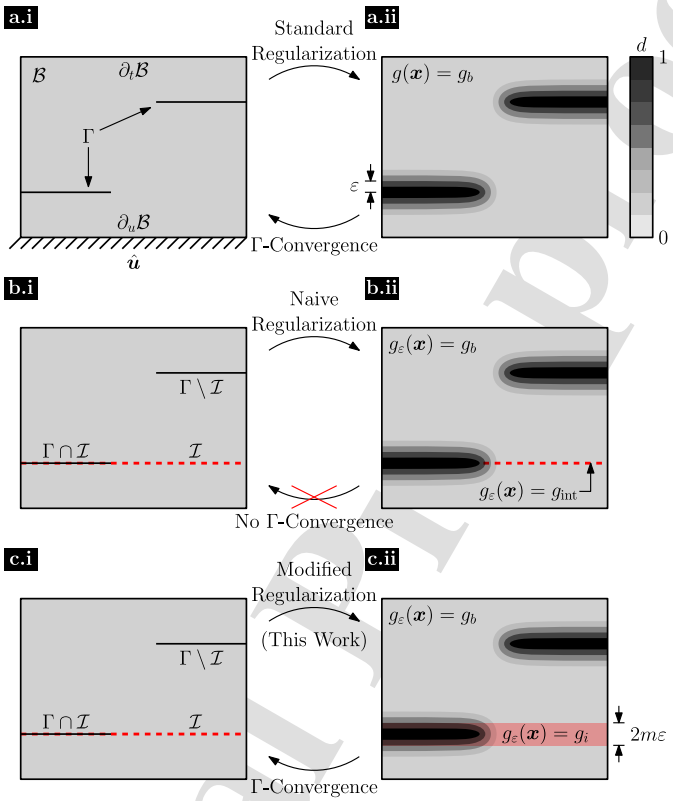

Figure 2: Schematic representation of the interface fracture problem and its regularization. (a.i) Original variational fracture problem with no weak interfaces, crack set Γ, and applied Dirichlet boundary conditions. (a.ii) Standard regularization approach for the problem in (a.i), which replaces the crack set by a continuous damage field d taking value between 0 and 1. The damage field has characteristic length scale ε. The standard regularization Γ-converges to the original problem as $\varepsilon \to 0$. (b.i) Variational fracture problem with a weak interface $\mathcal{I}$. (b.ii) Naive approach to regularize the problem in (b.i) using standard regularization practices. The regularized problem has the same fracture toughness distribution $g(\boldsymbol{x})$ as that of the original problem. Because the weak interface has zero measure, it is invisible to the damage field, and hence we do not recover the original problem as $\varepsilon \to 0$. (c.i) Variational fracture problem with weak interface $\mathcal{I}$. (c.ii) The modified regularization approach proposed in this work. We modify the fracture toughness distribution by widening the weak interface by a factor of $2m\varepsilon$, and we assign a fracture toughness g_i therein.

An important question in the minimization of (2) is what are the admissible spaces for $\boldsymbol{u}$ and Γ. The rigorous answer to this question is that $\boldsymbol{u}$ should belong to the space of generalized special functions of bounded deformation, $GSBD(\mathcal{B};\mathbb{R}^n)$ [57, 58]. Imprecisely, this space contains all functions whose symmetrized distributional derivative is a measure composed of two parts: the first is an integrable function (i.e. $\boldsymbol{\epsilon}(\boldsymbol{u})$) over $\mathcal{B}$, while the second corresponds to the jump in $\boldsymbol{u}$ across its so-called jump set $J_{\boldsymbol{u}}$. We immediately identify the crack set Γ with $J_{\boldsymbol{u}}$. We refer the interested reader to [57, 58] for further details.

Lastly, the global minimizers of (2) may not be physically or experimentally relevant. However, the computation of the global minimizers of (2) is a valuable exercise for the following two reasons.

1. As mentioned in [44], local minimizers of the energy may be more experimentally relevant. However, there are cases where the local and global minimizers coincide. For example, in a double cantilever beam (DCB) specimen subjected to displacement-controlled loading, the elastic energy scales inversely with the cube of the crack length while the fracture energy grows linearly with crack length. The result is that the total energy is convex with respect to crack length, possessing a unique minimizer.
2. Numerical procedures aimed at solving the global minimization problem often follow a sequence of configurations that locally minimize, which can also provide some insights into the fracture process.

3.2. Regularization of the total energy

It is difficult to compute the minimizers of (2) because of the presence of both volumetric and surface energies. Borrowing from the ideas of image segmentation, Bourdin et al. [45] introduced the following regularization, see Fig. 2(a.ii). We define a scalar-valued function d and a length scale ε. We then seek minimizers $(\boldsymbol{u}, d)$ of the regularized energy

$$\Pi_\varepsilon(\boldsymbol{u}, d) = \int_{\mathcal{B}} \left((1-d)^2 + k_\varepsilon\right) W(\boldsymbol{x}, \boldsymbol{\epsilon}(\boldsymbol{u}))\, \mathrm{d}\boldsymbol{x} + \int_{\mathcal{B}} \frac{g}{2}\left(\frac{d^2}{\varepsilon} + \varepsilon|\nabla d|^2\right) \mathrm{d}\boldsymbol{x} \tag{4}$$

over the admissible spaces $\mathcal{U}_u = \left\{\boldsymbol{v} \in H^1(\mathcal{B};\mathbb{R}^n) \;:\; \boldsymbol{v} \equiv \hat{\boldsymbol{u}} \text{ on } \partial\mathcal{B}_u\right\}$ and $\mathcal{U}_d = H^1(\mathcal{B};\mathbb{R})$. In the previous equation, $k_\varepsilon > 0$ is a parameter which is small compared with ε.

We first note that the optimal d must take value between 0 and 1. These limits may be interpreted as pristine and fully-damaged material, respectively. Second, it has been shown (see [59, 60, 46]) that Π is the Γ-limit of Π_ε as $\varepsilon \to 0$. Consequently, the global minimizers of Π_ε converge to those of Π, which provides a rational approach to approximate the minimizers of Π.

3.3. Regularization with interfaces

In (2) and (4), we assumed a constant fracture toughness g throughout the domain. However, it is possible to have spatial variation in fracture toughness throughout $\mathcal{B}$. In particular, suppose there exists a weak interface $\mathcal{I} \subset \mathcal{B}$, which we assume to be a simple, rectifiable curve (or finite collection of curves) with fracture toughness g_{int}. Meanwhile, we suppose the remainder of the domain $\mathcal{B} \setminus \mathcal{I}$ has uniform fracture toughness $g_b > g_{\text{int}}$. Under the original variational principle, cracks may form along this interface, and the surface energy will be less than if the same crack formed elsewhere in the domain. For this fracture toughness distribution, the total energy is

$$\Pi(\boldsymbol{u}, \Gamma) = \int_{\mathcal{B}\setminus\Gamma} W(\boldsymbol{x}, \boldsymbol{\epsilon}(\boldsymbol{u}))\, \mathrm{d}\boldsymbol{x} + g_b \mathcal{H}^{n-1}(\Gamma \setminus \mathcal{I}) + g_{\text{int}} \mathcal{H}^{n-1}(\Gamma \cap \mathcal{I}). \tag{5}$$

In the previous equation, another way to write the surface energy terms is

$$\int_\Gamma g(\boldsymbol{x})\,\mathrm{d}\mathcal{H}^{n-1}(\boldsymbol{x}), \tag{6a}$$

where

$$g(\boldsymbol{x}) = \begin{cases} g_{\text{int}} & \boldsymbol{x} \in \mathcal{I}, \\ g_b & \text{otherwise.} \end{cases} \tag{6b}$$

Following the relationship between (4) and (2), and considering the expression for the surface energy in (6), we propose the following regularization of (5):

$$\Pi_\varepsilon(\boldsymbol{u}, d) = \int_{\mathcal{B}} \left((1-d)^2 + k_\varepsilon\right) W(\boldsymbol{x}, \boldsymbol{\epsilon}(\boldsymbol{u}))\,\mathrm{d}\boldsymbol{x} + \int_{\mathcal{B}} \frac{g_\varepsilon(\boldsymbol{x})}{2}\left(\frac{d^2}{\varepsilon} + \varepsilon|\nabla d|^2\right)\mathrm{d}\boldsymbol{x}. \tag{7a}$$

We are now faced with the question of what fracture toughness distribution $g_\varepsilon(\boldsymbol{x})$ we should use in order to recover (5) in the Γ-limit. Some options are as follows:

1. We can use the fracture toughness distribution (6b) for the sharp-crack problem (see Fig. 2(b)), i.e.
$$g_\varepsilon(\boldsymbol{x}) = g(\boldsymbol{x}).$$
However, this approach faces a critical issue. Because $g(\boldsymbol{x}) - g_b$ is nonzero only when $\boldsymbol{x} \in \mathcal{I}$, and $\mathcal{L}^n(\mathcal{I}) = 0$, then the second integral in (7a) is equal to that in (4). In other words, the damage field does not see the weak interface. Consequently, if we take the Γ-limit of Π_ε, the limiting Π will not have reduced fracture toughness at the interface.
2. In order for the damage field to be influenced by the weak interface, we must make the weak interface occupy a set with finite measure. For example, we can widen the weak interfaces by some thickness $2t > 0$:
$$g_\varepsilon(\boldsymbol{x}) = \begin{cases} g_{\text{int}} & \operatorname{dist}(\boldsymbol{x}, \mathcal{I}) \le t, \\ g_b & \text{otherwise,} \end{cases}$$
where $\operatorname{dist}(\boldsymbol{x}, \mathcal{I})$ is the distance between $\boldsymbol{x}$ and the interfaces $\mathcal{I}$. This approach yields fracture toughness heterogeneities akin to those explored in [31]. However, this approach no longer models a weak interface with negligible thickness. Hence, when we take the Γ-limit of Π_ε, we no longer recover (5).
3. In order to recover thin weak interfaces, we must have t shrink to zero along with ε. Our approach is to set $t = m\varepsilon$, where $m > 0$, see Fig. 2(c). We define
$$g_\varepsilon(\boldsymbol{x}) = \begin{cases} g_i & \operatorname{dist}(\boldsymbol{x}, \mathcal{I}) \le m\varepsilon, \\ g_b & \text{otherwise,} \end{cases} \tag{7b}$$
where g_i is determined from g_b, g_{int}, and m using:
$$g_i = \frac{\sqrt{(g_b - g_{\text{int}})^2 + 4 g_b g_{\text{int}} \tanh^2(m)} - (g_b - g_{\text{int}})}{2\tanh(m)}. \tag{7c}$$
This equation for g_i may seem arbitrary; however, as we will prove in §4, setting g_i in this way allows us to precisely recover the desired interface fracture toughness g_{int}.

For our proposed formulation, we remark that if we start with a regularized problem with widened interface g_i the limiting interface fracture toughness is given by

$$g_{\text{int}} = g_i \left(\frac{g_b + g_i \tanh(m)}{g_i + g_b \tanh(m)} \right), \tag{8}$$

which is the inverse of (7c). We observe from this formula that g_{int} varies monotonically from g_b when $m = 0$ (zero-width interface) to g_i when $m = \infty$ (the interface encapsulates the entire domain). Similarly, for a fixed m, (8) is a one-to-one function from g_i to $g_{\text{int}} < g_b$, meaning if we wish to model an interface with fracture toughness g_{int}, we can always find a suitable g_i.

4. Γ-convergence proof for the interface toughness

In this section, we prove that the functional Π_ε defined in (7) Γ-converges to the functional Π in (5). Before formally stating and proving this result, we present some technical details. Readers who are more interested in numerics and simulation examples may skip this section and continue in §5.

4.1. Technical details

We take the problem domain $\mathcal{B} \subset \mathbb{R}^2$ to be bounded and to have Lipschitz boundary. Meanwhile, the interface set $\mathcal{I} \subset \overline{\mathcal{B}}$ is assumed to be a finite union of rectifiable curves, $(I_i)_i$. Specifically, for each I_i, we assume that the arc-length parameterization $\boldsymbol{\gamma}_i : [0, \mathcal{H}^1(I_i)] \to \mathbb{R}^2$ is C^2-continuous and injective. Furthermore, for $j \neq i$, we request that $I_i \cap I_j \subset \{\boldsymbol{\gamma}_i(0), \boldsymbol{\gamma}_i(\mathcal{H}^1(I_i))\}$, with an identical condition holding for $I_i \cap \partial\mathcal{B}$. In other words, the individual curves comprising $\mathcal{I}$ may only intersect each other at their endpoints and only the endpoints of I_i are allowed to touch the domain boundary $\partial\mathcal{B}$. For each $s \in [0, \mathcal{H}^1(I_i)]$, we set $\hat{\boldsymbol{t}}_i(s) = \boldsymbol{\gamma}_i'(s)$ to be the unit tangent vector at $\boldsymbol{\gamma}_i(s)$, and we define the unit normal at the same point, $\hat{\boldsymbol{n}}_i(s)$, through 90° rotation of $\hat{\boldsymbol{t}}_i(s)$.[4] We sometimes abuse notation by writing $\hat{\boldsymbol{t}}_i(\boldsymbol{x})$ and $\hat{\boldsymbol{n}}_i(\boldsymbol{x})$ for $\boldsymbol{x} \in I_i$ instead of $\hat{\boldsymbol{t}}_i(\boldsymbol{\gamma}_i^{-1}(\boldsymbol{x}))$ and $\hat{\boldsymbol{n}}_i(\boldsymbol{\gamma}_i^{-1}(\boldsymbol{x}))$, respectively. For each curve, we may define the *signed* radius of curvature R_i as

$$\frac{1}{R_i(s)} = -\boldsymbol{\gamma}_i''(s) \cdot \hat{\boldsymbol{n}}_i(s). \tag{9}$$

Because of the regularity of the interface curves, there must exist a minimum radius of curvature over all s and over all curves,

$$R_{\min} = \min_i \min_{s \in [0, \mathcal{H}^1(I_i)]} |R_i(s)|. \tag{10}$$

Additionally, for each I_i, there exists $\rho_i > 0$ such that the coordinate map

$$(s, z) \mapsto \boldsymbol{\gamma}_i(s) + z\hat{\boldsymbol{n}}_i(s) \tag{11}$$

on the domain $[0, \mathcal{H}^1(I_i)] \times (-\rho_i, \rho_i)$ is a diffeomorphism (see [61, Theorem 2.2.5]). The image of $[0, \mathcal{H}^1(I_i)] \times (-\rho_i, \rho_i)$ under the map is called the tubular neighborhood of I_i. Moreover, it may be shown that $\rho_i \leq \min_{s \in [0, \mathcal{H}^1(I_i)]} |R_i(s)|$.

We next discuss the admissible function spaces for Π_ε and Π. For Π_ε, arguments $(\boldsymbol{u}, d)$ belong to $H^1(\mathcal{B}; \mathbb{R}^2) \times H^1(\mathcal{B}; \mathbb{R})$. The functional Π is defined over the set

$$\mathcal{A} = \left\{ \boldsymbol{u} \in L^\infty(\mathcal{B}; \mathbb{R}^2) \ : \ \boldsymbol{u}|_{\mathcal{B} \setminus \Gamma} \in H^1(\mathcal{B} \setminus \Gamma; \mathbb{R}^2), \, \Gamma \in \mathcal{C} \right\}, \tag{12}$$

where $\mathcal{C}$ is the set of all closed, $\mathcal{H}^1$-rectifiable subsets of $\overline{\mathcal{B}}$. Note that each $\boldsymbol{u} \in \mathcal{A}$ has a corresponding Γ (the Γ is not defined separately). For $\boldsymbol{u} \in \mathcal{A}$, we also request that $\boldsymbol{u}|_{\mathcal{B} \setminus \Gamma}$ be discontinuous across its corresponding Γ, except possibly at a countable number of points in Γ. In the parlance of $SBD(\mathcal{B}; \mathbb{R}^2)$, we say that Γ is the jump set of the function $\boldsymbol{u}$. We note that $\mathcal{A}$ is slightly more restrictive than $SBD(\mathcal{B}; \mathbb{R}^2)$; however, this space is suitable for the sorts of crack topologies that are expected in practical situations. We also remark that this set can be extended to functions whose crack set is not closed via the approximation results of Chambolle [62, Theorem 3].

[4] More precisely, we may find an orthogonal transformation $\boldsymbol{Q} : \mathbb{R}^2 \to \mathbb{R}^2$ such that $\boldsymbol{v} \cdot (\boldsymbol{Q}\boldsymbol{v}) = 0$ for any $\boldsymbol{v} \in \mathbb{R}^2$. Then, we set $\hat{\boldsymbol{n}}_i(s) = \boldsymbol{Q}\hat{\boldsymbol{t}}_i(s)$ for each $s \in [0, \mathcal{H}^1(I_i)]$ and for each i.

4.2. Statement of the Theorem

Theorem 1. *Let $(\varepsilon_n)_n$ be a sequence of positive real numbers which converges to zero. Then the sequence of functionals $(\Pi_{\varepsilon_n})_n$ Γ-converges to Π. That is, for any $\boldsymbol{u} \in \mathcal{A}$ (with corresponding set Γ), the following hold.*

i. *(Γ-lim inf) For any sequences $(\boldsymbol{u}_n)_n \subset H^1(\mathcal{B};\mathbb{R}^2)$ and $(d_n)_n \subset H^1(\mathcal{B};\mathbb{R})$ such that $\boldsymbol{u}_n \to \boldsymbol{u}$ in $L^2(\mathcal{B};\mathbb{R}^2)$, we have*

$$\liminf_{n\to\infty} \Pi_{\varepsilon_n}[\boldsymbol{u}_n, d_n] \geq \Pi[\boldsymbol{u}, \Gamma]. \tag{13}$$

ii. *(Γ-lim sup) There exists sequences $(\boldsymbol{u}_n)_n \subset H^1(\mathcal{B};\mathbb{R}^2)$ and $(d_n)_n \subset H^1(\mathcal{B};\mathbb{R})$ such that $\boldsymbol{u}_n \to \boldsymbol{u}$ in $L^2(\mathcal{B};\mathbb{R}^2)$ and*

$$\limsup_{n\to\infty} \Pi_{\varepsilon_n}[\boldsymbol{u}_n, d_n] \leq \Pi[\boldsymbol{u}, \Gamma]. \tag{14}$$

In the following sections, we separately prove each of the two items in the above theorem.

4.3. Proof of Γ-lim inf

Before we prove Theorem 1(i), we require some preliminary results. For brevity, we leave the proofs to the appendices.

The first result concerns the portions of the tubular neighborhood of each I_i which do not overlap with the tubular neighborhood belonging to another I_j or with $\partial\mathcal{B}$.

Proposition 2. *For any $\rho > 0$, let $\ell_{i\boldsymbol{x}\rho}$ be the segment of length 2ρ, centered at point $\boldsymbol{x} \in I_i$ and orthogonal to I_i, i.e.,*

$$\ell_{i\boldsymbol{x}\rho} = \{\boldsymbol{x} + z\hat{\boldsymbol{n}}_i(\boldsymbol{x}) \ : \ z \in (-\rho, \rho)\}.$$

For each i, define $J_i = \partial\mathcal{B} \cup \left(\bigcup_{j\neq i} I_j\right) \cup \{\boldsymbol{\gamma}_i(0), \boldsymbol{\gamma}_i(\mathcal{H}^1(I_i))\}$. Then, for

$$0 < \rho < \min_i \left\{ \min\left\{ \rho_i, \max_{0\leq s\leq \mathcal{H}^1(I_i)} \frac{\operatorname{dist}(\boldsymbol{\gamma}_i(s), J_i)}{3} \right\} \right\}$$

the sets $(A_{i\rho})_i$ with

$$A_{i\rho} := \boldsymbol{\gamma}_i\big(\{s \in [0, \mathcal{H}^1(I_i)] : \operatorname{dist}(\boldsymbol{\gamma}_i(s), J_i) > 3\rho\}\big)$$

are nonempty and have the following properties.

1. *For any $\boldsymbol{x} \in A_{i\rho}$, $\ell_{i\boldsymbol{x}\rho} \cap \ell_{j\boldsymbol{y}\rho} = \emptyset$ for any $\boldsymbol{y} \in I_j$ (including the case where $j = i$ and $\boldsymbol{y} \neq \boldsymbol{x}$) and $\ell_{i\boldsymbol{x}\rho} \cap \partial\mathcal{B} = \emptyset$.*
2. *For any $\boldsymbol{x} \in A_{i\rho}$ and $\boldsymbol{y} \in \ell_{i\boldsymbol{x}\rho}$, $\operatorname{dist}(\boldsymbol{y}, \mathcal{I}) = \operatorname{dist}(\boldsymbol{y}, I_i) = |\boldsymbol{y} - \boldsymbol{x}|$.*
3. *As ρ decreases to 0,*

$$\lim_{\rho\to 0+} \mathcal{H}^1(I_i \setminus A_{i\rho}) = 0,$$

so that

$$\lim_{\rho\to 0+} \mathcal{H}^1(\Gamma \cap A_{i\rho}) = \mathcal{H}^1(\Gamma \cap I_i).$$

The second result is a specialized Γ-lim inf result for the one-dimensional domain $\mathcal{B} = (-\rho, \rho)$ containing a crack at $z = 0$.

Proposition 3 (One-dimensional Γ-lim inf)**.** *Suppose $u \in L^2((-\rho,\rho);\mathbb{R})$, but $u|_{(-\delta,\delta)} \notin H^1((-\delta,\delta);\mathbb{R})$ for any $0 < \delta \le \rho$. Let $(u_n)_n, (d_n)_n \subset H^1((-\rho,\rho);\mathbb{R})$ be such that $u_n \to u$ in $L^2((-\rho,\rho);\mathbb{R})$. Then, for any constant $C > 0$,*

$$\liminf_{n\to\infty} \left[\int_{-\rho}^{\rho} (1-d_n)^2 C (u_n')^2 \,\mathrm{d}z + \int_{-\rho}^{\rho} \frac{\overline{g}(z/\varepsilon_n)}{2} \left(\frac{d_n^2}{\varepsilon_n} + \varepsilon_n (d_n')^2 \right) \mathrm{d}z \right] \ge g_{\mathrm{int}}, \tag{15a}$$

where

$$\overline{g}(t) := \begin{cases} g_i & \text{if } |t| \le m, \\ g_b & \text{otherwise.} \end{cases} \tag{15b}$$

We remark that in our formulation (7b), $g_\varepsilon(\boldsymbol{x}) = \overline{g}(\mathrm{dist}(\boldsymbol{x},\mathcal{I})/\varepsilon)$. With these results, we are now ready for the proof.

Proof of Theorem 1(i).

1. Without loss of generality, assume that the sequences $(\boldsymbol{u}_n, d_n)_n$ are such that
$$\liminf_{n\to\infty} \Pi_{\varepsilon_n}[\boldsymbol{u}_n, d_n] < \infty.$$
Otherwise, it is trivial to bound the limit inferior from below by any finite value we choose. Also, without loss of generality, we may assume that $(\varepsilon_n)_n$ is a strictly decreasing sequence.
2. Fix $\rho > 0$ (which will be specified later) and consider the ρ-neighborhood of $\mathcal{I}$. We partition the domain into $\mathcal{B} \setminus \mathcal{N}_\rho(\mathcal{I})$ and $\mathcal{N}_\rho(\mathcal{I}) \cap \mathcal{B}$, and we apply superadditivity of the limit inferior:
$$\liminf_{n\to\infty} \Pi_{\varepsilon_n}[\boldsymbol{u}_n, d_n] \ge \liminf_{n\to\infty} \Pi_{\varepsilon_n}[\boldsymbol{u}_n, d_n, \mathcal{B} \setminus \mathcal{N}_\rho(\mathcal{I})] + \liminf_{n\to\infty} \Pi_{\varepsilon_n}[\boldsymbol{u}_n, d_n, \mathcal{N}_\rho(\mathcal{I}) \cap \mathcal{B}], \tag{16}$$
where for a subset $\Omega \subseteq \mathcal{B}$ we define $\Pi_\varepsilon[\cdot,\cdot,\Omega]$ to be the same as in (4), but integrated over Ω instead of $\mathcal{B}$. As $\varepsilon_n \to 0$, we will eventually have $m\varepsilon_n < \rho$, so that $\mathcal{N}_{m\varepsilon_n}(\mathcal{I}) \subset \mathcal{N}_\rho(\mathcal{I})$. Going forward, we assume n is sufficiently large so that this is the case.
3. We consider separately each of the two terms on the right-hand-side of (16). For the first term, since we have cut out the widened interfaces, $g_\varepsilon(\boldsymbol{x}) \equiv g_b$ in $\mathcal{B} \setminus \mathcal{N}_\rho(\mathcal{I})$. In this domain, we may apply standard Γ-convergence results such as [62, Theorem 4]:
$$\liminf_{n\to\infty} \Pi_{\varepsilon_n}[\boldsymbol{u}_n, d_n, \mathcal{B} \setminus \mathcal{N}_\rho(\mathcal{I})] \ge \int_{\mathcal{B}\setminus(\Gamma\cup\mathcal{N}_\rho(\mathcal{I}))} W(\boldsymbol{x}, \boldsymbol{\epsilon}(\boldsymbol{u}))\,\mathrm{d}\boldsymbol{x} + g_b \mathcal{H}^1(\Gamma \setminus \mathcal{N}_\rho(\mathcal{I})).$$
4. For the second term of (16), let us choose a subsequence $(\boldsymbol{u}_{n_k}, d_{n_k})_k$ of $(\boldsymbol{u}_n, d_n)_n$ for which.
$$\lim_{k\to\infty} \Pi_{\varepsilon_{n_k}}[\boldsymbol{u}_{n_k}, d_{n_k}, \mathcal{N}_\rho(\mathcal{I}) \cap \mathcal{B}] = \liminf_{n\to\infty} \Pi_{\varepsilon_n}[\boldsymbol{u}_n, d_n, \mathcal{N}_\rho(\mathcal{I}) \cap \mathcal{B}].$$
Going forward, we will abuse notation by referring to the subsequence as $(\boldsymbol{u}_n, d_n)_n$. Next, apply Proposition 2 to construct the sets $(A_{i\rho})_i$. We recall that each set $A_{i\rho}$ contains all points $\boldsymbol{x} \in I_i$ such that the orthogonal segment $\ell_{i\boldsymbol{x}\rho} := \{\boldsymbol{x} + z\hat{\boldsymbol{n}}_i(\boldsymbol{x}) \ : \ z \in (-\rho,\rho)\}$ does not intersect $\partial\mathcal{B}$ or any other orthogonal segment $\ell_{j\boldsymbol{y}\rho}$ with $\boldsymbol{y} \in I_j$ (which includes $\boldsymbol{y} \in I_i$). Let $\mathcal{T}_{i\rho} = \{\ell_{i\boldsymbol{x}\rho} \ : \ \boldsymbol{x} \in \Gamma \cap A_{i\rho}\} \subset \mathcal{N}_\rho(\mathcal{I}) \cap \mathcal{B}$. We assume that $\rho < R_{\min}$ is sufficiently small enough that each $A_{i\rho}$ (and hence $\mathcal{T}_{i\rho}$) is not empty. By construction, $\mathcal{T}_{i\rho} \cap \mathcal{T}_{j\rho} = \emptyset$ when $i \ne j$. Then, we trivially have
$$\Pi_{\varepsilon_n}[\boldsymbol{u}_n, d_n, \mathcal{N}_\rho(\mathcal{I}) \cap \mathcal{B}] \ge \Pi_{\varepsilon_n}[\boldsymbol{u}_n, d_n, (\cup_i \mathcal{T}_{i\rho})] = \sum_i \Pi_{\varepsilon_n}[\boldsymbol{u}_n, d_n, \mathcal{T}_{i\rho}].$$

5. We briefly discuss integration within each $\mathcal{T}_{i\rho}$. We use the coordinate map (11) defined for $(s,z) \in [0, \mathcal{H}^1(I_i)] \times (-\rho, \rho)$, which has Jacobian

$$1 + \frac{z}{R_i(s)} \geq 1 - \frac{\rho}{R_{\min}} > 0,$$

where the first inequality is a consequence of (10) and the second inequality is because ρ is chosen to be smaller than $R_{\min}$. Then, for any integrand $f(\boldsymbol{x})$, going to coordinates gives

$$\int_{\mathcal{T}_{i\rho}} f(\boldsymbol{x})\,\mathrm{d}\boldsymbol{x} = \int_{\boldsymbol{\gamma}_i^{-1}(\Gamma\cap A_{i\rho})} \int_{-\rho}^{\rho} f(\boldsymbol{x}(s,z)) \left(1 + \frac{z}{R_i(s)}\right) \mathrm{d}z\mathrm{d}s.$$

Using the lower bound on the Jacobian, we have

$$\int_{\mathcal{T}_{i\rho}} f(\boldsymbol{x})\,\mathrm{d}\boldsymbol{x} \geq \left(1 - \frac{\rho}{R_{\min}}\right) \int_{\boldsymbol{\gamma}_i^{-1}(\Gamma\cap A_{i\rho})} \int_{-\rho}^{\rho} f(\boldsymbol{x}(s,z))\,\mathrm{d}z\mathrm{d}s.$$

In this way, we have transformed an integral over $\mathcal{T}_{i\rho}$ into an integral over the rectangles $\boldsymbol{\gamma}_i^{-1}(\Gamma \cap A_{i\rho}) \times (-\rho, \rho)$.

6. As shorthand, let us denote the two functionals in (4) as Π_ε^e and Π_ε^f, respectively, for the elastic and surface energy terms. We may extend the normal vector $\hat{\boldsymbol{n}}_i$ away from I_i and into $\mathcal{T}_{i\rho}$ through the coordinate map; abusing notation, we have $\hat{\boldsymbol{n}}_i(\boldsymbol{x}(s,z)) = \hat{\boldsymbol{n}}_i(s)$. Then, for Π_ε^e we trivially have

$$\Pi_{\varepsilon_n}^e[\boldsymbol{u}_n, d_n, \mathcal{T}_{i\rho}] \geq \int_{\mathcal{T}_{i\rho}} (1-d_n)^2 C_{\lambda\mu} |\hat{\boldsymbol{n}}_i \cdot \nabla \boldsymbol{u}_n \cdot \hat{\boldsymbol{n}}_i|^2\,\mathrm{d}\boldsymbol{x},$$

were $C_{\lambda\mu}$ is a constant depending on the elastic moduli such that $W(\boldsymbol{x}, \boldsymbol{\epsilon}(\boldsymbol{u})) \geq C_{\lambda\mu}|\boldsymbol{\epsilon}(\boldsymbol{u})|^2$.[5] In the above, we also used the fact that $|\boldsymbol{\epsilon}(\boldsymbol{u})| \geq |\boldsymbol{v} \cdot \nabla \boldsymbol{u} \cdot \boldsymbol{v}|$ for any unit vector $\boldsymbol{v}$.

7. Following Step 5, we go to coordinates. Let us define the scalar function $u_{zn}(s,z) = \boldsymbol{u}_n(\boldsymbol{x}(s,z)) \cdot \hat{\boldsymbol{n}}_i(\boldsymbol{x}(s,z))$ and abuse notation by writing $d_n(s,z) = d_n(\boldsymbol{x}(s,z))$. Then, $\partial u_{zn}/\partial z = \hat{\boldsymbol{n}}_i \cdot \nabla \boldsymbol{u}_n \cdot \hat{\boldsymbol{n}}_i$, and so

$$\Pi_{\varepsilon_n}^e[\boldsymbol{u}_n, d_n, \mathcal{T}_{i\rho}] \geq \left(1 - \frac{\rho}{R_{\min}}\right) \int_{\boldsymbol{\gamma}_i^{-1}(\Gamma\cap A_{i\rho})} \int_{-\rho}^{\rho} (1-d_n)^2 C_{\lambda\mu} \left|\frac{\partial u_{zn}}{\partial z}\right|^2 \mathrm{d}z\mathrm{d}s.$$

8. Similarly, for Π_ε^f, we note that $|\nabla d_n| \geq |\nabla d_n \cdot \hat{\boldsymbol{n}}_i| = |\partial d_n/\partial z|$, and so

$$\Pi_{\varepsilon_n}^f[\boldsymbol{u}_n, d_n, \mathcal{T}_{i\rho}] \geq \left(1 - \frac{\rho}{R_{\min}}\right) \int_{\boldsymbol{\gamma}_i^{-1}(\Gamma\cap A_{i\rho})} \int_{-\rho}^{\rho} \frac{\overline{g}(z/\varepsilon_n)}{2} \left(\frac{d_n^2}{\varepsilon_n} + \varepsilon_n \left|\frac{\partial d_n}{\partial z}\right|^2\right) \mathrm{d}z\mathrm{d}s.$$

In the previous inequality, we used the fact that $g_{\varepsilon_n}(\boldsymbol{x}) = \overline{g}(\mathrm{dist}(\boldsymbol{x}, \mathcal{I})/\varepsilon_n)$, where $\overline{g}$ is defined in (15b), and $\mathrm{dist}(\boldsymbol{x}, \mathcal{I})$ is precisely precisely z for points in $\mathcal{T}_{i\rho}$ (see Proposition 2).

[5] The constant $C_{\lambda\mu}$ is precisely the minimum eigenvalue of the fourth-order elasticity tensor $\mathbb{C}$, which is defined so that (3) is equivalent to $W(\boldsymbol{x}, \boldsymbol{\epsilon}(\boldsymbol{u})) = \frac{1}{2}\boldsymbol{\epsilon}(\boldsymbol{u}) : (\mathbb{C}(\boldsymbol{x}) : \boldsymbol{\epsilon}(\boldsymbol{u}))$.

9. Let $\Theta = \boldsymbol{\gamma}_i^{-1}(\Gamma \cap A_{i\rho}) \times (-\rho, \rho)$ be the parametric domain for (s, r). Then, $u_{zn}, d_n \in H^1(\Theta; \mathbb{R})$ and $u_z := \boldsymbol{u} \cdot \hat{\boldsymbol{n}}_i$ belongs to $L^2(\Theta; \mathbb{R})$. We now apply two slicing results. First, by the slicing property of H^1 functions (see [56, Theorem 4.21]), for almost-every $s \in \boldsymbol{\gamma}_i^{-1}(\Gamma \cap A_{i\rho})$, the restrictions of u_{zn} and d_n[6] to the segment $\{s\} \times (-\rho, \rho)$, which we call $u_{zn}|_s$ and $d_n|_s$, respectively, belong to $H^1((-\rho, \rho); \mathbb{R})$; moreover, $(u_{zn}|_s)'$ and $(d_n|_s)'$ coincide for almost every $z \in (-\rho, \rho)$ with $\partial u_{zn}/\partial z$ and $\partial d_n/\partial z$. Second, via Fubini's Theorem and [56, Theorem 1.21], there exists a subsequence $(u_{zn_k}, d_{n_k})_k$ of $(u_{zn}, d_n)_n$ for which $u_{zn_k}|_s$ converges in $L^2((-\rho, \rho); \mathbb{R})$ to $u_z|_s$ for almost every $s \in \boldsymbol{\gamma}_i^{-1}(\Gamma \cap A_{i\rho})$. Moreover, because of the assumptions on $\boldsymbol{u} \in \mathcal{A}$, we know that $u_z|_s$ must be discontinuous across the crack set, in particular $z = 0$. Finally, as before, we abuse notation and refer to the subsequence as $(u_{zn}, d_n)_n$.
10. For almost every $s \in \boldsymbol{\gamma}_i^{-1}(\Gamma \cap A_{i\rho})$, if we define

$$f_n(s) := \int_{-\rho}^{\rho} (1 - d_n|_s)^2 C_{\lambda\mu}((u_{zn}|_s)')^2 \,\mathrm{d}z + \int_{-\rho}^{\rho} \frac{\overline{g}(z/\varepsilon_n)}{2} \left(\frac{(d_n|_s)^2}{\varepsilon_n} + \varepsilon_n((d_n|_s)')^2 \right) \mathrm{d}z,$$

then by the one-dimensional Γ-liminf result, Proposition 3, we have

$$\liminf_{n\to\infty} f_n(s) \geq g_{\mathrm{int}}.$$

Applying Fatou's lemma (and the sub-additivity of the lim inf), we have

$$\begin{aligned} \liminf_{n\to\infty} \int_{\boldsymbol{\gamma}_i^{-1}(\Gamma\cap A_{i\rho})} f_n(s) \,\mathrm{d}s &\geq \int_{\boldsymbol{\gamma}_i^{-1}(\Gamma\cap A_{i\rho})} \liminf_{n\to\infty} f_n(s) \,\mathrm{d}s \\ &\geq \int_{\boldsymbol{\gamma}_i^{-1}(\Gamma\cap A_{i\rho})} g_{\mathrm{int}} \,\mathrm{d}s \\ &= g_{\mathrm{int}} \mathcal{H}^1(\Gamma \cap A_{i\rho}). \end{aligned}$$

11. By the choice of subsequences in Steps 4 and 9, we have that

$$\liminf_{n\to\infty} \Pi_{\varepsilon_n}[\boldsymbol{u}_n, d_n, \mathcal{N}_\rho(\mathcal{I}) \cap \mathcal{B}] \geq \left(1 - \frac{\rho}{R_{\min}}\right) g_{\mathrm{int}} \sum_i \mathcal{H}^1(\Gamma \cap A_{i\rho}).$$

12. Finally, we put together the estimates for $\mathcal{B} \setminus \mathcal{N}_\rho(\mathcal{I})$ and $\mathcal{N}_\rho(\mathcal{I}) \cap \mathcal{B}$:

$$\liminf_{n\to\infty} \Pi_{\varepsilon_n}[\boldsymbol{u}_n, d_n] \geq \int_{\mathcal{B}\setminus(\Gamma\cup\mathcal{N}_\rho(\mathcal{I}))} W(\boldsymbol{x}, \boldsymbol{\epsilon}(\boldsymbol{u})) \,\mathrm{d}\boldsymbol{x} + g_b \mathcal{H}^1(\Gamma \setminus \mathcal{N}_\rho(\mathcal{I})) + \left(1 - \frac{\rho}{R_{\min}}\right) g_{\mathrm{int}} \sum_i \mathcal{H}^1(\Gamma \cap A_{i\rho}).$$

Since the left-hand-side is independent of ρ, we may shrink ρ to zero. We proceed term by term:

(a) The strain energy density $W(\cdot, \boldsymbol{\epsilon}(\boldsymbol{u}))$ belongs to $L^1(\mathcal{B} \setminus \Gamma; \mathbb{R})$ and is non-negative. Thus, $\mathcal{L}^2 \llcorner W(\cdot, \boldsymbol{\epsilon}(\boldsymbol{u}))$ is a measure on subsets of $\mathcal{B} \setminus \Gamma$ (cf. [63, §3.2]). Because

$$\bigcup_{\rho>0} \mathcal{B} \setminus (\Gamma \cup \mathcal{N}_\rho) = \mathcal{B} \setminus (\Gamma \cup \mathcal{I}),$$

[6] More precisely, there are representatives in the equivalence classes of u_{zn} and d_n for which this property holds; however, we abuse notation and do not distinguish between the representative and the equivalence class.

by continuity of measures on nested sets, we have

$$\lim_{\rho\to 0+}\int_{\mathcal{B}\setminus(\Gamma\cup\mathcal{N}_\rho(\mathcal{I}))} W(\boldsymbol{x},\boldsymbol{\epsilon}(\boldsymbol{u}))\,\mathrm{d}\boldsymbol{x} = \int_{\mathcal{B}\setminus(\Gamma\cup\mathcal{I})} W(\boldsymbol{x},\boldsymbol{\epsilon}(\boldsymbol{u}))\,\mathrm{d}\boldsymbol{x} = \int_{\mathcal{B}\setminus\Gamma} W(\boldsymbol{x},\boldsymbol{\epsilon}(\boldsymbol{u}))\,\mathrm{d}\boldsymbol{x}.$$

For the last equality, we used the fact that any function $f \in L^1(\mathcal{B}\setminus(\Gamma\cup\mathcal{I});\mathbb{R})$ also belongs to $L^1(\mathcal{B}\setminus\Gamma;\mathbb{R})$, since $\mathcal{L}^2(\mathcal{I})=0$ and we may arbitrarily define values for f along $\mathcal{I}$ without changing the integral.

(b) Similarly, for the nesting sets $(\Gamma\setminus\mathcal{N}_\rho(\mathcal{I}))_\rho$, continuity of the Hausdorff measure gives

$$\lim_{\rho\to 0+}\mathcal{H}^1(\Gamma\setminus\mathcal{N}_\rho(\mathcal{I})) = \mathcal{H}^1(\Gamma\setminus\mathcal{I}).$$

(c) Since $R_{\min}$ is independent of ρ,

$$\lim_{\rho\to 0+}\left(1-\frac{\rho}{R_{\min}}\right)=1.$$

(d) Finally, by construction of $A_{i\rho}$, we have

$$\lim_{\rho\to 0+}\sum_i \mathcal{H}^1(\Gamma\cap A_{i\rho}) = \sum_i \mathcal{H}^1(\Gamma\cap I_i) = \mathcal{H}^1(\Gamma\cap\mathcal{I}).$$

Hence

$$\liminf_{n\to\infty}\Pi_{\varepsilon_n}[\boldsymbol{u}_n,d_n] \geq \int_{\mathcal{B}\setminus\Gamma} W(\boldsymbol{x},\boldsymbol{\epsilon}(\boldsymbol{u}))\,\mathrm{d}\boldsymbol{x} + g_b\mathcal{H}^1(\Gamma\setminus\mathcal{I}) + g_{\mathrm{int}}\mathcal{H}^1(\Gamma\cap\mathcal{I}).$$

as desired.

□

4.4. Proof of Γ-lim sup

Next, we prove Theorem 1(ii). We require a preliminary result for this step, the proof of which is left to the appendices, which concerns the arc length of the boundary of the ρ-neighborhood of a C^2 curve.

Proposition 4. *For any I_i, let $0\leq s_1<s_2\leq\mathcal{H}^1(I_i)$. Then, for $\rho<R_{\min}$,*

$$\mathcal{H}^1(\partial\mathcal{N}_\rho(\boldsymbol{\gamma}_i([s_1,s_2]))) \leq 4\pi\rho + 2\left(1+\frac{\rho}{R_{\min}}\right)\mathcal{H}^1(\boldsymbol{\gamma}_i([s_1,s_2]))$$

We are now ready for the proof. Throughout this proof, we make use of the Γ-convergence proof of Chambolle [62, Theorem 4] for domains with constant fracture toughness.

Proof of Theorem 1(ii).

1. Without loss of generality, we assume that for each I_i, the set $\Gamma \cap I_i$ may be decomposed into the images of J_i disjoint closed intervals contained in $[0, \mathcal{H}^1(I_i)]$, $(\boldsymbol{\gamma}_i([s_{j1}, s_{j2}]))_{j=1}^{J_i}$.[7] Let $(\Gamma_j)_j$ be the collection of all the subsets over all I_i, and let $J = \sum_i J_i$ be the total number of subsets. Because the subsets are disjoint for each I_i, while I_i and I_j may intersect only at their endpoints, $\mathcal{H}^1(\Gamma \cap \mathcal{I}) = \sum_j \mathcal{H}^1(\Gamma_j)$.
2. Construct a sequence $(\alpha_n)_n$ converging to 0 such that $\alpha_n = o(\varepsilon_n)$, ensuring $k_{\varepsilon_n} = o(\alpha_n)$ as in [62, Theorem 4].
3. We now construct the recovery sequences $(\boldsymbol{u}_n)_n$ and $(d_n)_n$. As in [62, Theorem 4], define

$$\boldsymbol{u}_n(\boldsymbol{x}) = \begin{cases} \boldsymbol{0} & \operatorname{dist}(\boldsymbol{x}, \Gamma) < \alpha_n/2, \\ \left(\frac{2\operatorname{dist}(\boldsymbol{x},\Gamma)}{\alpha_n} - 1\right) \boldsymbol{u}(\boldsymbol{x}) & \alpha_n/2 \le \operatorname{dist}(\boldsymbol{x}, \Gamma) < \alpha_n, \\ \boldsymbol{u}(\boldsymbol{x}) & \text{otherwise.} \end{cases}$$

   By the regularity of the distance function, it is straightforward to show that $\boldsymbol{u}_n \in H^1(\mathcal{B}; \mathbb{R}^2)$ and $\|\boldsymbol{u}_n - \boldsymbol{u}\|_{L^2(\mathcal{B};\mathbb{R}^2)} \to 0$ as $n \to \infty$. Moreover, since $|\boldsymbol{u}_n(\boldsymbol{x})| \le |\boldsymbol{u}(\boldsymbol{x})|$ for almost every $\boldsymbol{x} \in \mathcal{B}$, we have $\|\boldsymbol{u}_n\|_{L^\infty(\mathcal{B};\mathbb{R}^2)} \le \|\boldsymbol{u}\|_{L^\infty(\mathcal{B};\mathbb{R}^2)}$.
4. Next, let

$$\tilde{d}_n(t) = \begin{cases} \exp\left(\frac{\alpha_n - |t|}{2\varepsilon_n}\right) & |t| \ge \alpha_n \\ 1 & |t| < \alpha_n. \end{cases}$$

   We remark that the function $\tilde{d}_n(\operatorname{dist}(\boldsymbol{x}, \Gamma \setminus \mathcal{I}))$ is precisely that used in the recovery sequence by Chambolle. Here, we will use this function around the bulk (i.e., non-interfacial) cracks.
5. Around the interface cracks, we require another damage profile d. Let $\rho > 0$ and define

$$\overline{d}_n(t) = \begin{cases} 0 & |t| \ge \rho, \\ \dfrac{2g_i \sinh\left(\frac{|t|-\rho}{\varepsilon_n}\right)}{(g_b+g_i)\sinh\left(\frac{\alpha_n-\rho}{\varepsilon_n}\right) + (g_i-g_b)\sinh\left(\frac{\alpha_n-2m\varepsilon_n+\rho}{\varepsilon_n}\right)} & m\varepsilon_n \le |t| < \rho, \\ \dfrac{(g_b+g_i)\sinh\left(\frac{|t|-\rho}{\varepsilon_n}\right) + (g_i-g_b)\sinh\left(\frac{|t|-2m\varepsilon_n+\rho}{\varepsilon_n}\right)}{(g_b+g_i)\sinh\left(\frac{\alpha_n-\rho}{\varepsilon_n}\right) + (g_i-g_b)\sinh\left(\frac{\alpha_n-2m\varepsilon_n+\rho}{\varepsilon_n}\right)} & \alpha_n \le |t| < m\varepsilon_n, \\ 1 & |t| < \alpha_n. \end{cases}$$

   In the prior equation, we have assumed that $\alpha_n < m\varepsilon_n < \rho$. Because $\alpha_n = o(\varepsilon_n)$, we can always choose n sufficiently large so that this is the case. The function $\overline{d}_n(t)$ is computed by minimizing

$$\overline{\Pi}^f_{\varepsilon_n}[d] = \int_{-\rho}^{\rho} \frac{\overline{g}(t/\varepsilon_n)}{2} \left(\frac{d^2}{\varepsilon_n} + \varepsilon_n (d')^2\right) \mathrm{d}t$$

[7] This assumption is not terribly restrictive, see Proposition 8. For any $\eta > 0$, we can cover $\Gamma \cap I_i$ by $N_{i\eta}$ pairwise disjoint, simply connected, closed subsets $(A_j)_j$ so that

$$\mathcal{H}(\Gamma \cap I_i) \le \sum_{j=1}^{N_{i\eta}} \mathcal{H}^1(A_j) \le \mathcal{H}(\Gamma \cap I_i) + \eta.$$

We then proceed through the proof with this new set, and take $\eta \to 0+$ at the end.

over the set

$$\mathcal{V}_{\alpha_n\rho_n} := \left\{ d \in H^1((-\rho,\rho);\mathbb{R}) \ : \ d(t) = 1 \text{ for } t \in [-\alpha_n, \alpha_n],\, d(\pm\rho) = 0 \right\},$$

and extending the minimizer by 0 outside of the interval $[-\rho, \rho]$ (compare with the proof of Proposition 3). By construction,

$$\lim_{n\to\infty} \overline{\Pi}^f_{\varepsilon_n}[\overline{d}_n] = g_{\text{int}}.$$

6. Finally, we build d_n as the point-wise maximum of $\tilde{d}_n$ and $\overline{d}_n$:

$$d_n(\boldsymbol{x}) = \max\left\{ \tilde{d}_n(\text{dist}(\boldsymbol{x}, \Gamma \setminus \mathcal{N}_\rho(\mathcal{I}))), \overline{d}_n(\text{dist}(\boldsymbol{x}, \Gamma \cap \mathcal{I})) \right\},$$

where ρ is chosen to be the same as in the previous step. Just like the constituent functions, we remark that $0 \le d_n \le 1$. Moreover, $d_n(\boldsymbol{x}) = 1$ whenever $\boldsymbol{x} \in \mathcal{N}_{\alpha_n}(\Gamma)$. Importantly, d_n is Lipschitz continuous (as it is the point-wise maximum of the compositions of the Lipschitz functions $\tilde{d}_n$ and $\overline{d}_n$ with the respective distance functions). Hence, by Rademacher's Theorem, $d_n \in H^1(\mathcal{B};\mathbb{R})$. Going forward, we will abuse notation by writing $\tilde{d}_n(\text{dist}(\boldsymbol{x}, \Gamma \setminus \mathcal{N}_\rho(\mathcal{I})))$ as $\tilde{d}_n(\boldsymbol{x})$, with similar abuse of notation for $\overline{d}_n(\boldsymbol{x})$.

7. Now, we show that the sequences $(\boldsymbol{u}_n)_n$ and $(d_n)_n$ are indeed recovery sequences. As in the proof of Theorem 1(i), we let Π^e_ε and Π^f_ε be the two functionals in (7). Then, for the elastic energy

$$\Pi^e_{\varepsilon_n}[\boldsymbol{u}_n, d_n] = \Pi^e_{\varepsilon_n}[\boldsymbol{u}, d_n, \mathcal{B} \setminus \mathcal{N}_{\alpha_n}(\Gamma)] + \Pi^e_{\varepsilon_n}[\boldsymbol{u}_n, 1, \mathcal{B} \cap \mathcal{N}_{\alpha_n}(\Gamma)],$$

where we have used that $\boldsymbol{u}_n \equiv \boldsymbol{u}$ in $\mathcal{B} \setminus \mathcal{N}_{\alpha_n}(\Gamma)$ and the fact that $d_n \equiv 1$ in $\mathcal{N}_{\alpha_n}(\Gamma)$.

8. For the first term,

$$\Pi^e_{\varepsilon_n}[\boldsymbol{u}, d_n, \mathcal{B} \setminus \mathcal{N}_{\alpha_n}(\Gamma)] \le (1 + k_{\varepsilon_n}) \int_{\mathcal{B}\setminus\mathcal{N}_{\alpha_n}(\Gamma)} W(\boldsymbol{x}, \boldsymbol{\epsilon}(\boldsymbol{u}))\, \mathrm{d}\boldsymbol{x} \le (1 + k_{\varepsilon_n}) \int_{\mathcal{B}\setminus\Gamma} W(\boldsymbol{x}, \boldsymbol{\epsilon}(\boldsymbol{u}))\, \mathrm{d}\boldsymbol{x},$$

where the first inequality follows from the bounds on d_n (so that $(1-d_n)^2 \le 1$) and the second inequality follows from integrating a non-negative function over nested domains. Taking the limit as $n \to \infty$, we get

$$\limsup_{n\to\infty} \Pi^e_{\varepsilon_n}[\boldsymbol{u}, d_n, \mathcal{B} \setminus \mathcal{N}_{\alpha_n}(\Gamma)] \le \int_{\mathcal{B}\setminus\Gamma} W(\boldsymbol{x}, \boldsymbol{\epsilon}(\boldsymbol{u}))\, \mathrm{d}\boldsymbol{x}.$$

9. Meanwhile, for the second term, we first note that

$$\nabla \boldsymbol{u}_n(\boldsymbol{x}) = \left(\frac{2\text{dist}(\boldsymbol{x}, \Gamma)}{\alpha_n} - 1 \right) \nabla \boldsymbol{u}(\boldsymbol{x}) + \frac{2}{\alpha_n} \boldsymbol{u}(\boldsymbol{x}) \otimes \nabla \text{dist}(\boldsymbol{x}, \Gamma)$$

when $\boldsymbol{x} \in \mathcal{N}_{\alpha_n}(\Gamma) \setminus \mathcal{N}_{\alpha_n/2}(\Gamma)$. Because $W(\boldsymbol{x}, \boldsymbol{\epsilon}(\boldsymbol{u}))$ is a quadratic function of $\nabla \boldsymbol{u}$, we must have that

$$W(\boldsymbol{x}, \boldsymbol{\epsilon}(\boldsymbol{u}_n)) \le 2 \left(\frac{2\text{dist}(\boldsymbol{x}, \Gamma)}{\alpha_n} - 1 \right)^2 W(\boldsymbol{x}, \boldsymbol{\epsilon}(\boldsymbol{u})) + 2C_1 \frac{4}{\alpha_n^2} \|\boldsymbol{u}\|^2_{L^\infty(\mathcal{B};\mathbb{R}^2)},$$ [8]

[8] $W(\boldsymbol{x}, \boldsymbol{\epsilon}(\boldsymbol{u}))$ may be shown to have the form $\nabla \boldsymbol{u} : \tilde{\mathbb{C}}(\boldsymbol{x}) : \nabla \boldsymbol{u}$, where the symmetric, fourth-order tensor $\tilde{\mathbb{C}}(\boldsymbol{x})$ is

where the constant C_1 depends on the elastic properties of the bulk material. In computing the previous constant, we used that $|\nabla \mathrm{dist}(\boldsymbol{x}, \Gamma)| = 1$ almost everywhere in $\mathcal{B}$, so that $|\boldsymbol{u} \otimes \nabla \mathrm{dist}(\boldsymbol{x}, \Gamma)| \leq \|\boldsymbol{u}\|_{L^\infty(\mathcal{B};\mathbb{R}^2)}$. Hence, also noting that the prefactor $2\mathrm{dist}(\boldsymbol{x}, \Gamma)/\alpha_n - 1 \leq 1$,

$$\begin{aligned}\Pi^e_{\varepsilon_n}[\boldsymbol{u}_n, 1, \mathcal{B} \cap \mathcal{N}_{\alpha_n}(\Gamma)] &\leq 2k_{\varepsilon_n} \int_{\mathcal{B}\cap\mathcal{N}_{\alpha_n}(\Gamma)\setminus\mathcal{N}_{\alpha_n/2}(\Gamma)} W(\boldsymbol{x}, \boldsymbol{\epsilon}(\boldsymbol{u}))\,\mathrm{d}\boldsymbol{x} \\ &\qquad + 8C_1 \frac{k_{\varepsilon_n}\|\boldsymbol{u}\|^2_{L^\infty(\mathcal{B};\mathbb{R}^2)}}{\alpha_n^2}\mathcal{L}^2(\mathcal{B} \cap \mathcal{N}_{\alpha_n}(\Gamma) \setminus \mathcal{N}_{\alpha_n/2}(\Gamma)), \\ &\leq 2k_{\varepsilon_n} \int_{\mathcal{B}\cap\mathcal{N}_{\alpha_n}(\Gamma)} W(\boldsymbol{x}, \boldsymbol{\epsilon}(\boldsymbol{u}))\,\mathrm{d}\boldsymbol{x} + 8C_1 \frac{k_{\varepsilon_n}\|\boldsymbol{u}\|^2_{L^\infty(\mathcal{B};\mathbb{R}^2)}}{\alpha_n^2}\mathcal{L}^2(\mathcal{N}_{\alpha_n}(\Gamma)).\end{aligned}$$

10. To bound $\mathcal{L}^2(\mathcal{N}_{\alpha_n}(\Gamma))$, we appeal to the Minkowski content:

$$\lim_{\alpha\to 0+} \frac{\mathcal{L}^2(\mathcal{N}_\alpha(\Gamma))}{2\alpha}$$

which coincides with $\mathcal{H}^1(\Gamma)$ for closed, rectifiable subsets of $\mathbb{R}^2$ [64, Theorem 3.2.39]. From the fact that this is a convergent, non-negative sequence when evaluated on $(\alpha_n)_n$, we observe that there must exist a constant $C_2 > 0$ such that

$$\mathcal{L}^2(\mathcal{N}_{\alpha_n}(\Gamma)) \leq 2\alpha_n C_2$$

holds for all n. Hence,

$$\Pi^e_{\varepsilon_n}[\boldsymbol{u}_n, 1, \mathcal{B} \cap \mathcal{N}_{\alpha_n}(\Gamma)] \leq 2k_{\varepsilon_n} \int_{\mathcal{B}\cap\mathcal{N}_{\alpha_n}(\Gamma)} W(\boldsymbol{x}, \boldsymbol{\epsilon}(\boldsymbol{u}))\,\mathrm{d}\boldsymbol{x} + 16C_1C_2 \frac{k_{\varepsilon_n}\|\boldsymbol{u}\|^2_{L^\infty(\mathcal{B};\mathbb{R}^2)}}{\alpha_n}.$$

The first term must shrink to zero, because $\mathcal{B}\cap\mathcal{N}_{\alpha_n}(\Gamma) \subseteq \mathcal{B}$, $0 \leq \int_{\mathcal{B}} W(\boldsymbol{x}, \boldsymbol{\epsilon}(\boldsymbol{u}))\,\mathrm{d}\boldsymbol{x} < \infty$, and $k_{\varepsilon_n} \to 0$ as $n \to \infty$. The second term must also shrink to zero since we have selected $(\alpha_n)_n$ so that $k_{\varepsilon_n} = o(\alpha_n)$. Hence,

$$\limsup_{n\to\infty} \Pi^e_{\varepsilon_n}[\boldsymbol{u}_n, 1, \mathcal{B} \cap \mathcal{N}_{\alpha_n}(\Gamma)] = 0.$$

11. Next, we turn to the surface energy. Define the set

$$A_n = \left\{\boldsymbol{x} \in \mathcal{B} \ : \ d_n(\boldsymbol{x}) = \overline{d}_n(\boldsymbol{x})\right\}.$$

Then

$$\Pi^f_{\varepsilon_n}[\boldsymbol{u}_n, d_n, \mathcal{B}] = \Pi^f_{\varepsilon_n}[\boldsymbol{u}_n, \tilde{d}_n, \mathcal{B} \setminus A_n] + \Pi^f_{\varepsilon_n}[\boldsymbol{u}_n, \overline{d}_n, A_n].$$

---

bounded and has nonnegative components. For such quadratic forms, if $\nabla\boldsymbol{u} = \boldsymbol{U}_1 + \boldsymbol{U}_2$, then

$$(\boldsymbol{U}_1 + \boldsymbol{U}_2) : \tilde{\mathbb{C}}(\boldsymbol{x}) : (\boldsymbol{U}_1 + \boldsymbol{U}_2) \leq 2\boldsymbol{U}_1 : \tilde{\mathbb{C}}(\boldsymbol{x}) : \boldsymbol{U}_1 + 2\boldsymbol{U}_2 : \tilde{\mathbb{C}}(\boldsymbol{x}) : \boldsymbol{U}_2.$$

Noting that $\boldsymbol{U}_1 = f(\boldsymbol{x})\nabla\boldsymbol{u}$ gives $2\boldsymbol{U}_1 : \tilde{\mathbb{C}}(\boldsymbol{x}) : \boldsymbol{U}_1 = 2f(\boldsymbol{x})^2 W(\boldsymbol{x}, \boldsymbol{\epsilon}(\boldsymbol{u}))$. Meanwhile, by the boundedness of $\tilde{\mathbb{C}}(\boldsymbol{x})$, there exists a constant $C_1 > 0$ such that $\boldsymbol{U}_2 : \tilde{\mathbb{C}}(\boldsymbol{x}) : \boldsymbol{U}_2 \leq C_1|\boldsymbol{U}_2|^2$.

12. For integration on $\mathcal{B} \setminus A_n$, we use the fact that $g_\varepsilon(\boldsymbol{x}) \leq g_b$ for any $\boldsymbol{x} \in \mathcal{B}$, while $\mathcal{B} \setminus A_n \subseteq \mathcal{B}$, and so

$$\Pi^f_{\varepsilon_n}[\boldsymbol{u}_n, \tilde{d}_n, \mathcal{B} \setminus A_n] \leq \int_{\mathcal{B}\setminus A_n} \frac{g_b}{2}\left(\frac{\tilde{d}_n^2}{\varepsilon_n} + \varepsilon_n|\nabla \tilde{d}_n|^2\right) \mathrm{d}\boldsymbol{x} \leq \int_{\mathcal{B}} \frac{g_b}{2}\left(\frac{\tilde{d}_n^2}{\varepsilon_n} + \varepsilon_n|\nabla \tilde{d}_n|^2\right) \mathrm{d}\boldsymbol{x}.$$

The set $\Gamma \setminus \mathcal{N}_\rho(\mathcal{I})$ is closed and rectifiable. Hence, the integral on the right is simply the one that results from Chambolle's construction for the crack set $\Gamma \setminus \mathcal{N}_\rho(\mathcal{I})$. Repeating his steps, we get

$$\limsup_{n\to\infty} \Pi^f_{\varepsilon_n}[\boldsymbol{u}_n, \tilde{d}_n, \mathcal{B} \setminus A_n] \leq \limsup_{n\to\infty} \int_{\mathcal{B}} \frac{g_b}{2}\left(\frac{\tilde{d}_n^2}{\varepsilon_n} + \varepsilon_n|\nabla \tilde{d}_n|^2\right) \mathrm{d}\boldsymbol{x} \leq g_b \mathcal{H}^1(\Gamma \setminus \mathcal{N}_\rho(\mathcal{I})).$$

13. For integration on A_n, we consider the subsets $(A_{nj})_j$, where

$$A_{nj} = \left\{\boldsymbol{x} \in A_n \ : \ d_n(\boldsymbol{x}) = \overline{d}_{nj}(\boldsymbol{x})\right\},$$

where we use the shorthand $\overline{d}_{nj}(\boldsymbol{x}) := \overline{d}_n(\mathrm{dist}(\boldsymbol{x}, \Gamma_j))$. We recall that the simply connected pieces $(\Gamma_j)_j$ which compose $\Gamma \cap \mathcal{I}$ were defined in Step 1. Then, because these subsets might overlap (in particular, if $\overline{d}_{nj}(\boldsymbol{x}) = \overline{d}_{nk}(\boldsymbol{x}) = 1$ for some $j \neq k$),

$$\Pi^f_{\varepsilon_n}[\boldsymbol{u}_n, \overline{d}_n, A_n] \leq \sum_{j=1}^{J} \Pi^f_{\varepsilon_n}[\boldsymbol{u}_n, \overline{d}_{nj}, A_{nj}]$$

Additionally, because $\overline{d}_{nj}(\boldsymbol{x}) = 0$ for $\boldsymbol{x} \notin \mathcal{N}_\rho(\Gamma_j)$, we have $A_{nj} \subseteq \mathcal{N}_\rho(\Gamma_j)$, and so for each j

$$\Pi^f_{\varepsilon_n}[\boldsymbol{u}_n, \overline{d}_{nj}, A_{nj}] \leq \Pi^f_{\varepsilon_n}[\boldsymbol{u}_n, \overline{d}_{nj}, \mathcal{N}_\rho(\Gamma_j)] = \int_{\mathcal{N}_\rho(\Gamma_j)} \frac{g_{\varepsilon_n}(\boldsymbol{x})}{2}\left(\frac{\overline{d}_{nj}^2}{\varepsilon_n} + \varepsilon_n|\nabla \overline{d}_{nj}|^2\right) \mathrm{d}\boldsymbol{x}.$$

Finally, because $\mathrm{dist}(\boldsymbol{x}, \Gamma_j) \geq \mathrm{dist}(\boldsymbol{x}, \mathcal{I})$, we have $g_\varepsilon(\boldsymbol{x}) = \overline{g}(\mathrm{dist}(\boldsymbol{x}, \mathcal{I})/\varepsilon) \leq \overline{g}(\mathrm{dist}(\boldsymbol{x}, \Gamma_j)/\varepsilon)$, and so

$$\int_{\mathcal{N}_\rho(\Gamma_j)} \frac{g_{\varepsilon_n}(\boldsymbol{x})}{2}\left(\frac{\overline{d}_{nj}^2}{\varepsilon_n} + \varepsilon_n|\nabla \overline{d}_{nj}|^2\right) \mathrm{d}\boldsymbol{x} \leq \int_{\mathcal{N}_\rho(\Gamma_j)} \frac{\overline{g}(\mathrm{dist}(\boldsymbol{x}, \Gamma_j)/\varepsilon_n)}{2}\left(\frac{\overline{d}_{nj}^2}{\varepsilon_n} + \varepsilon_n|\nabla \overline{d}_{nj}|^2\right) \mathrm{d}\boldsymbol{x}.$$

14. Let $z = \mathrm{dist}(\boldsymbol{x}, \Gamma_j)$. Then $\overline{d}_{nj}(\boldsymbol{x}) = \overline{d}_n(z)$. Meanwhile, $\nabla \overline{d}_{nj}(\boldsymbol{x}) = \overline{d}_n'(z)\nabla \mathrm{dist}(\boldsymbol{x}, \Gamma_j)$, where we recall that $|\nabla \mathrm{dist}(\boldsymbol{x}, \Gamma_j)| = 1$ almost everywhere, and so $|\nabla \overline{d}_{nj}(\boldsymbol{x})|^2 = (\overline{d}_n'(z))^2$ almost everywhere. Hence, the above integrand depends only on z, the distance to Γ_j. Via integration over level sets of the distance function [56, Theorem 3.11], this may be written as

$$\int_{\mathcal{N}_\rho(\Gamma_j)} \frac{\overline{g}(\mathrm{dist}(\boldsymbol{x}, \Gamma_j)/\varepsilon_n)}{2}\left(\frac{\overline{d}_{nj}^2}{\varepsilon_n} + \varepsilon_n|\nabla \overline{d}_{nj}|^2\right) \mathrm{d}\boldsymbol{x} = \int_0^\rho \frac{\overline{g}(z/\varepsilon_n)}{2}\left(\frac{\overline{d}_n(z)^2}{\varepsilon_n} + \varepsilon_n(\overline{d}_n'(z))^2\right) \mathcal{H}^1(\partial \mathcal{N}_z(\Gamma_j))\, \mathrm{d}z.$$

Using Proposition 4, we may bound

$$\begin{aligned}
&\int_0^\rho \frac{\overline{g}(z/\varepsilon_n)}{2}\left(\frac{\overline{d}_n(z)^2}{\varepsilon_n} + \varepsilon_n(\overline{d}_n'(z))^2\right) \mathcal{H}^1(\partial \mathcal{N}_z(\Gamma_j))\, \mathrm{d}z \\
&\qquad \leq \left(4\pi\rho + 2\left(1 + \frac{\rho}{R_{\min}}\right)\mathcal{H}^1(\Gamma_j)\right) \int_0^\rho \frac{\overline{g}(z/\varepsilon_n)}{2}\left(\frac{\overline{d}_n(z)^2}{\varepsilon_n} + \varepsilon_n(\overline{d}_n'(z))^2\right) \mathrm{d}z.
\end{aligned}$$

The integral on the right is precisely that which is minimized by our choice of $\overline{d}_n$. Hence,

$$\lim_{n\to\infty} \int_0^\rho \frac{\overline{g}(z/\varepsilon_n)}{2} \left(\frac{\overline{d}_n(z)^2}{\varepsilon_n} + \varepsilon_n (\overline{d}_n'(z))^2 \right) \mathrm{d}z = \frac{g_{\mathrm{int}}}{2}.$$

As a shorthand, let $g_n/2$ be the above integral for integer n, so that $\lim_{n\to\infty} g_n = g_{\mathrm{int}}$.

15. Putting together the bounds for the integrals over each set A_{nj}, we conclude that

$$\begin{aligned}
\limsup_{n\to\infty} \Pi^f_{\varepsilon_n}[\boldsymbol{u}_n, \overline{d}_n, A_n] &\le \lim_{n\to\infty} \sum_{j=1}^J \frac{g_n}{2} \left(4\pi\rho + 2\left(1 + \frac{\rho}{R_{\min}}\right) \mathcal{H}^1(\Gamma_j) \right) \\
&= \lim_{n\to\infty} g_n \left(2\pi J\rho + \left(1 + \frac{\rho}{R_{\min}}\right) \sum_{j=1}^J \mathcal{H}^1(\Gamma_j) \right) \\
&= g_{\mathrm{int}} \left(2\pi J\rho + \left(1 + \frac{\rho}{R_{\min}}\right) \mathcal{H}^1(\Gamma \cap \mathcal{I}) \right).
\end{aligned}$$

16. Finally, putting together Steps 8, 10, 12, and 15 yields

$$\limsup_{n\to\infty} \Pi_{\varepsilon_n}[\boldsymbol{u}_n, d_n] \le \int_{\mathcal{B}\setminus\Gamma} W(\boldsymbol{x}, \boldsymbol{\epsilon}(\boldsymbol{u}))\, \mathrm{d}\boldsymbol{x} + g_b \mathcal{H}^1(\Gamma \setminus \mathcal{N}_\rho(\mathcal{I})) + g_{\mathrm{int}} \left(2\pi J\rho + \left(1 + \frac{\rho}{R_{\min}}\right) \mathcal{H}^1(\Gamma \cap \mathcal{I}) \right).$$

Since $\rho > 0$ is arbitrary, we may take it to zero to yield the conclusion. In particular, for the second term, we note that

$$\bigcup_{\rho>0} \Gamma \setminus \mathcal{N}_\rho(\mathcal{I}) = \Gamma \setminus \mathcal{I}$$

and so by continuity of measures on nested sets

$$\lim_{\rho\to 0+} \mathcal{H}^1(\Gamma \setminus \mathcal{N}_\rho(\mathcal{I})) = \mathcal{H}^1(\Gamma \setminus \mathcal{I}).$$

□

5. Numerical implementation

The model and analysis of the previous sections does not address crack evolution in response to time-varying external loads. Rather, the variational principle itself is general, providing a framework to study problems with interfaces. In the following sections, we apply our approach to problems featuring crack growth in order to study toughening mechanisms in SBs. While a crack growth model is not part of our theoretical framework, for concreteness we summarize the approach used in the computations. For further details of the model and method, we refer the reader to [65].

5.1. Evolution via local stationary points

We suppose that the applied displacements vary with time t (i.e., $\hat{\boldsymbol{u}} = \hat{\boldsymbol{u}}(t)$). Then, at time t, we seek $(\boldsymbol{u}(t), d(t))$ to be stationary points of the functional Π_ε. That is, recalling the admissible function spaces

$$\mathcal{U}_u(t) = \left\{\boldsymbol{v} \in H^1(\mathcal{B};\mathbb{R}^2) \ : \ \boldsymbol{v}(\boldsymbol{x}) = \hat{\boldsymbol{u}}(t,\boldsymbol{x}) \text{ for } \boldsymbol{x} \in \partial\mathcal{B}_u\right\} \tag{17a}$$

$$\mathcal{U}_d = H^1(\mathcal{B};\mathbb{R}), \tag{17b}$$

and defining test spaces

$$\mathcal{V}_u = \left\{\boldsymbol{v} \in H^1(\mathcal{B};\mathbb{R}^2) \ : \ \boldsymbol{v} \equiv \boldsymbol{0} \text{ on } \partial\mathcal{B}_u\right\} \tag{18a}$$

$$\mathcal{V}_d = \mathcal{U}_d, \tag{18b}$$

at time t we seek $(\boldsymbol{u}(t), d(t)) \in \mathcal{U}_u(t) \times \mathcal{U}_d$ which satisfy

$$\begin{aligned} 0 = &\int_{\mathcal{B}} \left((1-d)^2 + k_\varepsilon\right) \frac{\partial W(\boldsymbol{x}, \boldsymbol{\epsilon}(\boldsymbol{u}))}{\partial \boldsymbol{\epsilon}} : \boldsymbol{\epsilon}(\boldsymbol{v}) \, \mathrm{d}\boldsymbol{x} \\ &+ \int_{\mathcal{B}} \left\{ \left[\frac{g_\varepsilon(\boldsymbol{x}) d}{\varepsilon} - 2(1-d) W(\boldsymbol{x}, \boldsymbol{\epsilon}(\boldsymbol{u})) \right] \phi + g_\varepsilon(\boldsymbol{x}) \varepsilon \nabla d \cdot \nabla \phi \right\} \mathrm{d}\boldsymbol{x} \end{aligned} \tag{19}$$

for any $(\boldsymbol{v}, \phi) \in \mathcal{V}_u \times \mathcal{V}_d$.

We remark that stationarity of Π_ε is a very different condition from global minimality [46]. Moreover, a consequence of Γ-convergence is that global minimizers of Π_ε will converge to those of Π as $\varepsilon \to 0$ [66]; in general, this result does not hold for local minimizers or stationary points.

5.2. Discretization and solution procedure

We partition the time interval of interest $[0, T]$ into N steps: $0 = t_0 < t_1 < \ldots < t_N = T$. For simplicity, we assume a fixed time step $\Delta t = t_{n+1} - t_n$ for any n. We seek functions $(\boldsymbol{u}_n, d_n)$ which approximate $(\boldsymbol{u}(t_n), d(t_n))$. We spatially discretize the stationarity equation using the Finite Element Method (e.g., [67]) with bilinear quadrilateral (Q1) finite elements. In other words, we partition $\mathcal{B}$ into a mesh $\mathcal{T}^h$ of non-overlapping quadrilaterals with maximum diameter h; the admissible and test functions are those that are continuous and whose restriction to any quadrilateral $E \in \mathcal{T}^h$ are bilinear. We let $\mathcal{U}_u^h(t_n)$ denote the admissible finite element function space for $\boldsymbol{u}$ at t_n, and we use similar notation for the other function spaces. We construct our mesh $\mathcal{T}^h$ to conform to the boundaries of the widened interface (i.e., the $m\varepsilon$-neighborhood of $\mathcal{I}$). This ensures that the restriction of $g_\varepsilon(\boldsymbol{x})$ to each quadrilateral is a constant (either g_b or g_i).

We define $(\boldsymbol{u}_n, d_n) \in \mathcal{U}_u^h(t_n) \times \mathcal{U}_d^h$ to be the functions satisfying (19) for any $(\boldsymbol{v}, \phi) \in \mathcal{V}_u^h \times \mathcal{V}_d^h$. Choosing a set of basis functions for the finite element spaces results in a finite-dimensional system

of nonlinear equations. We solve these equations monolithically (simultaneously for both $\boldsymbol{u}_n$ and d_n) using Newton-Raphson iteration in Abaqus [68]. Instead of a monolithic scheme, we could have staggered the solution of $\boldsymbol{u}_n$ and d_n (the so-called "Alternate Minimization" approach [45]) to take advantage of the biconvexity of Π_ε.

5.3. Modifications to the equations

Motivated by physical modeling considerations, we make three modifications to (19) before use in the examples. First, the previous equations do not distinguish energetically between open cracks and interpenetrated cracks, a symmetry also present in classical fracture mechanics without contact. Hence, cracks may nucleate and grow in regions under compression. To combat this, several approaches have been proposed in the literature (cf. the review [69]). These approaches split the strain energy density W into positive and negative parts (corresponding to tensile and compressive strains and/or stresses), and only the positive part is degraded by the damage. That is, we replace

$$\left((1-d)^2+k_\varepsilon\right) W(\boldsymbol{x},\boldsymbol{\epsilon}) \to \left((1-d)^2+k_\varepsilon\right) W^+(\boldsymbol{x},\boldsymbol{\epsilon}) + W^-(\boldsymbol{x},\boldsymbol{\epsilon}).$$

In this work, we adopt the spectral split of Miehe et al. [49]. For the isotropic, linear elastic constitutive response, the forms of $W^\pm$ are

$$W^\pm(\boldsymbol{x},\boldsymbol{\epsilon}) = \frac{1}{2}\lambda(\boldsymbol{x})\langle \epsilon_1+\epsilon_2\rangle_\pm^2 + \mu(\boldsymbol{x})\left(\langle\epsilon_1\rangle_\pm^2 + \langle\epsilon_2\rangle_\pm^2\right)$$

where ϵ_1 and ϵ_2 are the principal strains of the tensor $\boldsymbol{\epsilon}$, and $\langle\epsilon\rangle_+ = \max\{0,\epsilon\}$ while $\langle\epsilon\rangle_- = \min\{0,\epsilon\}$.

Second, we impose irreversibility on the crack evolution. We remark that this condition was part of the original VFT [44] and RVFT [45], though it may not be applicable for all engineering situations (i.e., crack healing). In RVFT, this condition is $d(t_1,\boldsymbol{x}) \geq d(t_2,\boldsymbol{x})$ for any $t_1 \geq t_2$ and $\boldsymbol{x}\in\mathcal{B}$. Numerically, this condition can be enforced via inequality constraint $(d_{n+1}(\boldsymbol{x}) \geq d_n(\boldsymbol{x})$ for $\boldsymbol{x}\in\mathcal{B})$ [45]. We instead adopt the approach of [70], which replaces the strain energy density W^+ in the damage-field portion of (19) with a history variable

$$\mathsf{H}(t,\boldsymbol{x}) = \max_{s\in[0,t)} W^+(\boldsymbol{x},\boldsymbol{\epsilon}(\boldsymbol{u}(s))).$$

In the time-discrete case, this variable is

$$\mathsf{H}(t_n,\boldsymbol{x}) = \max_{0\leq m<n} W^+(\boldsymbol{x},\boldsymbol{\epsilon}(\boldsymbol{u}_m))$$

In the formulation in §3, we have neglected inertial effects, i.e. we have assumed that the deformation is static. When we introduce time-varying external loading, we maintain the assumption of negligible inertia, which is referred to as quasi-static behavior. Hence, time t only acts to parameterize the external loads and does not need to correspond to physical time. Rather t can be replaced by any increasing load parameter. As a consequence of neglecting inertia, numerical instabilities can arise when the damage field evolves rapidly from one time step to another, for example in the case of catastrophic crack propagation, where the crack may grow large distances in very small intervals of time. In particular, conventional methods to solve (19) such as Newton iteration can fail to find solutions because $(\boldsymbol{u}_{n+1}, d_{n+1})$ is "far" from $(\boldsymbol{u}_n, d_n)$. To mitigate these numerical

instabilities, as the final modification, when seeking d_{n+1} we add to the damage field equation (19) a viscous damping term of the form $\frac{\eta}{2\Delta t}\left(\frac{d-d_n}{\Delta t}\right)\left|\frac{d-d_n}{\Delta t}\right|\phi$, where $\eta > 0$ [70]. This term may be derived by adding the cubic penalty $\frac{\eta}{6}|\dot{d}|^3$ to the modified energy (7), introducing the finite time difference $\dot{d}(t_{n+1}) \approx \frac{d-d_n}{\Delta t}$, and taking the variation with respect to d.

In summary, the modified version of (19) incorporating the above three changes is as follows. At time t_{n+1}, we seek $(\boldsymbol{u}, d) \in \mathcal{U}_u^h(t_{n+1}) \times \mathcal{U}_d^h$ which satisfy

$$\begin{aligned} 0 = &\int_{\mathcal{B}} \left[\left((1-d)^2 + k_\varepsilon\right) \frac{\partial W^+(\boldsymbol{x}, \boldsymbol{\epsilon}(\boldsymbol{u}))}{\partial \boldsymbol{\epsilon}} + \frac{\partial W^-(\boldsymbol{x}, \boldsymbol{\epsilon}(\boldsymbol{u}))}{\partial \boldsymbol{\epsilon}} \right] : \boldsymbol{\epsilon}(\boldsymbol{v}) \, \mathrm{d}\boldsymbol{x} \\ &+ \int_{\mathcal{B}} \left\{ \left[\frac{g_\varepsilon(\boldsymbol{x}) d}{\varepsilon} - 2(1-d)\mathsf{H}(t_{n+1}, \boldsymbol{x}) + \frac{\eta}{2\Delta t}\left(\frac{d-d_n}{\Delta t}\right)\left|\frac{d-d_n}{\Delta t}\right| \right] \phi + g_\varepsilon(\boldsymbol{x}) \varepsilon \nabla d \cdot \nabla \phi \right\} \mathrm{d}\boldsymbol{x} \end{aligned} \tag{20}$$

for any $(\boldsymbol{v}, \phi) \in \mathcal{V}_u^h \times \mathcal{V}_d^h$. We denote the solution to (20) as $(\boldsymbol{u}_{n+1}, d_{n+1})$.

6. Numerical verification

In this section, we assess the implementation of the modified RVFT for interfaces (RVFTI) in §5 and, in particular, how it relates to the theory of §3.3. The verification provided in this section is two-fold:

(1) In standard RVFT, it has been shown that crack initiation occurs when the energy release rate is equal to the constant fracture toughness g [71]. We show for RVFTI that crack initiation occurs when the energy release rate is equal to g_{int} in (8).
(2) We study the problem of the kinking of a crack at the bi-material interface subjected to far-field loading. We compare the computationally-observed kink angles against those predicted by the semi-analytical solutions of He and Hutchinson [25]. We also study the ability of RVFTI to predict crack trapping by the interface, which we also compare with [25].

6.1. Crack initiation fracture toughness for the interface model

We first study a single edge notch (SEN) specimen under plane strain conditions with Young's modulus E and Poisson's ratio ν. The bulk fracture toughness is g_b, and we set the fracture toughness in the widened interface as g_i. The specimen has width b, while the initial notch has length a. We take the interface thickness to be $2m\varepsilon$. The specimen is depicted in Figure 3(a).

We prescribe along the boundary of the specimen the asymptotic mode I displacement field with prescribed stress intensity factor K_I^∞ (see [72])

$$u_x(\boldsymbol{x}) = K_I^\infty u_x^I(\boldsymbol{x}) = \frac{K_I^\infty}{2\mu}\sqrt{\frac{r}{2\pi}}\cos\left(\frac{\theta}{2}\right)(3-4\nu-\cos(\theta)) \tag{21a}$$

$$u_y(\boldsymbol{x}) = K_I^\infty u_y^I(\boldsymbol{x}) = \frac{K_I^\infty}{2\mu}\sqrt{\frac{r}{2\pi}}\sin\left(\frac{\theta}{2}\right)(3-4\nu-\cos(\theta)), \tag{21b}$$

where r and θ are the usual polar coordinates associated with the point $\boldsymbol{x} \in \mathbb{R}^2$. Under plane strain conditions, the energy release rate $\mathcal{G}$ is related to K_I^∞ via $\mathcal{G} = (1-\nu^2)(K_I^\infty)^2/E$.

From Griffith's criterion [39], crack growth occurs when the energy release rate at the crack tip is equal to the fracture toughness of the material, i.e. $\mathcal{G} = g_{\text{int}}$. Hence, from a simulation we may estimate the interface fracture toughness, denoted by g_{int}^h, using the relationship

$$g_{\text{int}}^h = \frac{1-\nu^2}{E}(K_{I,\text{cr}}^\infty)^2, \tag{22}$$

where $K_{I,\text{cr}}^\infty$ is the critical value of the prescribed mode I stress intensity factor at which the crack initiates.

In our computations, $b = 100$ mm, $a = b/4$, and we took the height of the SEN specimen to be $100b$. The material has shear modulus $\mu = 22 \times 10^3$ MPa and Poisson's ratio $\nu = 1/4$. For the damage field, we set $\varepsilon = b/500$, $k_\varepsilon = 0$, and we vary $m \in \{0.1, 0.2, 0.3, 0.4, 0.5\}$, $g_i \in \{1, 5\}$ N/mm, and $g_b/g_i \in \{2, 5, 20\}$.

For the finite-width notch, we initialize the damage field by setting $d = 1$ in the rectangle $-a \le x \le 0$ and $-h \le y \le h$, where $h = b/1000$ is the half-width of the notch. We estimate $K_{I,\text{cr}}^\infty$ for the above parameter combinations by slowly incrementing the parameter K_I^∞ from zero until the first node ahead of the notch (at $x = 0$) attains a damage value of $d = 0.99$. These values of $K_{I,\text{cr}}^\infty$ are then used to estimate g_{int}^h in (22).

In Fig. 3(b), we compare the analytical expression for the ratio g_{int}/g_b of (8) against the numerically computed value g^h_{int}/g_b. The thick dashed line with unit slope corresponds to one-to-one equivalence. We observe good agreement between g^h_{int} and g_{int}, and the error between the two is within $0.065 g_b$. Additionally the precise values of g_i and g_b had minimal impact on g^h_{int}/g_b, which is consistent with (8). Hence, we conclude that the numerically obtained values for interface fracture toughness are largely consistent with their analytical counterparts.

For the cases where $m = 0.2$ and $g_i = 1$ N/mm, we also ran simulations with variable ε. We show the computed values of g^h_{int}/g_b versus ε in Fig. 3(c). All simulations results in this subfigure were computed on a single mesh with $h \approx 0.01$ mm. We observe that as ε decreases, the value of g^h_{int} gets closer to the exact value g_{int}. Because of the differences between RVFTI in §5 and the theory in §4, and several other differences, it is not guaranteed that the numerical simulations should converge under ε refinement. For these reasons, we find the results in Fig. 3(c) especially remarkable.

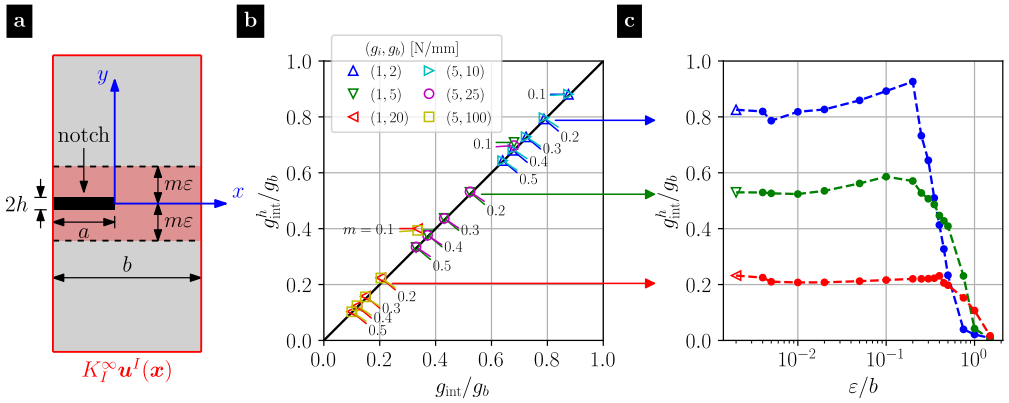

Figure 3: (a) Schematic of SEN specimen subjected to the asymptotic mode I displacement field along the boundary. The specimen has width b, the initial notch has length $a = b/4$, and the interface thickness is $2m\varepsilon$. (b) Comparison between the theoretical interface fracture toughness, g_{int}/g_b, and that computed from the simulations, g^h_{int}/g_b, for $m \in \{0.1, 0.2, 0.3, 0.4, 0.5\}$, $\varepsilon = b/500$, $g_i \in \{1,5\}$ N/mm and $g_b/g_i \in \{2, 5, 20\}$. (c) Variation in the computed value of g^h_{int}/g_b versus ε for the cases where $m = 0.2$ and $g_i = 1$ N/mm.

6.2. Kinking of a crack at a bi-material interface

We benchmark RVFTI by comparing against kink angle predictions made by He and Hutchinson [25] for a semi-infinite crack along the interface between two materials and subjected to far-field loading. The geometry of the crack is illustrated in Figure 4, where a semi-infinite crack is present along the interface of material 1 and 2. The shear modulus and Poisson's ratio of materials 1 and 2 are (μ_1, ν_1) and (μ_2, ν_2), respectively.

He and Hutchinson assume that a new crack grows from the tip of the semi-infinite crack along a fixed direction. In this section, the original semi-infinite crack is termed the interface crack and the new crack segment is termed the kinked crack. The angle that the kinked crack makes with respect to the interface (measured clockwise from the x-axis) is called the kink angle ω and its length is denoted as a.

The domain is loaded at infinity so that the interface crack (without the kink) is under a state of mode I and mode II stress intensity; these remote stress intensity factors are denoted K_1 and K_2, respectively. Following [25], the mode mixity is described using a non-dimensional parameter called the phase angle $\gamma = \arctan(K_2/K_1)$. The parameter γ indicates whether the loading is mode I or mode II dominant; $\gamma = 0$ under pure mode I loading, while $\gamma = \pi/2$ for pure mode II loading, and $\gamma < \pi/4$ (resp. $\gamma > \pi/4$) for mode I (resp. mode II) dominant loading. Expressions for the asymptotic mode I and mode II displacement fields in the vicinity of the interface crack in terms of K_1 and K_2 will be described later.

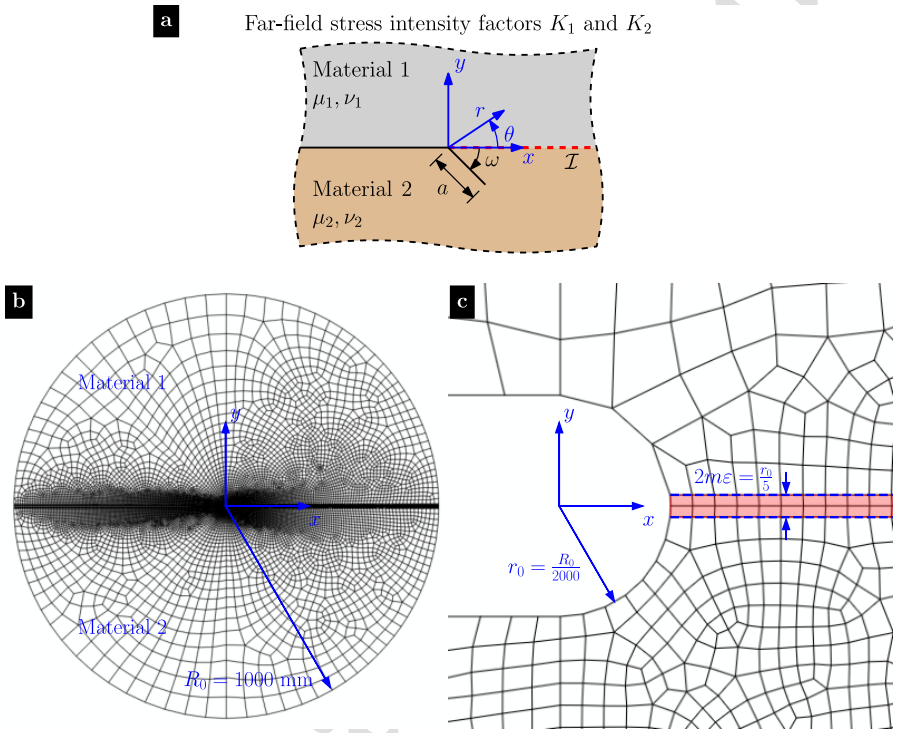

Figure 4: Semi-infinite crack along a bi-material interface. (a) Schematic of the geometry, showing a crack along the interface between materials 1 (gray) and 2 (brown), which has kinked by an angle ω (defined clockwise) into material 2. The far-field loading is characterized by stress intensity factors K_1 and K_2 with stress intensity phase angle $\gamma = \arctan(K_2/K_1)$. The kink length a is assumed to be very small compared to any other relevant problem dimensions. (b) Quadrilateral mesh used in the finite element computations. The computational domain has radius $R_0 = 1000$ mm and finite-width notch. (c) Closeup of the notch tip, showing the notch radius $r_0 = R_0/1000$, and the wide interface with width $2m\varepsilon = r_0/5$.

For the bi-material problem studied in [25], it had been shown that the kink angle depends on two non-dimensional material parameters called the Dundurs mismatch parameters α and β [73],

which depend as follows on the four material moduli:

$$\alpha := \frac{\mu_1 (1-\nu_2) - \mu_2 (1-\nu_1)}{\mu_1 (1-\nu_2) + \mu_2 (1-\nu_1)}, \tag{23a}$$

$$\beta := \frac{1}{2}\left(\frac{\mu_1 (1-2\nu_2) - \mu_2 (1-2\nu_1)}{\mu_1 (1-\nu_2) + \mu_2 (1-\nu_1)}\right). \tag{23b}$$

The parameter α can be interpreted as a relative measure of stiffness; $\alpha = 1$ when material 1 is rigid and $\alpha = -1$ when material 2 is rigid. Physical interpretation for β is unclear. In this work we choose $\beta = 0$ because for the case of $\beta \neq 0$ it has been shown that the interface crack faces interpenetrate [22, 74, 75], which is unphysical.

The mode I and II stress intensity factors of the kinked crack are denoted by K_I and K_{II}, respectively. They may be related to the remote stress intensity factors, K_1 and K_2, for the case of $\beta = 0$, as given in [25],

$$K_I + iK_{II} = \left(c(\omega,\alpha) + \bar{d}(\omega,\alpha)\right) K_1 + i\left(c(\omega,\alpha) - \bar{d}(\omega,\alpha)\right) K_2, \tag{24}$$

where $i = \sqrt{-1}$. The functions c and d are complex-valued in terms of ω and α, and the symbol $(\bar{})$ denotes the complex conjugate.

6.2.1. Analytical results

The procedure employed in [25] to predict the kink angle for a given loading γ and α (and particularized to $\beta = 0$) is briefly reviewed. For a given loading γ, the interface crack is assumed to have kinked by an angle ω, forming an extended crack of length a. The kinked crack surfaces are free of traction. In [25], the kinked crack is considered to be a distribution of edge dislocations. To enforce traction free conditions on the kinked crack segment, the stress fields from the interface crack and the distribution of edge dislocations are superimposed and set to zero. This leads to a singular integral equation which is solved numerically using Chebyshev polynomials. The complex valued functions c and d are tabulated for different values of ω. The energy release rate $\mathcal{G}$, given by

$$\mathcal{G} = q^{-2}\,\mathcal{G}_0\left[|c|^2 + |d|^2 + 2\Re\left(cde^{2i\gamma}\right)\right], \tag{25}$$

is computed as a function of ω, where $|\cdot|$ denotes the magnitude of a complex number. In this equation, the symbol $q := \sqrt{1/(1+\alpha)}$, the symbol $\mathcal{G}_0$ is the energy release rate of the interface crack and the symbol $\Re(\cdot)$ is the real part of complex number. A crack propagation criterion is necessary to specify the kink angle ω. In [25], the crack is assumed to kink in the direction that maximizes $\mathcal{G}$ for a given α and γ. This condition is called the maximum energy release rate (MER) criterion. The optimal kink angle is denoted by $\hat{\omega}$. For a given γ and α, the kink angle $\hat{\omega}$ can be computed by setting $d\mathcal{G}/d\omega|_{\omega=\hat{\omega}} = 0$ for $d^2\mathcal{G}/d\omega^2|_{\omega=\hat{\omega}} < 0$.

To compute $\hat{\omega}$ from (25), the functional form of the complex valued functions $c(\omega,\alpha)$ and $d(\omega,\alpha)$ are necessary. No analytical solution exists, so one would need to solve the singular integral equation as in [25] and tabulate the coefficients for $c(\omega,\alpha)$ and $d(\omega,\alpha)$. To circumvent this issue, Veljkovic [76] proposed closed form approximations to the complex valued functions $c(\omega,\alpha)$ and $d(\omega,\alpha)$, given as

$$c(\omega,\alpha) \approx \frac{1}{2}\sqrt{\frac{1}{1+\alpha}}\left(e^{-\frac{i\omega}{2}} + e^{-\frac{3i\omega}{2}}\right), \tag{26a}$$

$$d(\omega,\alpha) \approx \frac{1}{4}\sqrt{\frac{1}{1-\alpha}}\left(e^{-\frac{i\omega}{2}} - e^{\frac{3i\omega}{2}}\right). \tag{26b}$$

We reiterate that the prior expressions are specialized for the case of $\beta = 0$.

We evaluate the accuracy of the approximate functions given in (26) by computing the kink angles for the cases of $\alpha = \{0, 0.25, 0.5\}$ and comparing them to those computed with the tabulated data provided in [25]. In Fig. 5(a), we plot the computed kink angles as a function of phase angle γ using the tabulated data of [25] and the approximate functions [76] for $\alpha = 0$. The tabulated data and approximate functions produce similar kink angles $\hat{\omega}$, particularly at low γ. We also plot the kink angles for $\alpha = 0.25$ and 0.5 in Figs. 5(b) and (c), respectively. The values of $\hat{\omega}$ computed using the approximate functions of [76] are less accurate for $\alpha = 0.5$ than for $\alpha = 0$ or $\alpha = 0.25$. Thus, we can conclude that the approximate closed form solutions for $c(\omega, \alpha)$ and $d(\omega, \alpha)$ given in (26) should not be used for $\alpha > 0.5$.

6.2.2. Simulations with RVFTI

To benchmark RVFTI, we propose to compute the kink angles for an interface crack for $\alpha = \{0, 0.25, 0.5\}$ and $0 \leq \gamma \leq \pi/4$. We consider a circular domain as shown in Fig. 4(b), where the interface crack is modeled as a notch whose length is equal to that of the radius $R_0 = 1000$ mm. The region above the notch is material 1 and the region below the notch is material 2. An enlarged view of the notch root is shown in Fig. 4(c), along with a local polar coordinate system attached to the notch tip. Contrary to polar angle θ, we measure kink angle $\hat{\omega}$ clockwise with respect to the x-axis. The notch root radius is $r_0 = R_0/2000$. For the phase-field model, we select $\varepsilon = r_0$ and $k_\varepsilon = 2.5 \times 10^{-4}$, while the widened interface ahead of the notch has width $m\varepsilon = r_0/10 = R_0/20000$.

We set $\mu_1 = 1000$ MPa and $\nu_1 = 0.3$ for material 1, while the elastic parameters for material 2 are determined from $\beta = 0$ and $\alpha \in \{0, 0.25, 0.5\}$. We assign to both materials an identical bulk fracture toughness g_b, while the widened interface has fracture toughness g_i. The values of g_b and g_i are chosen to ensure that the crack will always kink into material 2 (see [25] for details).

Along the outer boundary (at $r = R_0$, a sufficient distance from the notch tip), the domain is subjected to the asymptotic displacement fields for an interface crack. With $\beta = 0$, these may be written in complex notation as

$$u_x + iu_y = \frac{|K|\sqrt{R_0}}{\mu_1}\sqrt{\frac{1}{8\pi}}\left((3 - 4\nu_1)\, e^{i\left(\frac{\theta}{2} - \gamma\right)} - e^{-i\left(\frac{\theta}{2} + \gamma\right)} - i \sin\theta\; e^{i\left(\frac{\theta}{2} + \gamma\right)}\right), \tag{27a}$$

for material 1, and

$$u_x + iu_y = \frac{|K|\sqrt{R_0}}{\mu_2}\sqrt{\frac{1}{8\pi}}\left((3 - 4\nu_2)\, e^{i\left(\frac{\theta}{2} - \gamma\right)} - e^{-i\left(\frac{\theta}{2} + \gamma\right)} - i \sin\theta\; e^{i\left(\frac{\theta}{2} + \gamma\right)}\right) \tag{27b}$$

for material 2, where $|K| = \sqrt{K_1^2 + K_2^2}$. The individual displacement components u_x or u_y are extracted from (27) as the real or imaginary parts of the previous equations, respectively. In our simulations, for each γ, we slowly increase the stress intensity magnitude $|K|$ until a crack nucleates at the notch tip and grows into material 2.

The presence of a non-zero notch root radius and the phase-field length scale ε slightly alters the stress field around the crack tip. However, by choosing these dimensions to be small compared with R_0, the alteration to the stress field should be minor. As a check, we compare the resulting stresses on the outer boundary (at $r = R_0$) with the analytical expressions, which are given for

$\beta = 0$ in the following form:

$$\sigma_{11} + \sigma_{22} = \frac{|K|}{\sqrt{R_0}} \frac{1}{\sqrt{2\pi}} \left(e^{-i\left(\frac{\theta}{2}+\gamma\right)} + e^{i\left(\frac{\theta}{2}+\gamma\right)} \right), \tag{28a}$$

$$\sigma_{11} - \sigma_{22} + 2i\sigma_{12} = \frac{|K|}{\sqrt{R_0}} \frac{e^{i\theta}}{\sqrt{2\pi}} \left(e^{i\left(\frac{\theta}{2}+\gamma\right)} \cos\theta - e^{-i\left(\frac{\theta}{2}+\gamma\right)} \right). \tag{28b}$$

The individual stress components may be computed by extracting the real and imaginary components in (28), though we omit these expressions for brevity. In Fig. 6, we plot the analytical stress components as well as those computed from the finite element simulations, and we observe close agreement between the two.

We show example contour plots of the damage field d from the RVFTI simulations in Fig. 7, corresponding to the cases with $\alpha = 0.25$ and $\gamma = \pi/12$ and $\pi/6$. We also show how the kink angle $\hat{\omega}$ is measured from the damage field. The final kink angles are presented in Fig. 5, alongside the theoretical predictions of [25]. Despite our use of a finite-radius notch and the subtle ambiguity of measuring kink angles from d, it can be seen that the kink angles compare reasonably well to the analytical values.

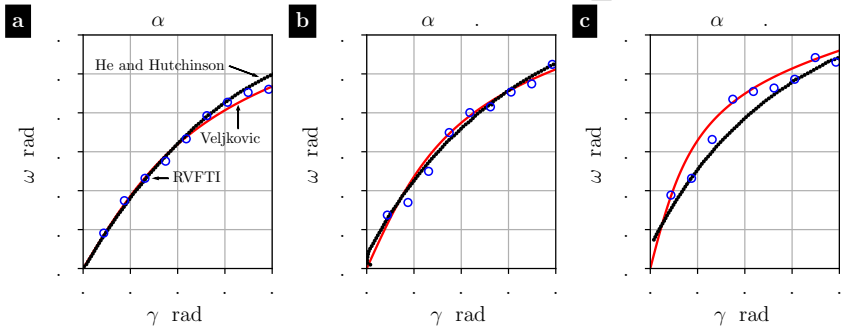

Figure 5: Theoretical and computed kink angles $\hat{\omega}$ versus mode mixity $\gamma = \tan(K_2/K_1)$ for a crack at a bi-material interface with Dundurs mismatch parameters $\beta = 0$ and (a) $\alpha = 0$, (b) $\alpha = 0.25$, and (c) $\alpha = 0.5$. The black circles show the theoretical angles computed from (25) using tabulated values of $c(\omega, \alpha)$ and $d(\omega, \alpha)$ from [25]. The red lines show the theoretical angles computing using approximations of $c(\omega, \alpha)$ and $d(\omega, \alpha)$ in (26). The blue circles are the kink angles observed in the simulations using RVFTI.

6.2.3. Crack trapping at the interface

We now consider the same semi-infinite crack at the bi-material interface, but we examine the conditions under which the crack would continue to grow along the interface, rather than kinking into material 2, see Fig. 8(a). In this situation, despite possible shear loading, the interface "traps" the crack. The possibility of crack trapping is considered in [25], where the authors state that as long as the material fracture toughness (g_b) is sufficiently larger than the interface fracture toughness (g_{int}), the crack will remain trapped at the interface. The authors make the condition more precise: if γ is fixed, but the loading intensity is slowly increased, then by Griffith's criterion and the condition of maximum energy release, the crack will grow in the first direction which reaches $\mathcal{G}(\omega) = g(\omega)$. From (25), there emerges two cases. First, if the crack were to kink into material 2, then $\mathcal{G}^* = \max_\omega \mathcal{G}(\omega) = g_b$, while $\mathcal{G}_0 < g_{\text{int}}$. In words, there exists a non-zero potential kink angle

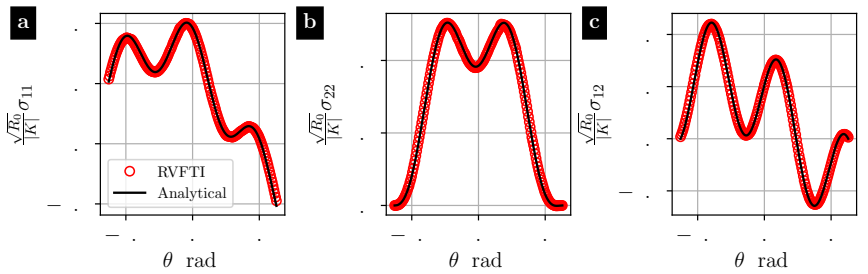

Figure 6: Variation of the far-field stress components versus polar angle θ. The red circles show the data obtained from a simulation using RVFTI with $\alpha = 0.25$ and $\gamma = \pi/12$. The black lines are the analytical formula in (28).

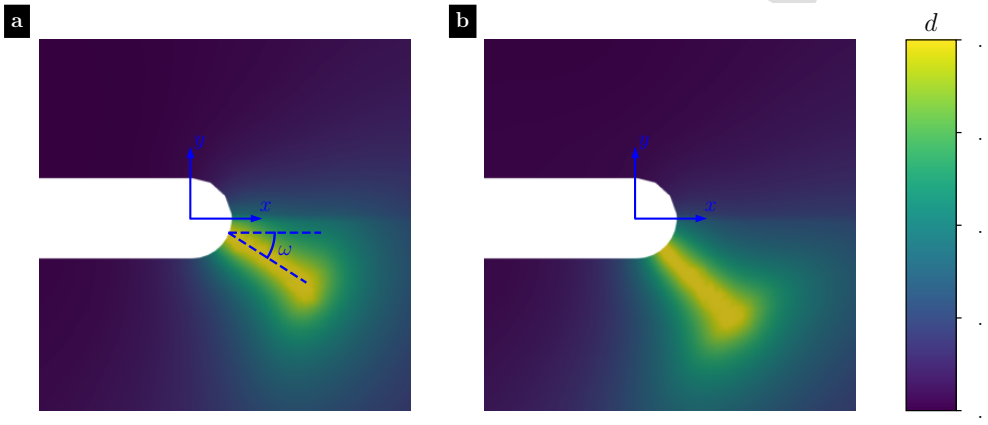

Figure 7: Contour maps of the damage field computed using RVFTI for the crack at a bi-material interface. The simulations were for $\alpha = 0.25$ and (a) $\gamma = \pi/12$ and (b) $\gamma = \pi/6$. The crack set is taken where the material is fully-damaged, $d = 1$, and the kink angle $\hat{\omega}$ is measured clockwise from the x-axis.

for which $\mathcal{G}$ reaches the fracture toughness g_b, while there is insufficient driving force for the crack to continue along the interface. The second case is the opposite, wherein $\mathcal{G}_0 = g_{\text{int}}$, but $\mathcal{G}^* < g_b$. These two cases may be checked simultaneously by comparing the ratios $\mathcal{G}^*/\mathcal{G}_0$ and g_b/g_{int}; the kinking and trapping cases correspond to $\mathcal{G}^*/\mathcal{G}_0 > g_b/g_{\text{int}}$ and $\mathcal{G}^*/\mathcal{G}_0 < g_b/g_{\text{int}}$, respectively.

We assess the prior condition using RVFTI. For these simulations, we use the same domain and boundary conditions as before; however we use a wider weak interface with $m\varepsilon = 2r_0 = R_0/1000$. We also select $k_\varepsilon \in [10^{-6}, 10^{-3}]$. We fix $\gamma = 3\pi/20$ and vary $\alpha \in [0, 0.5]$. We choose $g_i = 0.4$ N/mm, and we select g_b so that $g_b/g_{\text{int}} \in [1, 2.6]$, a range which encompasses the predicted values of $\mathcal{G}^*/\mathcal{G}_0$.

In Fig. 8(b), we show the results of our computations, indicating for which combinations of α and g_b/g_{int} the crack is trapped versus kinks. Using the expressions of [76] for the functions $c(\omega, \alpha)$ and $d(\omega, \alpha)$, we also plot the variation of $\mathcal{G}^*/\mathcal{G}_0$ with respect to α. The points above (resp. below) this curve are those for which $g_b/g_{\text{int}} > \mathcal{G}^*/\mathcal{G}_0$ (resp. $g_b/g_{\text{int}} < \mathcal{G}^*/\mathcal{G}_0$), which indicates trapping (resp. kinking) according to the theory of [25]. We observe some quantitative disagreement between the simulations and theory. Notably, there are data points for which the crack kinks despite the

theory predicting trapping. Nonetheless, there is qualitative agreement between the theoretical and computational boundaries between the trapping and kinking regimes.

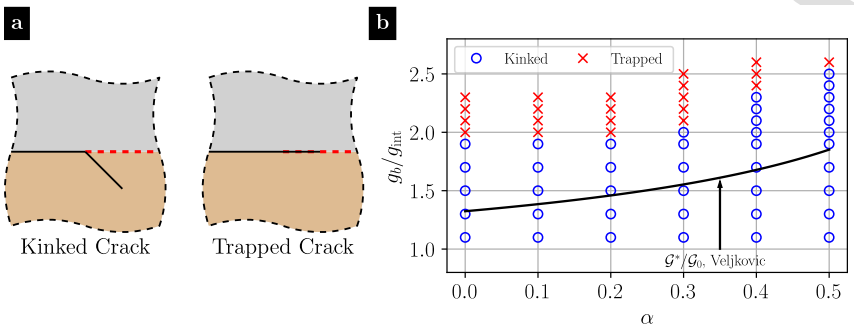

Figure 8: Investigation of crack trapping at a bi-material interface. (a) Visual representation of crack kinking and crack trapping at a bi-material interface. (b) Simulation results using RVFTI for mode mixity $\gamma = 3\pi/20$, and varying the Dundurs mismatch parameter α and the fracture toughness ratio g_b/g_{int}. Circles denote simulations where kinking out of the interface was observed, while crosses correspond to simulations where the crack remained trapped at the interface. The solid black curve shows the ratio $\mathcal{G}^*/\mathcal{G}_0$, computed using the approximations of [76]. From the theory of [25], crack trapping is expected whenever $g_b/g_{\text{int}} > \mathcal{G}^*/\mathcal{G}_0$ (above the black curve), while kinking occurs otherwise.

7. Numerical simulations of toughness enhancement

In this section, we use RVFTI to investigate toughness enhancement in materials with weak interfaces. In particular, we study two-dimensional analogues of micro-architectural designs in SBs and ceramic composites to gain insights into the mechanisms which enhance toughness. Two specimens with specific micro-architectural designs are considered in this section:

(1) a three-point bending in a multi-layered composite, where the bulk material has weak interfaces aligned perpendicular to the fracture growth direction, and
(2) a single edge notch (SEN) geometry with a sinusoidal interface aligned with the crack growth direction.

7.1. Multi-layered specimen

The motivation to study multi-layered composites comes from the micro-architecture of spicules. As previously noted, spicules have a three-dimensional micro-architecture where the bulk material (mineral phase) is arranged in concentric layers separated by interfaces (organic phase).

Multi-layered geometries, which can be considered two-dimensional analogues of spicules, have been studied extensively in the context of ceramics [15]. Clegg et al. [15] conducted experiments on SiC, which was made into thin sheets and coated with graphite forming weak interfaces. The sheets were then pressed together to form a layered micro-architecture which can be seen in Fig. 9(a.ii). The work of fracture for the layered SiC-graphite material, which was notched and tested under three point bending, was found to be 4625 J/m^2, while that of monolithic SiC was 62 J/m^2. As seen in Fig. 9(a.ii), the fracture surface of the layered material showed crack deflection into the weak interfaces. Meanwhile, the load-displacement response in Fig. 9(a.i) indicates that the ceramic composite did not catastrophically fail once the peak load was reached; rather, the material failed in a sequence of catastrophic steps beyond the peak load. From these experiments, it is unclear whether crack deflection was the only toughness-enhancing mechanism. Furthermore, any correlation between the crack path and the observed step-like features in the load-displacement response was not well investigated. We aim to address these points using RVFTI.

We consider the three-point bending specimen shown in Fig. 9(b), where the bulk material contains a number of weak interfaces that are aligned parallel to the span of the geometry. These interfaces are roughly uniformly-spaced along the vertical direction of the specimen. For the purpose of RVFTI, we take $\varepsilon = 0.025$ mm, and we widen the interfaces to have total thickness $2m\varepsilon = 0.05$ mm. We set $k_\varepsilon \in [0, 5 \times 10^{-4}]$. The bulk material has fracture toughness $g_b = 0.5$ N/mm. Meanwhile, we select the fracture toughness in the widened interfaces to be $g_i = 0.05$ N/mm, a factor of ten smaller than g_b. Via (8), the effective interface fracture toughness is around $g_{\text{int}} \approx 0.125 g_b$. The V-notch is oriented perpendicular to the interfaces and the geometry is subjected to displacement-controlled three-point bending loads applied at the midpoint of the top surface. We note that the elastic properties are uniform throughout the composite (here, we take $\mu = 8000$ MPa and $\nu = 0.3$); only the toughness is varied in the widened interfaces.

Figure 9(c) shows the effect of the number of layers on the load-displacement response. We observe that the geometry with zero interfaces (i.e., with uniform toughness g_b) reaches a peak load and fails in a brittle manner, as shown by the almost vertical reduction in load after the peak is reached. However, in the specimen with one interface, the load-displacement curve shows a step-like feature after the peak load is reached similar to that seen by Clegg et al. [15]. We examine this further for the specimen with three interfaces, with the final crack path shown in Fig. 9(d). In Fig. 9(e), we show six stages of the evolution of the crack path, labelled A–F; the corresponding

points in the load displacement curve are indicated with black dots in Fig. 9(c). The peak load is reached at A, when the specimen fractures and grows up to the first weak interface at B. Between B and C, the crack deflects into the first weak interface. The crack then grows up to the second weak interface at D and is trapped in the second weak interface until E. Finally, the crack grows to the third interface at F, where it remains trapped until the simulation is terminated.

Observing the experimental and simulated load displacement curves in Fig. 9, one might expect that the vertical sections of the curve would coincide with rapid crack growth in the bulk material, while the flat parts of the steps would correspond to stable crack growth within the weak interfaces. In contrast to our expectation, points B and D (when the crack first reaches an interface) are not at the bottom of the steps of the load-displacement curve. Rather, the load continues to drop even as the crack deflects into the interface. While this behavior may be an artifact of the simulation, the experiments of Clegg et al. [15] do not use high-speed video recordings, and hence do not rule out the possibility of unstable growth of the deflected cracks within the weak layers. We believe this to be an interesting phenomenon which requires further experimental and numerical investigation.

We also remark that the load-displacement curve is flatter and longer on subsequent steps (between B–C and D–E, and beyond F). These features are also present in the load-displacement curve for SiC-graphite, Fig. 9(a.i). The increase in step flatness parallels the increase in system compliance as the crack grows. A possible interpretation for the increase in step length comes from beam bending theory. In beam bending theory, the maximum bending stress is proportional to both the applied displacement and the height of the beam. As the crack grows upward and deflects along a weak interface, the effective height of the beam decreases as the bottom layers of the beam are delaminated. Hence, if a vertical crack will nucleate when a critical stress is reached, then the necessary displacement must increase as the height is reduced. Finally, with respect to the remaining beam height, the thickness of a single layer represents an increasing fraction as the number of layers is reduced, thereby resulting in longer steps.

We lastly compute the work of fracture (i.e. the area under the load-displacement curves) for the multi-layered specimens. Respectively, for zero, one, two, three, and four interfaces the work of fracture is 1250, 1950, 2330, 2240, and 2110 J/m^2. The work of fracture increases from zero to two interfaces, but then decreases for three and four interfaces. This suggests that there may be an optimal number of interfaces for toughness enhancement, though further work is needed to understand how this number depends on design choices such as the material parameters, interface spacing, and specimen geometry.

7.2. Wavy interface

We demonstrated in the previous example how the presence of weak interfaces can enhance toughness via crack deflection and arrest. We next explore how the shape of the interface can also enhance toughness, which plays an important role in some SBs. For example, rams have wavy interfaces in their skull called suture joints that have been experimentally shown to enhance toughness [77]. Suture joints which enhance toughness are also found in the beaks of woodpeckers [78]. There have been experimental studies to determine the role of wavy, weak interfaces in enhancing toughness [79, 80], and several models have been used to understand this process [28, 81, 82]. However, the role of other geometric factors, such as the amplitude of waviness, on toughness enhancement, is not well understood because the aforementioned models do not predict the crack path.

In this section, we review how interface geometry affects the toughness of the structure by computing the work of fracture for single edge notch (SEN) specimens with straight and wavy

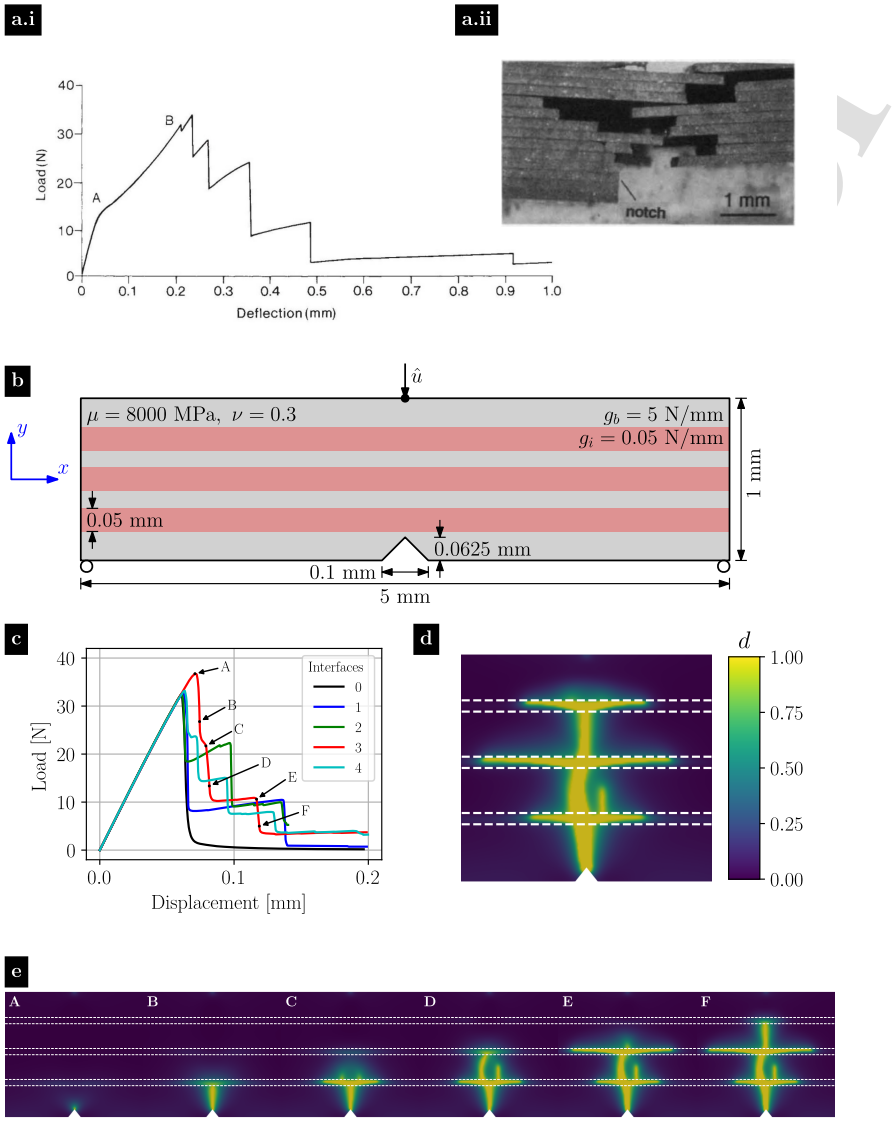

Figure 9: Toughening in a multi-layered specimen. (a.i) Load-deflection response of a SiC-graphite composite [15]. (a.ii) Final fracture surface in SiC-graphite composite [15]. (b) Geometry and loading of a micro-architecture with layers. The bulk material has fracture toughness g_b, while the widened interfaces are assigned fracture toughness g_i. The geometry has a V-notch and is subjected to three point bending loading conditions. (c) Load-displacement response for the layered micro-architecture specimen with zero to four interfaces. (d) Final crack path for the specimen with three interfaces. (e) Evolution of the crack path. The labels A–F in the panels of (e) coincide with the points of the load-displacement curve in (c).

interfaces, depicted in Fig. 10(a). The notch has radius 0.01 mm and length 0.1 mm. For the wavy interface specimen, the interface is initially straight ahead of the notch so that the crack initiation load is identical to that of the straight interface specimen. After the straight portion, the wavy interface is sinusoidal with wavelength and amplitude $\Lambda = A = 0.0625$ mm. The specimens have the same elastic parameters as the previous example, $\mu = 8000$ MPa and $\nu = 0.3$. The bulk material has fracture toughness $g_b = 0.5$ N/mm, and we select a wide-interface fracture toughness $g_i = g_b/100$. For RVFTI, $\varepsilon = 0.004$ mm, $k_\varepsilon = 5 \times 10^{-5}$, and we widen the interfaces by an amount $2m\varepsilon = 0.004$ mm. From these parameters, we compute $g_{\text{int}} \approx 0.02 g_b$. The specimens are subjected to vertical displacement on the top surface of the domain.

The load-displacement response for both the specimens is shown in Fig. 10(b). The wavy interface specimen shows a higher work of fracture than the straight interface specimen. When the interface is straight, the crack propagates along the interface (see Fig. 10(c)). However, when the interface is wavy, the crack path becomes more complicated (see Fig. 10(d)).

Similar to the crack evolution in the multi-layered specimens, one might expect the crack to exhibit unstable growth between segments of the sinusoidal interface, followed by interludes of stable growth or trapping along the interface. However, the simulations show a more complicated behavior with three regimes. In Fig. 10(e), we show snapshots of a portion of the crack evolution as it grows between two segments of the weak interface corresponding to load steps A–E. The corresponding points in the load-displacement curve are shown in Fig. 10(b). From A to B, the crack is trapped along a segment of the weak interface. From B-C, the crack breaks out of the interface and grows in a stable fashion until the crack tip is roughly halfway between segments of the weak interface. From C-D, the crack growth becomes unstable and the crack rapidly grows to the next segment of the weak interface, where it is trapped until E and the cycle continues. This crack growth behavior is highly nontrivial, featuring growth along the interface and in the bulk material, as well as stable and unstable propagation, which highlights the ability of RVFTI to capture a wide variety of crack growth phenomena.

There are other interesting observations during the crack growth process. Cracks nucleate in the weak interface even before the main crack intersects it (see load step C in Fig. 10(e)). These daughter cracks form at the peaks and troughs of the weak interface and immediately ahead of the main crack. The effective interface fracture toughness is weaker than the bulk material (by approximately a factor of 1/50), so cracks nucleate due to the tensile stresses which are present ahead of main crack. This phenomenon is similar to the Cook-Gordon mechanism [83], where the stress field of a crack approaching perpendicularly to a weak interface causes the nucleation of daughter cracks along said interface.

Lastly, like with the number of interfaces in the previous example, there is further room to explore how the amplitude A and wavelength λ of the wavy interface can be chosen to optimize the work of fracture.

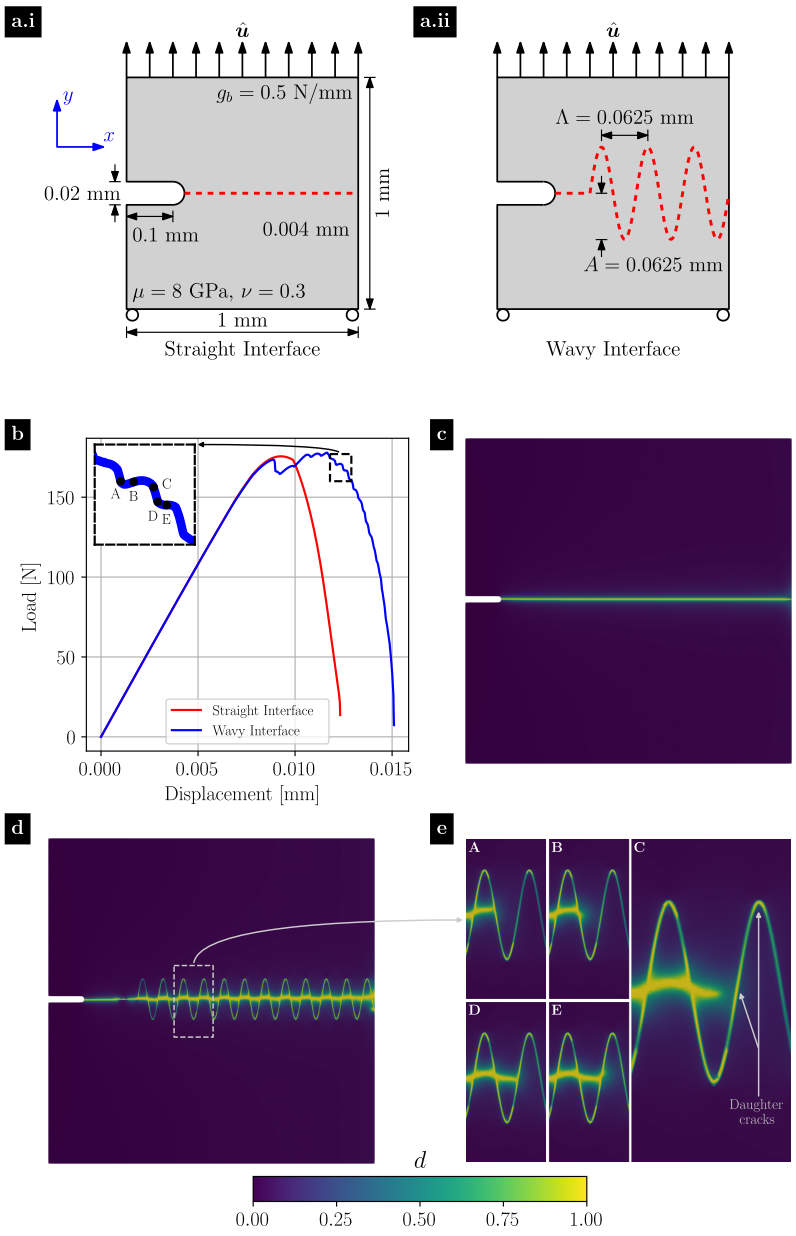

Figure 10: The effect of interface shape on specimen toughness. (a) Geometry and loading for the (a.i) straight and (a.ii) wavy interface specimens. (b) Load-displacement curves for the two specimens. Step-like features are seen in the wavy interface specimen's load-displacement response, see inset. (c) Final damage field for the straight interface specimen. (d) Final damage field for the wavy interface specimen. (e) Zoomed view for a portion of the damage field evolution in the wavy specimen. The labels A–E in subfigure (e) coincide with the black points in the load-displacement curve in subfigure (b).

8. Discussion and conclusions

In this work, we presented a modified regularization of VFT to incorporate weak interfaces. Our goal was to model SBs, which are composites primarily made of a stiff mineral phase and interfaces composed of a compliant organic phase. In SBs, the interface thickness is several orders of magnitude smaller than that of the stiff mineral phase, and it is infeasible to resolve numerically across the interface. We note that our procedure may also be applied to problems with zero-thickness (atomically-thin) interfaces, such as grain boundaries or adhesive contact between dissimilar media.

In our modified regularization approach, we widened the weak interfaces by $2m\varepsilon$, where ε is the regularization length scale for VFT, and set the fracture toughness inside to a value $g_i < g_b$, where g_b is the fracture toughness of the surrounding material. In this way, the interfaces had reduced toughness, and the thickness of the interface decreased to 0 along with ε. We presented an analytical expression for the effective interface fracture toughness g_{int} in the limit of vanishing thickness of the interface, which depended on m, g_b, and g_i. Notably, one was able to select m and g_i to achieve any desired value for the interface toughness g_{int}. We then proved a Γ-convergence result for two-dimensional domains with weak interfaces.

The regularization approach in this work is an important step towards modeling interface fracture and the complex crack patterns that form in SBs. In particular, we derived an effective fracture toughness for interfaces in a material with homogenous g_b. In SBs such as spicules, the organic phase is mixed with the mineral phase, which may cause the fracture toughness g_b to vary within the mineral phase. Future work is needed to determine how the effective interface fracture toughness depends on local variation in g_b. Further, even under constant g_b, one may wish to model interfaces with varying toughness (i.e. $g_{\text{int}}(\boldsymbol{x})$); it is interesting to explore whether the approach in this paper may accommodate such behavior, perhaps through appropriate selection of g_i or m.

We applied the modified regularization approach within a numerical implementation of VFT, which we termed RVFTI. While additional work is needed to connect the numerical model with the theory, we demonstrated that RVFTI reproduced the expected interface fracture toughness predicted by the theory. RVFTI was also used to study two toughening mechanisms in SBs due to the presence of layered microarchitectures and wavy interfaces. For the layered microarchitecture, we observed the "stepped" load-displacement curves present in experiments [15], which corresponded in the simulations to crack arrest and deflection at the weak interfaces. Meanwhile, for the wavy interface specimen, bulk crack growth was impeded by both crack arrest and deflection, as well as the formation of daughter cracks. In both cases, more exhaustive parameter studies may be performed to explore which configurations achieve "optimal" toughness.

Acknowledgements

Authors K.V., B.E.G.P., and H.K. gratefully acknowledge the support of the U. S. Office of Naval Research under PANTHER 1 award number N00014-18-1-2494, PANTHER 2 award number N00014-21-1-2044, PANTHER 3 award number N00014-21-1-2855, and TIGER award number N00014-21-1-2054 through Dr. Timothy Bentley. They also gratefully acknowledge the support from the Collaborative Research Laboratory for Computational Materials Research at Brown University. Authors P.Y. and C.J.L. gratefully acknowledge the support of the U. S. National Science Foundation under grants DMS-1909991 and DMS-2206114.

References

[1] R. Ritchie, The conflicts between strength and toughness, Nature Materials 10 (11) (2011) 817–822.

[2] F. Barthelat, H. Espinosa, An experimental investigation of deformation and fracture of nacre–mother of pearl, Experimental Mechanics 47 (3) (2007) 311–324.

[3] F. Barthelat, R. Rabiei, Toughness amplification in natural composites, Journal of the Mechanics and Physics of Solids 59 (4) (2011) 829–840.

[4] J. Currey, Mechanical properties of mother of pearl in tension, Proceedings of the Royal Society of London. Series B. Biological Sciences 196 (1125) (1977) 443–463.

[5] R. Rabiei, S. Bekah, F. Barthelat, Nacre from mollusk shells: Inspiration for high-performance nanocomposites, in: M. John, S. Thomas (Eds.), Natural Polymers, Vol. 2 of Green Chemistry, Royal Society of Chemistry, 2012, pp. 113–146.

[6] J. C. Weaver, G. W. Milliron, P. Allen, A. Miserez, A. Rawal, J. Garay, P. J. Thurner, J. Seto, B. Mayzel, L. J. Friesen, et al., Unifying design strategies in demosponge and hexactinellid skeletal systems, The Journal of Adhesion 86 (1) (2010) 72–95.

[7] A. Jackson, J. Vincent, R. Turner, The mechanical design of nacre, Proceedings of the Royal Society of London. Series B. Biological sciences 234 (1277) (1988) 415–440.

[8] X. Wang, M. Wiens, H. C. Schröder, S. Hu, E. Mugnaioli, U. Kolb, W. Tremel, D. Pisignano, W. E. Müller, Morphology of sponge spicules: Silicatein a structural protein for bio-silica formation, Advanced Engineering Materials 12 (9) (2010) B422–B437.

[9] J. C. Weaver, I. Pietrasanta, N. Hedin, B. F. Chmelka, P. K. Hansma, D. E. Morse, et al., Nanostructural features of demosponge biosilica, Journal of Structural Biology 144 (3) (2003) 271–281.

[10] J. R. Neilson, N. C. George, M. M. Murr, R. Seshadri, D. E. Morse, Mesostructure from hydration gradients in demosponge biosilica, Chemistry–A European Journal 20 (17) (2014) 4956–4965.

[11] I. Zlotnikov, D. Shilo, Y. Dauphin, H. Blumtritt, P. Werner, E. Zolotoyabko, P. Fratzl, In situ elastic modulus measurements of ultrathin protein-rich organic layers in biosilica: towards deeper understanding of superior resistance to fracture of biocomposites, RSC Advances 3 (17) (2013) 5798–5802.

[12] H. G. Tattersall, G. Tappin, The work of fracture and its measurement in metals, ceramics and other materials, Journal of Materials Science 1 (3) (1966) 296–301.

[13] U. G. Wegst, H. Bai, E. Saiz, A. P. Tomsia, R. O. Ritchie, Bioinspired structural materials, Nature Materials 14 (1) (2015) 23–36.

[14] S. Suresh, Fatigue crack deflection and fracture surface contact: micromechanical models, Metallurgical Transactions A 16 (1) (1985) 249–260.

[15] W. Clegg, K. Kendall, N. M. Alford, T. Button, J. Birchall, A simple way to make tough ceramics, Nature 347 (6292) (1990) 455–457.

[16] A. Evans, Z. Suo, R. Wang, I. Aksay, M. He, J. Hutchinson, Model for the robust mechanical behavior of nacre, Journal of Materials Research 16 (09) (2001) 2475–2484.

[17] F. Lange, The interaction of a crack front with a second-phase dispersion, Philosophical Magazine 22 (179) (1970) 0983–0992.

[18] A. Bower, M. Ortiz, A three-dimensional analysis of crack trapping and bridging by tough particles, Journal of the Mechanics and Physics of Solids 39 (6) (1991) 815–858.

[19] T. M. Mower, A. S. Argon, Experimental investigations of crack trapping in brittle heterogeneous solids, Mechanics of Materials 19 (4) (1995) 343–364.

[20] G. Xu, A. Bower, M. Ortiz, The influence of crack trapping on the toughness of fiber reinforced composites, Journal of the Mechanics and Physics of Solids 46 (10) (1998) 1815–1833.

[21] G. Huajian, Fracture analysis of nonhomogeneous materials via a moduli-perturbation approach, International Journal of Solids and Structures 27 (13) (1991) 1663–1682.

[22] M. Comninou, The interface crack, Journal of Applied Mechanics 44 (4) (1977) 631–636.

[23] T. Cook, F. Erdogan, Stresses in bonded materials with a crack perpendicular to the interface, International Journal of Engineering Science 10 (8) (1972) 677–697.

[24] F. Delale, F. Erdogan, Interface crack in a nonhomogeneous elastic medium, International Journal of Engineering Science 26 (6) (1988) 559–568.

[25] M.-Y. He, J. W. Hutchinson, Kinking of a crack out of an interface, Journal of Applied Mechanics 56 (2) (1989) 270–278.

[26] J. W. Hutchinson, Z. Suo, Mixed mode cracking in layered materials, Advances in Applied Mechanics 29 (1991) 63–191.

[27] V. Tvergaard, J. W. Hutchinson, On the toughness of ductile adhesive joints, Journal of the Mechanics and Physics of Solids 44 (5) (1996) 789–800.

[28] P. Zavattieri, L. Hector Jr, A. Bower, Determination of the effective mode-I toughness of a sinusoidal interface between two elastic solids, International Journal of Fracture 145 (3) (2007) 167–180.

[29] J. Pro, R. Lim, L. Petzold, M. Utz, M. Begley, GPU-based simulations of fracture in idealized brick and mortar composites, Journal of the Mechanics and Physics of Solids 80 (2015) 68–85.

[30] R. Lim, J. Pro, M. Begley, M. Utz, L. Petzold, High-performance simulation of fracture in idealized 'brick and mortar' composites using adaptive Monte Carlo minimization on the GPU, International Journal of High Performance Computing Applications 30 (2) (2016) 186–199.

[31] M. Hossain, C.-J. Hsueh, B. Bourdin, K. Bhattacharya, Effective toughness of heterogeneous media, Journal of the Mechanics and Physics of Solids 71 (2014) 15–32.

[32] C.-J. Hsueh, L. Avellar, B. Bourdin, G. Ravichandran, K. Bhattacharya, Stress fluctuation, crack renucleation and toughening in layered materials, Journal of the Mechanics and Physics of Solids 120 (2018) 68–78. doi:https://doi.org/10.1016/j.jmps.2018.04.011.

[33] S. Brach, M. Hossain, B. Bourdin, K. Bhattacharya, Anisotropy of the effective toughness of layered media, Journal of the Mechanics and Physics of Solids 131 (2019) 96–111. doi:https://doi.org/10.1016/j.jmps.2019.06.021.

[34] N. R. Brodnik, C.-J. Hsueh, K. T. Faber, B. Bourdin, G. Ravichandran, K. Bhattacharya, Guiding and Trapping Cracks With Compliant Inclusions for Enhancing Toughness of Brittle Composite Materials, Journal of Applied Mechanics 87 (3), 031018 (01 2020). doi:10.1115/1.4045682.

[35] N. R. Brodnik, S. Brach, C. M. Long, G. Ravichandran, B. Bourdin, K. T. Faber, K. Bhattacharya, Fracture diodes: Directional asymmetry of fracture toughness, Phys. Rev. Lett. 126 (2021) 025503. doi:10.1103/PhysRevLett.126.025503.

[36] N. Moës, J. Dolbow, T. Belytschko, A finite element method for crack growth without remeshing, International Journal for Numerical Methods in Engineering 46 (1) (1999) 131–150.

[37] N. Moës, A. Gravouil, T. Belytschko, Non-planar 3d crack growth by the extended finite element and level sets–part I: Mechanical model, International Journal for Numerical Methods in Engineering 53 (11) (2002) 2549–2568.

[38] N. Sukumar, J. Dolbow, N. Moës, Extended finite element method in computational fracture mechanics: a retrospective examination, International Journal of Fracture 196 (1-2) (2015) 189–206.

[39] A. A. Griffith, The phenomena of rupture and flow in solids, Philosophical Transactions of the Royal Society of London. Series A, containing papers of a mathematical or physical character 221 (1921) 163–198.

[40] X.-P. Xu, A. Needleman, Numerical simulations of fast crack growth in brittle solids, Journal of the Mechanics and Physics of Solids 42 (9) (1994) 1397–1434.

[41] G. T. Camacho, M. Ortiz, Computational modelling of impact damage in brittle materials, International Journal of Solids and Structures 33 (20) (1996) 2899–2938.

[42] R. H. J. Peerlings, R. De Borst, W. A. M. Brekelmans, J. H. P. De Vree, Gradient enhanced damage for quasi-brittle materials, International Journal for Numerical Methods in Engineering 39 (19) (1996) 3391–3403. doi:https://doi.org/10.1002/(SICI)1097-0207(19961015)39:19<3391::AID-NME7>3.0.CO;2-D.

[43] A. Karma, D. A. Kessler, H. Levine, Phase-field model of mode III dynamic fracture, Phys. Rev. Lett. 87 (2001) 045501. doi:10.1103/PhysRevLett.87.045501.

[44] G. A. Francfort, J.-J. Marigo, Revisiting brittle fracture as an energy minimization problem, Journal of the Mechanics and Physics of Solids 46 (8) (1998) 1319–1342.

[45] B. Bourdin, G. A. Francfort, J.-J. Marigo, Numerical experiments in revisited brittle fracture, Journal of the Mechanics and Physics of Solids 48 (4) (2000) 797–826.

[46] B. Bourdin, G. A. Francfort, J.-J. Marigo, The variational approach to fracture, Journal of Elasticity 91 (1-3) (2008) 5–148.

[47] L. Ambrosio, V. M. Tortorelli, Approximation of functionals depending on jumps by elliptic functional via Γ-convergence, Communications on Pure and Applied Mathematics 43 (8) (1990) 999–1036.

[48] G. A. Francfort, C. J. Larsen, Existence and convergence for quasi-static evolution in brittle fracture, Communications on Pure and Applied Mathematics 56 (10) (2003) 1465–1500. doi:https://doi.org/10.1002/cpa.3039.

[49] C. Miehe, F. Welschinger, M. Hofacker, Thermodynamically consistent phase-field models of fracture: Variational principles and multi-field FE implementations, International Journal for Numerical Methods in Engineering 83 (10) (2010) 1273–1311.

[50] M. J. Borden, C. V. Verhoosel, M. A. Scott, T. J. Hughes, C. M. Landis, A phase-field description of dynamic brittle fracture, Computer Methods in Applied Mechanics and Engineering 217 (2012) 77–95.

[51] A. C. Hansen-Dörr, R. de Borst, P. Hennig, M. Kästner, Phase-field modelling of interface failure in brittle materials, Computer Methods in Applied Mechanics and Engineering 346 (2019) 25–42. doi:https://doi.org/10.1016/j.cma.2018.11.020.

[52] A. C. Hansen-Dörr, F. Dammaß, R. de Borst, M. Kästner, Phase-field modeling of crack branching and deflection in heterogeneous media, Engineering Fracture Mechanics 232 (2020) 107004. doi:https://doi.org/10.1016/j.engfracmech.2020.107004.

[53] K. Yoshioka, M. Mollaali, O. Kolditz, Variational phase-field fracture modeling with interfaces, Computer Methods in Applied Mechanics and Engineering 384 (2021) 113951. doi:https://doi.org/10.1016/j.cma.2021.113951.

[54] Q. Zhou, Y. Wei, Y. Zhou, L. Yang, An interface-width-insensitive cohesive phase-field model for fracture evolution in heterogeneous materials, International Journal of Solids and Structures 256 (2022) 111980. doi:https://doi.org/10.1016/j.ijsolstr.2022.111980.

[55] A. Unnikrishna Pillai, A. K. Behera, M. M. Rahaman, Combined diffused material interface and hybrid phase-field model for brittle fracture in heterogeneous composites, Engineering Fracture Mechanics 277 (2023) 108957. doi:https://doi.org/10.1016/j.engfracmech.2022.108957.

[56] L. C. Evans, R. F. Gariepy, Measure Theory and Fine Properties of Functions, Revised Edition, Texbooks in Mathematics, CRC press, 2015.

[57] L. Ambrosio, A. Coscia, G. Dal Maso, Fine properties of functions with bounded deformation, Archive for Rational Mechanics and Analysis 139 (3) (1997) 201–238.

[58] L. Ambrosio, N. Fusco, D. Pallara, Functions of Bounded Variation and Free Discontinuity Problems, Clarendon Press, Oxford, 2000.

[59] A. Chambolle, Addendum to "An approximation result for special functions with bounded deformation." [J. Math. Pures Appl.(9) 83 (7)(2004) 929–954]: the N-dimensional case, Journal de Mathématiques Pures et Appliquées 84 (1) (2005) 137–145.

[60] L. Ambrosio, V. M. Tortorelli, On the approximation of free discontinuity problems, Boll. Un. Mat. Ital. B 7 (6) (1992) 105–123.

[61] M. Abate, F. Tovena, Curves and Surfaces, UNITEXT, Springer-Verlag, Milan, 2012.

[62] A. Chambolle, An approximation result for special functions with bounded deformation, Journal de Mathématiques Pures et Appliquées 83 (7) (2004) 929–954. doi:https://doi.org/10.1016/j.matpur.2004.02.004.

[63] A. Vol'pert, S. Hudjaev, Analysis in Classes of Discontinuous Functions and Equations of Mathematical Physics, Vol. 8 of Mechanics: Analysis, Martinus Nijhoff Publishers, 1985.

[64] H. Federer, Geometric Measure Theory, Classics in Mathematics, Springer-Verlag, 1996.

[65] K. Vijaykumar, A variational mechanics theory for modeling the evolution of crack networks in composite materials with brittle interfaces, Ph.D. thesis, Brown University (2019).

[66] G. Dal Maso, An introduction to Γ-convergence, Vol. 8 of Progress in Nonlinear Differential Equations and Their Applications, Springer Science & Business Media, New York, 1993.

[67] T. J. Hughes, The Finite Element Method: Linear Static and Dynamic Finite Element Analysis, Courier Corporation, New York, 2000.

[68] Abaqus, reference manual (2012).

[69] M. Ambati, T. Gerasimov, L. De Lorenzis, A review on phase-field models of brittle fracture and a new fast hybrid formulation, Computational Mechanics 55 (2) (2015) 383–405.

[70] C. Miehe, M. Hofacker, F. Welschinger, A phase field model for rate-independent crack propagation: Robust algorithmic implementation based on operator splits, Computer Methods in Applied Mechanics and Engineering 199 (45) (2010) 2765–2778. doi:https://doi.org/10.1016/j.cma.2010.04.011.

[71] C. Kuhn, R. Müller, A continuum phase field model for fracture, Engineering Fracture Mechanics 77 (18) (2010) 3625–3634.

[72] T. L. Anderson, Fracture Mechanics: Fundamentals and Applications, CRC Press, 2005.

[73] J. Dundurs, Edge-bonded dissimilar orthogonal elastic wedges, Journal of Applied Mechanics 36 (3) (1969) 650–652.

[74] J. Rice, Elastic fracture mechanics concepts for interfacial cracks, Journal of Applied Mechanics 55 (1) (1988) 98–103.

[75] P. M. Anderson, Small scale contact conditions for the linear-elastic interface crack, Journal of Applied Mechanics 55 (4) (1988) 814–817.

[76] J. Veljkovic, The crack kinking out of an interface, Theor Appl Mech 32 (3) (2005) 208–221.

[77] C. R. Jaslow, Mechanical properties of cranial sutures, Journal of Biomechanics 23 (4) (1990) 313–321.

[78] N. Lee, M. Horstemeyer, H. Rhee, B. Nabors, J. Liao, L. N. Williams, Hierarchical multiscale structure–property relationships of the red-bellied woodpecker (melanerpes carolinus) beak, Journal of The Royal Society Interface 11 (96) (2014) 20140274.

[79] M. Mirkhalaf, A. K. Dastjerdi, F. Barthelat, Overcoming the brittleness of glass through bio-inspiration and micro-architecture, Nature Communications 5 (2014).

[80] E. Lin, Y. Li, C. Ortiz, M. C. Boyce, 3d printed, bio-inspired prototypes and analytical models for structured suture interfaces with geometrically-tuned deformation and failure behavior, Journal of the Mechanics and Physics of Solids 73 (2014) 166–182.

[81] Y. Li, C. Ortiz, M. C. Boyce, Stiffness and strength of suture joints in nature, Physical Review E 84 (6) (2011) 062904.

[82] Y. Li, C. Ortiz, M. C. Boyce, A generalized mechanical model for suture interfaces of arbitrary geometry, Journal of the Mechanics and Physics of Solids 61 (4) (2013) 1144–1167.

[83] J. Cook, J. E. Gordon, A mechanism for the control of crack propagation in all-brittle systems, Proceedings of the Royal Society of London. Series A. Mathematical and Physical Sciences 282 (1391) (1964) 508–520.

[84] G. Edgar, Measure, Topology, and Fractal Geometry, 2nd Edition, Undergraduate Texts in Mathematics, Springer, 2008.

[85] A. Braides, Γ-convergence for Beginners, Vol. 22 of Oxford Lecture Series in Mathematics and its Applications, Oxford University Press, 2002.

[86] R. A. Adams, J. J. Fournier, Sobolev Spaces, Vol. 140 of Pure and Applied Mathematics, Academic Press, 2003.

Appendix A. Additional mathematical results

Proposition 5 (Properties of the distance function)**.** *Let $A \subset \mathbb{R}^n$ be a bounded domain. Then* $\operatorname{dist}(\boldsymbol{x}, A) : \mathbb{R}^n \to \mathbb{R}$ *is a Lipschitz continuous function with Lipschitz constant 1. Moreover,* $\operatorname{dist}(\boldsymbol{x}, A) = \operatorname{dist}(\boldsymbol{x}, \overline{A})$.

Proof.

1. Let $\boldsymbol{y} \in \mathbb{R}^n$. Then $\operatorname{dist}(\boldsymbol{x}, \{\boldsymbol{y}\}) = |\boldsymbol{x} - \boldsymbol{y}| : \mathbb{R}^n \to \mathbb{R}$ is Lipschitz continuous with constant 1.
   (a) For any $\boldsymbol{x}, \boldsymbol{z} \in \mathbb{R}^n$, we apply the reverse triangle inequality
   $$\big|\operatorname{dist}(\boldsymbol{x}, \{\boldsymbol{y}\}) - \operatorname{dist}(\boldsymbol{z}, \{\boldsymbol{y}\})\big| = \big||\boldsymbol{x} - \boldsymbol{y}| - |\boldsymbol{z} - \boldsymbol{y}|\big| \leq |(\boldsymbol{x} - \boldsymbol{y}) - (\boldsymbol{z} - \boldsymbol{y})| = |\boldsymbol{x} - \boldsymbol{z}|.$$
2. The function $\operatorname{dist}(\boldsymbol{x}, \overline{A}) : \mathbb{R}^n \to \mathbb{R}$ is Lipschitz continuous with constant 1.
   (a) Fix $\boldsymbol{x} \in \mathbb{R}^n$. Via Step 1 the function $\operatorname{dist}(\boldsymbol{z}, \{\boldsymbol{x}\}) : \overline{A} \to \mathbb{R}$ is Lipschitz continuous over a compact set. Hence, it has a minimum, which it achieves at some point $\boldsymbol{a} \in \overline{A}$. Thus, $\operatorname{dist}(\boldsymbol{x}, \overline{A}) = |\boldsymbol{x} - \boldsymbol{a}|$.
   (b) Then, for any $\boldsymbol{x}, \boldsymbol{y} \in \mathbb{R}^n$:
   $$\operatorname{dist}(\boldsymbol{y}, \overline{A}) - \operatorname{dist}(\boldsymbol{x}, \overline{A}) = \inf_{\boldsymbol{z} \in \overline{A}} |\boldsymbol{y} - \boldsymbol{z}| - |\boldsymbol{x} - \boldsymbol{a}| \leq |\boldsymbol{y} - \boldsymbol{a}| - |\boldsymbol{x} - \boldsymbol{a}| \leq |\boldsymbol{y} - \boldsymbol{x}|,$$
   where the last inequality results from the reverse triangle inequality.
   (c) We may repeat item (a) for $\boldsymbol{y}$; we define its closest point in $\overline{A}$ to be $\boldsymbol{b}$. Then,
   $$\operatorname{dist}(\boldsymbol{x}, \overline{A}) - \operatorname{dist}(\boldsymbol{y}, \overline{A}) = \inf_{\boldsymbol{z} \in \overline{A}} |\boldsymbol{x} - \boldsymbol{z}| - |\boldsymbol{y} - \boldsymbol{b}| \leq |\boldsymbol{x} - \boldsymbol{b}| - |\boldsymbol{y} - \boldsymbol{b}| \leq |\boldsymbol{x} - \boldsymbol{y}|.$$
   (d) Combining the two inequalities gives the desired conclusion.
   $$\big|\operatorname{dist}(\boldsymbol{x}, \overline{A}) - \operatorname{dist}(\boldsymbol{y}, \overline{A})\big| \leq |\boldsymbol{x} - \boldsymbol{y}|.$$
3. Finally, we prove $\operatorname{dist}(\boldsymbol{x}, A) = \operatorname{dist}(\boldsymbol{x}, \overline{A})$.
   (a) For any $\boldsymbol{x} \in \mathbb{R}^n$, let $\boldsymbol{a} \in \overline{A}$ be a closest point (i.e. $\operatorname{dist}(\boldsymbol{x}, \overline{A}) = |\boldsymbol{x} - \boldsymbol{a}|$).
   (b) There is a sequence $(\boldsymbol{a}_n)_n \subset A$ which converges to $\boldsymbol{a}$.
   (c) Because $\overline{A} \supseteq A$, we must have $\operatorname{dist}(\boldsymbol{x}, \overline{A}) \leq \operatorname{dist}(\boldsymbol{x}, A)$.
   (d) For any n, we have
   $$|\boldsymbol{x} - \boldsymbol{a}| = \operatorname{dist}(\boldsymbol{x}, \overline{A}) \leq \operatorname{dist}(\boldsymbol{x}, A) = \inf_{\boldsymbol{z} \in A} |\boldsymbol{x} - \boldsymbol{z}| \leq |\boldsymbol{x} - \boldsymbol{a}_n| \leq |\boldsymbol{x} - \boldsymbol{a}| + |\boldsymbol{a} - \boldsymbol{a}_n|.$$
   (e) Since $|\boldsymbol{a} - \boldsymbol{a}_n|$ can be made arbitrarily small as $n \to \infty$, we have by the squeeze lemma
   $$|\boldsymbol{x} - \boldsymbol{a}| \leq \operatorname{dist}(\boldsymbol{x}, A) \leq |\boldsymbol{x} - \boldsymbol{a}|.$$
   which gives the conclusion.

□

Here, we present some mathematical results related to the Hausdorff measure of curves and subsets of curves, which are used in the proofs in §4. The first result shows an equivalence between the Hausdorff measure and the arc length of a curve.

Proposition 6 (Hausdorff measure and arc-length)**.** *Let $\boldsymbol{\gamma} : [a, b] \to \mathbb{R}^2$ be a continuous, injective, rectifiable curve with length L. Then, if $\Gamma := \boldsymbol{\gamma}([a, b])$,*

$$\mathcal{H}^1(\Gamma) = \mathcal{H}^1(\boldsymbol{\gamma}((a, b))) = L.$$

Proof. The proof may be found in an equivalent result [84, Theorem 6.3.8]. □

The next result concerns the Hausdorff measure of subsets of curves.

Proposition 7 (Hausdorff measure of subsets of curves)**.** *Let $\boldsymbol{\gamma} : [0, L] \to \mathbb{R}^2$ be an injective, C^1-continuous function such that $|\boldsymbol{\gamma}'(s)| = 1$ for almost every $s \in [0, L]$. This is an arc-length parameterization of the curve $\boldsymbol{\gamma}([0, L])$. Then, for any $A \subseteq [0, L]$,*

$$\mathcal{H}^1(\boldsymbol{\gamma}(A)) = \mathcal{L}^1(A).$$

Proof.

1. We recapitulate [56, Theorem 1.8]. For any Radon measure μ (such as the Lebesgue measure),
$$\mu(A) = \inf\{\mu(U) \ : \ A \subseteq U, \, U \text{ open}\}.$$
2. Any open set $U \subset \mathbb{R}$ may be written as a countable union of pairwise-disjoint open intervals $(I_k)_k$.
3. Combining Steps 1 and 2,
$$\mathcal{L}^1(A) = \inf\left\{\sum_{k=1}^{\infty} \mathcal{L}^1(I_k) \ : \ A \subseteq \bigcup_{k=1}^{\infty} I_k, \ I_k \text{ pairwise-disjoint}\right\}.$$
Without issue, we may restrict these sets to lie within the interval $[0, L]$ (i.e. redefine $I_k \leftarrow I_k \cap [0, L]$).
4. Next, let us take an infimizing sequence of open sets $(U_j)_j$. Then, we have
$$\mathcal{L}^1(U_j) \to \mathcal{L}^1(A).$$
Moreover, $\mathcal{L}^1(U_j \setminus A) \to 0$.
5. By [56, Theorem 2.8], we have
$$\mathcal{H}^1(\boldsymbol{\gamma}(U_j \setminus A)) \leq Lip(\boldsymbol{\gamma})\mathcal{L}^1(U_j \setminus A) \to 0,$$
where $Lip(\boldsymbol{\gamma})$ is the Lipschitz constant for $\boldsymbol{\gamma}$ (here equal to 1). This means
$$\mathcal{H}^1(\boldsymbol{\gamma}(U_j)) \to \mathcal{H}^1(\boldsymbol{\gamma}(A)).$$
Moreover, applying Proposition 6 to each pairwise-disjoint interval I_{jk} in U_j,
$$\mathcal{H}^1(\boldsymbol{\gamma}(U_j)) = \sum_{k=1}^{\infty} \mathcal{H}^1(\boldsymbol{\gamma}(I_{jk})) = \sum_{k=1}^{\infty} \mathcal{L}^1(I_{jk}) = \mathcal{L}^1(U_j).$$
Hence, taking the limit as $j \to \infty$ of both sides, we reach the conclusion
$$\mathcal{H}^1(\boldsymbol{\gamma}(A)) = \mathcal{L}^1(A).$$

□

The final result concerns covering closed subsets of a rectifiable curve by a finite number of pairwise disjoint, closed, simply-connected subsets.

Proposition 8. *Let $\boldsymbol{\gamma} : [0, L] \to \mathbb{R}$ be as in Proposition 7, and let $A \subset \boldsymbol{\gamma}([0, L])$ be closed or $\mathcal{H}^1$-almost closed (i.e. $\mathcal{H}^1(\overline{A}/A) = 0$). Then, for any $\eta > 0$, there exists a finite cover of $\overline{A}$ by pairwise disjoint sets $(A_i)_{i=1}^{N_\eta}$ such that each A_i is the image of $[a_i, b_i] \subseteq [0, L]$ under $\boldsymbol{\gamma}$, and*

$$\mathcal{H}^1(A) = \mathcal{H}^1(\overline{A}) \leq \mathcal{H}^1\left(\bigcup_{i=1}^{N_\eta} A_i\right) = \sum_{i=1}^{N_\eta} \mathcal{H}^1(A_i) < \mathcal{H}^1(A) + \eta.$$

Proof.

1. If A is $\mathcal{H}^1$-almost closed, then $\mathcal{H}^1(\overline{A}) = \mathcal{H}^1(A)$, and so the result is unchanged. Going forward, we assume A is closed.
2. Let $B := \boldsymbol{\gamma}_i^{-1}(A)$. By Proposition 7, we have
$$\mathcal{H}^1(A) = \mathcal{L}^1(B).$$
3. Because $\boldsymbol{\gamma}$ is a continuous function and A is closed, B must also be closed.
4. As in the proof of Proposition 7, for any $\eta > 0$, we may find an open set $U \supset B$ such that
$$\mathcal{L}^1(U) = \mathcal{L}^1(B) + \eta.$$
Again, this is an open subset of $\mathbb{R}$, and hence can be expressed as a countable union of pairwise-disjoint open intervals $(U_i)_{i=1}^{\infty}$. Again, without issue, we may restrict these sets to the domain $[0, L]$ (the domain of $\boldsymbol{\gamma}$).
5. The set $(U_i)_{i=1}^{\infty}$ is a cover of B. Meanwhile, B is a closed and bounded subset of $\mathbb{R}$, and hence is compact. Thus, there exists a finite subcover consisting of pairwise-disjoint open intervals $(U_i)_{i=1}^{M_\eta}$ (we have not relabeled in i) such that
$$B \subset \bigcup_{i=1}^{M_\eta} U_i$$
and hence
$$\mathcal{L}^1(B) \leq \sum_{i=1}^{M_\eta} \mathcal{L}^1(U_i) < \sum_{i=1}^{\infty} \mathcal{L}^1(U_i) = \mathcal{L}^1(U) = \mathcal{L}^1(B) + \varepsilon.$$
6. For each i, we may write $U_i = (a_i, b_i)$, and $\overline{U_i} = [a_i, b_i]$. We have $\mathcal{L}^1(\overline{U_i}) = \mathcal{L}^1(U_i) = b_i - a_i$.
7. For any $i \neq j$, if $\overline{U_i} \cap \overline{U_j} \neq \emptyset$, then these sets must overlap at one of the endpoints (since the open sets are disjoint). Hence, we can define $\overline{V_i} = \overline{U_i} \cup \overline{U_j} = [\min(a_i, a_j), \max(b_i, b_j)]$, and we have $\mathcal{L}^1(V_i) = \mathcal{L}^1(\overline{U_i}) + \mathcal{L}^1(\overline{U_j}) = \max(b_i, b_j) - \min(a_i, a_j)$. Repeating this way, we end up with a finite set $(V_i)_{i=1}^{N_\eta}$ of closed, pairwise disjoint intervals (with $N_\eta \leq M_\eta$) such that
$$\sum_{i=1}^{N_\eta} \mathcal{L}^1(V_i) = \sum_{j=1}^{M_\eta} \mathcal{L}^1(\overline{U_j}) = \sum_{j=1}^{M_\eta} \mathcal{L}^1(U_j) < \mathcal{L}^1(B) + \eta.$$

8. Set $A_i := \boldsymbol{\gamma}(V_i)$. Then
$$A \subset \bigcup_{i=1}^{N_\eta} A_i.$$
We remark that since the closed intervals $(V_i)_i$ are pairwise disjoint, then so too must be the sets $(A_i)_i$. Thus,
$$\mathcal{H}^1(A) \leq \mathcal{H}^1\left(\bigcup_{i=1}^{N_\eta} A_i\right) = \sum_{i=1}^{N_\eta} \mathcal{H}^1(A_i).$$
9. Finally, by Proposition 7,
$$\mathcal{H}^1(A) \leq \sum_{i=1}^{N_\eta} \mathcal{H}^1(A_i) = \sum_{i=1}^{N_\eta} \mathcal{L}^1(V_i) < \mathcal{L}^1(B) + \eta = \mathcal{H}^1(A) + \eta.$$

□

Appendix B. Proof of preliminary results

Here, we present the proofs for the preliminary results in §4.3 and §4.4.

Proof of Proposition 2.

1. As the composition of two continuous functions (the distance function to J_i and $\boldsymbol{\gamma}_i$), the function $\operatorname{dist}(\boldsymbol{\gamma}_i(\cdot), J_i) : [0, \mathcal{H}^1(I_i)] \to \mathbb{R}$ is also continuous. Moreover, it is defined over the compact set $[0, \mathcal{H}^1(I_i)]$ and so it achieves its maximum.
2. By assumption on $\mathcal{I}$ (cf. §4.1), an interface curve only intersects other interface curves (or the domain boundary) at its endpoints. Hence, $\max_{s\in[0,\mathcal{H}^1(I_i)]} \operatorname{dist}(\boldsymbol{\gamma}_i(s), J_i) > 0$. Thus,
$$\{s \in [0, \mathcal{H}^1(I_i)] \ : \ \operatorname{dist}(\boldsymbol{\gamma}_i(s), J_i) > 3\rho\}$$
is nonempty whenever $3\rho < \max_{s\in[0,\mathcal{H}^1(I_i)]} \operatorname{dist}(\boldsymbol{\gamma}_i(s), J_i)$; hence $A_{i\rho}$ is also nonempty.
3. We prove Property 1 in the Proposition. For this step, let $\boldsymbol{x} \in A_{i\rho}$.
   (a) Let $\boldsymbol{y} \in I_j$ for $j \neq i$. Suppose $\ell_{i\boldsymbol{x}\rho} \cap \ell_{i\boldsymbol{y}\rho} \neq \emptyset$, and let $\boldsymbol{z} \in \ell_{i\boldsymbol{x}\rho} \cap \ell_{i\boldsymbol{y}\rho}$. Then, via the triangle inequality
   $$|\boldsymbol{x} - \boldsymbol{y}| \leq |\boldsymbol{x} - \boldsymbol{z}| + |\boldsymbol{z} - \boldsymbol{y}| \leq 2\rho.$$
   However, $\boldsymbol{y} \in J_i$, and so
   $$|\boldsymbol{x} - \boldsymbol{y}| \geq \operatorname{dist}(\boldsymbol{x}, J_i) > 3\rho,$$
   which yields the contradiction $3\rho < 2\rho$. Hence, $\ell_{i\boldsymbol{x}\rho} \cap \ell_{i\boldsymbol{y}\rho} = \emptyset$.
   (b) A similar sequence of steps may be used to show that $\ell_{i\boldsymbol{x}\rho} \cap \partial\mathcal{B} = \emptyset$.
   (c) Let $\boldsymbol{y} \in I_i$ with $\boldsymbol{x} \neq \boldsymbol{y}$. Suppose $\ell_{i\boldsymbol{x}\rho} \cap \ell_{i\boldsymbol{y}\rho} \neq \emptyset$, and let $\boldsymbol{z} \in \ell_{i\boldsymbol{x}\rho} \cap \ell_{i\boldsymbol{y}\rho}$. Under the coordinate map (11), we have
   $$\boldsymbol{z} = \boldsymbol{\gamma}_i(s_{\boldsymbol{x}}) + |\boldsymbol{z} - \boldsymbol{x}|\hat{\boldsymbol{n}}_i(s_{\boldsymbol{x}}) = \boldsymbol{\gamma}_i(s_{\boldsymbol{y}}) + |\boldsymbol{z} - \boldsymbol{y}|\hat{\boldsymbol{n}}_i(s_{\boldsymbol{y}})$$
   where $s_{\boldsymbol{x}} = \boldsymbol{\gamma}_i^{-1}(\boldsymbol{x})$ and $s_{\boldsymbol{y}} = \boldsymbol{\gamma}_i^{-1}(\boldsymbol{y})$. However, since $s_{\boldsymbol{x}} \neq s_{\boldsymbol{y}}$ and $|\boldsymbol{z} - \boldsymbol{x}|, |\boldsymbol{z} - \boldsymbol{y}| < \rho < \rho_i$, this implies that the coordinate map is not injective, which contradicts the existence of the tubular neighborhood. Hence, $\ell_{i\boldsymbol{x}\rho} \cap \ell_{i\boldsymbol{y}\rho} = \emptyset$.

4. We next prove Property 2 in the Proposition. Let $\boldsymbol{y} \in \ell_{i\boldsymbol{x}\rho}$ for some $\boldsymbol{x} \in A_{i\rho}$. Because $\cup_{j\neq i} I_j \subset J_i$, $\operatorname{dist}(\boldsymbol{y}, \cup_{j\neq i} I_j) \geq \operatorname{dist}(\boldsymbol{y}, J_i) > \operatorname{dist}(\boldsymbol{x}, J_i) - |\boldsymbol{y}-\boldsymbol{x}| > 2\rho$. Meanwhile $\operatorname{dist}(\boldsymbol{y}, I_i) < |\boldsymbol{y}-\boldsymbol{x}| < \rho$, and so we must have

$$\operatorname{dist}(\boldsymbol{y}, \mathcal{I}) = \operatorname{dist}(\boldsymbol{y}, I_i).$$

Next, suppose there exists $\boldsymbol{z} \in I_i$ (with $\boldsymbol{z} \neq \boldsymbol{x}$) such that $\operatorname{dist}(\boldsymbol{y}, I_i) = |\boldsymbol{y}-\boldsymbol{z}|$. From the previous argument, we know $\boldsymbol{z} \notin \{\boldsymbol{\gamma}_i(0), \boldsymbol{\gamma}_i(\mathcal{H}^1(I_i))\} \subset J_i$. Hence, $\boldsymbol{\gamma}_i^{-1}(\boldsymbol{z}) =: s_{\boldsymbol{z}} \in (0, \mathcal{H}^1(I_i))$. As a minimizer of the distance function in the interior of the interval $[0, \mathcal{H}^1(I_i)]$, $s_{\boldsymbol{z}}$ must also be a stationary point of the function $|\boldsymbol{y}-\boldsymbol{\gamma}_i(s)|^2/2$. However, this means that

$$(\boldsymbol{y}-\boldsymbol{\gamma}_i(s_{\boldsymbol{z}})) \cdot \boldsymbol{\gamma}_i'(s_{\boldsymbol{z}}) = (\boldsymbol{y}-\boldsymbol{z}) \cdot \hat{\boldsymbol{t}}_i(s_{\boldsymbol{z}}) = 0.$$

Thus, $\boldsymbol{y} \in \ell_{i\boldsymbol{z}\rho}$ or $\ell_{i\boldsymbol{x}\rho} \cap \ell_{i\boldsymbol{z}\rho} \neq \emptyset$, which contradicts Property 1. Hence, $\boldsymbol{z} = \boldsymbol{x}$, and so

$$\operatorname{dist}(\boldsymbol{y}, I_i) = |\boldsymbol{y}-\boldsymbol{x}|.$$

5. Finally, we prove Property 3 in the Proposition.
   (a) We may show
   $$I_i \setminus A_{i\rho} = \boldsymbol{\gamma}_i\big(\{s \in [0, \mathcal{H}^1(I_i)] : \operatorname{dist}(\boldsymbol{\gamma}_i(s), J_i) \leq 3\rho\}\big).$$
   (b) Applying Proposition 7,
   $$\mathcal{H}^1(I_i \setminus A_{i\rho}) = \mathcal{L}^1(\{s \in [0, \mathcal{H}^1(I_i)] : \operatorname{dist}(\boldsymbol{\gamma}_i(s), J_i) \leq 3\rho\}).$$
   (c) Via continuity of measures on nesting sets,
   $$\begin{aligned}\lim_{\rho\to 0+} \mathcal{L}^1(\{s \in [0, \mathcal{H}^1(I_i)] : \operatorname{dist}(\boldsymbol{\gamma}_i(s), J_i) \leq 3\rho\}) &= \mathcal{L}^1\left(\bigcap_{\rho>0} \{s \in [0, \mathcal{H}^1(I_i)] : \operatorname{dist}(\boldsymbol{\gamma}_i(s), J_i) \leq 3\rho\}\right) \\ &= \mathcal{L}^1(\{s \in [0, \mathcal{H}^1(I_i)] : \operatorname{dist}(\boldsymbol{\gamma}_i(s), J_i) = 0\}).\end{aligned}$$
   (d) By construction of $\mathcal{I}$, the interface curve I_i may only intersect another interface curve I_j or the domain boundary at its endpoints. Hence
   $$\{s \in [0, \mathcal{H}^1(I_i)] : \operatorname{dist}(\boldsymbol{\gamma}_i(s), J_i) = 0\} = \{0, \mathcal{H}^1(I_i)\},$$
   which is a set with only two elements, and so
   $$\mathcal{L}^1(\{s \in [0, \mathcal{H}^1(I_i)] : \operatorname{dist}(\boldsymbol{\gamma}_i(s), J_i) = 0\}) = 0.$$
   (e) Hence,
   $$\lim_{\rho\to 0+} \mathcal{H}^1(I_i \setminus A_{i\rho}) = 0.$$
   (f) Finally,
   $$\mathcal{H}^1(\Gamma \cap A_{i\rho}) = \mathcal{H}^1(\Gamma \cap I_i) - \mathcal{H}^1(\Gamma \cap (I_i \setminus A_{i\rho})).$$
   Because $\mathcal{H}^1(\Gamma \cap (I_i \setminus A_{i\rho})) \leq \mathcal{H}^1(I_i \setminus A_{i\rho})$, which shrinks to zero as $\rho \to 0+$, we have
   $$\lim_{\rho\to 0+} \mathcal{H}^1(\Gamma \cap A_{i\rho}) = \mathcal{H}^1(\Gamma \cap I_i).$$

□

We next prove Proposition 3. Our proof strategy mirrors existing proof strategies for Γ-lim inf results for domains with homogeneous fracture toughness g, for example [85, Theorem 8.1].

Proof of Proposition 3.

1. Let us denote the functional in (15a) as $\overline{\Pi}_{\varepsilon_n}$. Without loss of generality, we may assume that $\liminf_{n\to\infty} \overline{\Pi}_{\varepsilon_n}[u_n, d_n] < \infty$. Otherwise, the result is trivial to show.
2. Take a subsequence $(u_{n_k}, d_{n_k})_k$ of $(u_n, d_n)_n$ so that
$$\lim_{k\to\infty} \overline{\Pi}_{\varepsilon_n}[u_{n_k}, d_{n_k}] = \liminf_{n\to\infty} \overline{\Pi}_{\varepsilon_n}[u_n, d_n].$$
Going forward, we abuse notation by referring to the subsequence as $(u_n, d_n)_n$.
3. Because $\lim_{n\to\infty} \overline{\Pi}_{\varepsilon_n}[u_n, d_n] < \infty$, then there must be a constant $M < \infty$ such that $\overline{\Pi}_{\varepsilon_n}[u_n, d_n] < M$. In particular, the same bound holds for the elastic energy:
$$0 \leq \int_{-\rho}^{\rho} (1 - d_n)^2 C(u_n')^2 \,\mathrm{d}z \leq M < \infty.$$
4. Via the Sobolev Embedding Theorem [86], $H^1((-\rho, \rho); \mathbb{R}) \hookrightarrow C^0([-\rho, \rho]; \mathbb{R})$, so that u_n and d_n have continuous representatives in their equivalence classes. In particular, these representative functions are bounded on $[-\rho, \rho]$. Going forward, where it is necessary we will abuse notation and let u_n and d_n to refer to the continuous representatives in the original equivalence classes.
5. Pick $0 < \delta < \rho$. Using the uniform bound for the elastic energy and the continuity (and boundedness) of the function $(1 - d_n)^2$, we trivially have
$$M \geq \int_{-\delta}^{\delta} (1 - d_n)^2 C(u_n')^2 \,\mathrm{d}z \geq C \min_{[-\delta,\delta]} (1 - d_n)^2 \int_{-\delta}^{\delta} (u_n')^2 \,\mathrm{d}z.$$
6. Take a subsequence $(u_{n_k}, d_{n_k})_k$ of $(u_n, d_n)_n$ such that
$$\lim_{k\to\infty} \left(\min_{[-\delta,\delta]} (1 - d_{n_k})^2 \right) = \liminf_{n\to\infty} \left(\min_{[-\delta,\delta]} (1 - d_n)^2 \right)$$
and define this limit to be m_δ, which must be non-negative. As before, we abuse notation by referring to the new subsequence as $(u_n, d_n)_n$.
7. Suppose $m_\delta > 0$. There must exist an index N such that, for all $n > N$, we have
$$\min_{[-\delta,\delta]} (1 - d_n)^2 > m_\delta/2.$$
This implies
$$\int_{-\delta}^{\delta} (u_n')^2 \,\mathrm{d}z \leq \max \left\{ \max_{1\leq k\leq N} \int_{-\delta}^{\delta} (u_k')^2 \,\mathrm{d}z, \frac{2M}{C m_\delta} \right\},$$
or that $(u_n')_n$ is a bounded sequence in $L^2((-\delta, \delta); \mathbb{R})$. By weak compactness in $L^2((-\delta, \delta); \mathbb{R})$ [56, Theorem 1.42], there is a subsequence $(u_{n_k}')_k$ of $(u_n')_n$ such that $u_{n_k}' \rightharpoonup f \in L^2((-\delta, \delta); \mathbb{R})$ as $k \to \infty$. That is, for any $v \in L^2((-\delta, \delta); \mathbb{R})$, we have
$$\int_{-\delta}^{\delta} u_{n_k}' v \,\mathrm{d}z \to \int_{-\delta}^{\delta} f v \,\mathrm{d}z.$$

If we restrict our attention to $v \in C_c^\infty((-\delta,\delta);\mathbb{R})$, then applying integration by parts gives

$$\int_{-\delta}^{\delta} u'_{n_k} v \,\mathrm{d}z = -\int_{-\delta}^{\delta} u_n v' \,\mathrm{d}z.$$

Using strong convergence of u_{n_k} to u in $L^2((-\delta,\delta);\mathbb{R})$, we also have

$$-\int_{-\delta}^{\delta} u_{n_k} v' \,\mathrm{d}z \to -\int_{-\delta}^{\delta} u v' \,\mathrm{d}z.$$

If we combine the weak convergence of u'_{n_k} to f and the strong convergence of u_{n_k} to u, we arrive at

$$\int_{-\delta}^{\delta} f v \,\mathrm{d}z = -\int_{-\delta}^{\delta} u v' \,\mathrm{d}z,$$

which holds for any $v \in C_c^\infty((-\delta,\delta);\mathbb{R})$. However, the previous equation is precisely the definition of the weak derivative of u, which implies that $u \in H^1((-\delta,\delta);\mathbb{R})$. This contradicts the assumptions on u in the proposition statement.

8. Hence,

$$\lim_{n\to\infty} \left(\min_{[-\delta,\delta]} (1 - d_n)^2 \right) = 0.$$

Thus, there must exist $(z_n)_n \subset [-\delta,\delta]$ so that $d_n(z_n) \to 1$.

9. For each n, define

$$\mathcal{V}_n = \left\{ d \in H^1((-\rho,\rho);\mathbb{R}) \ : \ d(z_n) = d_n(z_n) \right\}.$$

We have

$$\overline{\Pi}_{\varepsilon_n}(u_n, d_n) \geq \int_{-\rho}^{\rho} \frac{\overline{g}(z/\varepsilon_n)}{2} \left(\frac{d_n^2}{\varepsilon_n} + \varepsilon_n (d'_n)^2 \right) \mathrm{d}z \geq \inf_{d\in\mathcal{V}_n} \int_{-\rho}^{\rho} \frac{\overline{g}(z/\varepsilon_n)}{2} \left(\frac{d^2}{\varepsilon_n} + \varepsilon_n (d')^2 \right) \mathrm{d}z.$$

10. Any $d \in \mathcal{V}_n$ may be written as $d = d_n(z_n)\tilde{d}$, where $\tilde{d} \in \tilde{\mathcal{V}}_n = \left\{ d \in H^1((-\rho,\rho);\mathbb{R}) \ : \ d(z_n) = 1 \right\}$. Moreover,

$$\inf_{d\in\mathcal{V}_n} \int_{-\rho}^{\rho} \frac{\overline{g}(z/\varepsilon_n)}{2} \left(\frac{d^2}{\varepsilon_n} + \varepsilon_n (d')^2 \right) \mathrm{d}z = (d_n(z_n))^2 \inf_{\tilde{d}\in\tilde{\mathcal{V}}_n} \int_{-\rho}^{\rho} \frac{\overline{g}(z/\varepsilon_n)}{2} \left(\frac{\tilde{d}^2}{\varepsilon_n} + \varepsilon_n (\tilde{d}')^2 \right) \mathrm{d}z.$$

11. As a shorthand, let us define $f(\varepsilon_n, z_n, \rho)$ to be the infimum on the right hand side of the previous equation. From the Euler-Lagrange equations, one may directly compute $f(\varepsilon_n, \cdot, \rho)$ and show that it is continuous on $[-\delta,\delta]$ and hence admits a minimum. Then,

$$\overline{\Pi}_{\varepsilon_n}(u_n, d_n) \geq (d_n(z_n))^2 f(\varepsilon_n, z_n, \rho) \geq (d_n(z_n))^2 \min_{z\in[-\delta,\delta]} f(\varepsilon_n, z, \rho).$$

12. We take the limits of both sides of the previous equation as $n \to \infty$:

$$\lim_{n\to\infty} \overline{\Pi}_{\varepsilon_n}(u_n, d_n) \geq \lim_{n\to\infty} \left((d_n(z_n))^2 \min_{z\in[-\delta,\delta]} f(\varepsilon_n, z, \rho) \right).$$

Via Step 8, we have that $\lim_{n\to\infty} d_n(z_n) = 1$. We may show that

$$\lim_{n\to\infty} \left(\min_{z\in[-\delta,\delta]} f(\varepsilon_n, z, \rho) \right) = g_{\text{int}}.$$

Combining these limits, and recalling that the subsequences were chosen in Step 2 and Step 6 so that $\lim_{n\to\infty} \overline{\Pi}_{\varepsilon_n}(u_n, d_n)$ is precisely the original limit inferior in (15a), we reach the desired conclusion.

□

Finally, we prove Proposition 4.

Proof of Proposition 4.

1. Let $A := \boldsymbol{\gamma}_i([s_0, s_1])$. We claim that $\partial\mathcal{N}_\rho(A)$ is a subset of the union of four sets: the boundaries of ρ-neighborhoods of $\boldsymbol{\gamma}_i(s_0)$ and $\boldsymbol{\gamma}_i(s_1)$ (i.e. circles with radius ρ about the two endpoints) and the images of $[s_0, s_1]$ under under the maps

$$\boldsymbol{y}_\pm(s) = \boldsymbol{\gamma}_i(s) \pm \rho\hat{\boldsymbol{n}}_i(s).$$

Proof of the claim:
   (a) For any $\boldsymbol{x} \in \partial\mathcal{N}_\rho(A)$, let the closest point projection onto A be $\boldsymbol{\pi}_A(\boldsymbol{x})$. We note that this may not be unique depending on the value of ρ. Let $s = \boldsymbol{\gamma}_i^{-1}(\boldsymbol{\pi}_A(\boldsymbol{x}))$.
   (b) If $s = s_0$ or s_1, then we trivially have that $\boldsymbol{x} \in \partial\mathcal{N}_\rho(\boldsymbol{\gamma}_i(s_0))$ or $\partial\mathcal{N}_\rho(\boldsymbol{\gamma}_i(s_1))$.
   (c) If $s \in (s_0, s_1)$, then $\boldsymbol{x} - \boldsymbol{\gamma}_i(s)$ must be orthogonal to $\hat{\boldsymbol{t}}_i(s)$. Hence, it can be written as $\boldsymbol{\gamma}_i(s) \pm \rho\hat{\boldsymbol{n}}_i(s)$.

   We next bound the length of each of the four sets.
2. Each circle has circumference $2\pi\rho$.
3. Meanwhile, the arc lengths of the other two sets are computed using

$$\int_{s_0}^{s_1} |\boldsymbol{y}'_\pm(s)| \, \mathrm{d}s.$$

   We may directly compute the derivatives of $\boldsymbol{y}_\pm$:

$$\boldsymbol{y}'_\pm(s) = \left(1 \pm \frac{\rho}{R_i(s)}\right) \hat{\boldsymbol{t}}_i(s)^9$$

   Thus,

$$\int_{s_0}^{s_1} |\boldsymbol{y}'_\pm(s)| \, \mathrm{d}s = \int_{s_0}^{s_1} \left|1 \pm \frac{\rho}{R_i(s)}\right| \, \mathrm{d}s \le \int_{s_0}^{s_1} \left(1 + \frac{\rho}{R_{\min}}\right) \, \mathrm{d}s \le \left(1 + \frac{\rho}{R_{\min}}\right)(s_1 - s_0).$$

4. Since $s_1 - s_0 = \mathcal{H}^1(A)$, we can put together the estimates for the four pieces to yield the conclusion.

□

[9] This follows from the fact that $\hat{\boldsymbol{n}}_i(s) = \boldsymbol{Q}\hat{\boldsymbol{t}}_i(s) = \boldsymbol{Q}\boldsymbol{\gamma}'_i(s)$. Hence $\hat{\boldsymbol{n}}'_i(s) = \boldsymbol{Q}\boldsymbol{\gamma}''_i(s)$, which we note must be orthogonal to $\hat{\boldsymbol{n}}_i(s)$. Finally, $\hat{\boldsymbol{t}}_i(s) \cdot \hat{\boldsymbol{n}}'_i(s) = \hat{\boldsymbol{t}}_i(s) \cdot (\boldsymbol{Q}\boldsymbol{\gamma}''_i(s)) = (\boldsymbol{Q}^\mathsf{T}\hat{\boldsymbol{t}}_i(s)) \cdot \boldsymbol{\gamma}''_i(s) = -\hat{\boldsymbol{n}}_i(s) \cdot \boldsymbol{\gamma}''_i(s) = 1/R_i(s)$, where $\boldsymbol{Q}^\mathsf{T}$ is the transpose of the orthogonal transformation $\boldsymbol{Q}$.

Author Statement for "A regularized variational mechanics theory for modeling the evolution of crack networks in composite materials with brittle interfaces" by Vijaykumar et al.

K.V.: Conceptualization, Methodology, Software, Investigation, Writing – Original Draft
B.E.G.P.: Methodology, Formal Analysis, Investigation, Writing – Original Draft
Y.W.: Software, Investigation
P.Y.: Formal Analysis, Writing – Original Draft
C.J.L.: Methodology, Formal Analysis, Supervision, Writing – Original Draft
H.K.: Conceptualization, Methodology, Supervision, Writing – Original Draft

Declaration of interests

☒ The authors declare that they have no known competing financial interests or personal relationships that could have appeared to influence the work reported in this paper.

☐ The authors declare the following financial interests/personal relationships which may be considered as potential competing interests: